

Arab American University
Faculty of Graduate Studies
Department of Natural, Engineering and
Technology Sciences
Ph.D. Program in Physics



Impurities Effects on Electronic, Thermal and Magnetic
Properties of GaAs Quantum Dot/Ring Nanostructures

Olfat Abdulfatah Ibrahim Omareya

201920344

Dissertation Committee:

Assoc. Prof. Dr. Muayad Abu Saa

Assoc. Prof. Dr. Adli Saleh

Prof. Dr. Mohammad Elsaid

Prof. Dr. Atef Qassrawi

Prof. Dr. Hussein Shannak

Assoc. Prof. Dr. Iyad Saadeddin

This Dissertation Was Submitted in Partial Fulfillment of the
Requirements for the Doctor of Philosophy (Ph.D.) Degree in
Physics.

Palestine, September/2024

© Arab American University. All rights reserved.

Arab American University
Faculty of Graduate Studies
Department of Natural, Engineering and
Technology Sciences
Ph.D. Program in Physics



Dissertation Approval

Impurities Effects on Electronic, Thermal and Magnetic Properties of
GaAs Quantum Dot/Ring Nanostructures

Olfat Abdulfatah Ibrahim Omareya

201920344

This dissertation was defended successfully on 26/09/2024 and approved by:

Dissertation Committee Members:

Name	Title	Signature
1. Assoc. Prof. Dr. Muayad Abu Saa	Main Supervisor	
2. Assoc. Prof. Dr. Adli Saleh	Members of Dissertation Committee	
3. Prof. Dr. Mohammad Elsaid	Members of Dissertation Committee	
4. Prof. Dr. Atef Qassrawi	Members of Dissertation Committee	
5. Prof. Dr. Hussein Shannak	Members of Dissertation Committee	
6. Assoc. Prof. Dr. Iyad Saadeddin	Members of Dissertation Committee	

Palestine, 09/2024

Declaration

I declare that, except where explicit reference is made to the contribution of others, this dissertation is substantially my own work and has not been submitted for any other degree at the Arab American University or any other institution.

Student Name: Olfat Abdulfatah Ibrahim Omareya

Student ID: 201920344

Signature: 

Date of Submitting the Final Version of the Dissertation: 06/11/2024

Dedication

To My Parents and daughters.

Olfat Abdulfatah Ibrahim Omareya

Acknowledgments

Began with a help of more than a hand, and suffered a lot of difficulties. Today, I am here, grateful to ALLAH and after whom to many people who have the right to thank, even though with a few words, suffice it is from my heart. I would like to express my sincere gratitude to my supervisors Assoc. Prof. Dr. Muayad Abu Saa, Assoc. Prof. Dr. Adli Saleh and Prof. Dr. Mohammad Elsaid. They didn't hold back any efforts in warm encouragement and continuous support that made a great effect to feel interesting about what I'm working on.

I would like to extend my gratitude to Prof. Dr. Atef Qasrawi (internal examiner), It is not often that one can find a person to be colleague that always creates the time for listening to the little problems and roadblocks that are unavoidably faced in the research performing. His critical comments and corrections were important to the completion of this work and has taught me unnumbered lessons on the academic research workings.

My genuine thanks to Dr. Hazem Khanfer; the member of Department of Telecommunication Engineering and member of Research LAB at Arab American University, for his technical advices. The depth of his software knowledge has helped me greatly.

Beside my supervisors, I would like to acknowledge the members of Department of Physics at Arab American University. I have greatly profited from the courses I took, the high-quality knowledge I reserved and all opportunities that I had when I worked as a teaching and research assistant and when I participated in conferences that held inside and outside the university.

I wish to express my sincere thanks to external examiners Prof. Dr. Hussein Shannak and Assoc. Prof. Dr. Iyad Saadeddin for his support, valuable suggestions and critical comments.

The friendship of Eman Nazzal and Arwa Abu-Ghannam is much appreciated and has led to good-spirited discussions relating to this research. My deep affection and love extend to them and their childrens.

I am deeply grateful to my husband, Iyad Mukahal, for his invaluable assistance in my Ph.D quest. His consistent support, whether offering a listening ear during times of academic stress or providing practical aid with domestic tasks, has proven effective.

I would like to express my deepest gratitude to my beloved daughters, [Eyla and Laya], whose unwavering love and patience have been a constant source of strength throughout this journey. Their smiles and laughter have been my greatest motivation. Thanks for being my inspiration.

I have no words in my dictionary to express my thanks to my brothers and sisters, Ibrahim, Ihsan, Arkan, Osaid, Dalia and Lamees for their constant support. They were one of the first friendly faces to greet me when I began this Ph.D. thesis. Thanks for you and for the angels that filled our house with happiness and pureness, your childrens, all love.

Last, but not least. I want to express my deepest gratitude to my parents for their instillation of many admirable qualities in me and for the many years of their dedication and support during my studies.

Impurities Effects on Electronic, Thermal and Magnetic Properties of GaAs Quantum Dot/Ring Nanostructures

Olfat Abdulfatah Ibrahim Omareya

Assoc. Prof. Dr. Muayad Abu Saa

Assoc. Prof. Dr. Adli Saleh

Prof. Dr. Mohammad Elsaïd

Prof. Dr. Atef Qassrawi

Prof. Dr. Hussein Shannak

Assoc. Prof. Dr. Iyad Saadeddin

Abstract

In this thesis, the energy spectra of a tuned GaAs quantum dot/quantum ring (QD/QR) with parabolic-inverse squared potential and modified Gaussian confinement under an external magnetic field is studied. For this goal, the Schrödinger equation is analytically solved without and with considering the donor and acceptor impurities term and the energy eigenfunctions and eigenvalues are derived within the framework of effective-mass and parabolic band approximation. Also, the donor binding energy of the system has been theoretically investigated considering the various parameters. Moreover, the density of state has been studied in the QD/QR system characterized by varying magnetic fields, pressures, and impurity and computed over specified energy range using a comprehensive theoretical framework. Our analysis reveals significant variations in the density of state profiles corresponding to changes in these parameters, it provides remarkable insights into the electronic properties of materials.

Based on the calculated energy spectra, the thermal functions of the system have been theoretically obtained. The partition function was calculated and then, the mean energy, free energy, specific heat, and entropy and variation of magnetic entropy of the tuned quantum dot/ring system with and without the impurity effect have been calculated; It is found that the presence of the impurity term causes the specific heat of the system to play a peaky structure. Also, it is observed that the temperature dependence of the magnetocaloric effect shows a pronounced maximum at specified temperatures.

In addition, the computational results show that the impurity, temperature and magnetic field have a great influence on the magnetic characteristics of the system, the behavior of the magnetization and the magnetic susceptibility curves were studied. It is found that the magnetic susceptibility has both negative and positive values with changing the values of temperature and magnetic field strength. The results are offering a critical basis for future experimental researches and practical applications in material science and condensed matter physics.

Keywords: Quantum dot, quantum ring, confinement, GaAs, magnetic, thermal.

Table of Contents

#	Title	Page
	Declaration	i
	Dedication	ii
	Acknowledgments	iii
	Abstract	v
	List of Tables	viii
	List of Figures	ix
	List of Definitions of Abbreviations	xv
Chapter One	Introduction	1
	1.1 Artificial Atoms	1
	1.2 Nanotechnology	2
	1.3 Low Dimensional Systems and Quantum Confinement Effect	2
	1.3.1 The Density of States (DoS)	4
	1.3.2 Quantum Dots (QDs)	5
	1.3.3 Quantum Rings (QRs)	10
	1.4 The Magneto-Caloric Effect	11
	1.5 Proplem Statement	13
	1.6 Thesis Layout	15
Chapter Two	Literature Review	16
Chapter Three	Methodology	19
	3.1 Hamiltonian of Quantum Dot/Quantum Ring (QD/QR) System	19
	3.2 Impurity Effect	22
	3.3 The Binding Energy (E_b)	23
	3.4 The Density of States (DoS)	23
	3.5 Thermodynamic Properties	24
	3.5.1 Statistical Average Energy ($\langle E \rangle$)	24
	3.5.2 Helmholtz Free Energy (F)	24
	3.5.3 Specific Heat (C_v)	25
	3.5.4 Entropy (S)	25
	3.5.6 Magneto-Caloric Effect (MCE)	25
	3.6 Magnetic Properties	26
	3.6.1 The Magnetization (M)	26
	3.6.2 The Magnetic Susceptibility (χ)	26
	3.7 The Dependence of Dielectric Constant and Effective Mass on the Hydrostatic Pressure and Temperature	27
	3.8 Simulation Approach	27
Chapter Four	Results	29

4.1	Electronic Properties	29
4.1.1	Energy Spectra (E_{mn})	29
4.1.2	Binding Energy (E_b)	36
4.1.3	The Density of State (DoS)	41
4.2	Thermal Properties	50
4.2.1	Convergence Test and Statistical energy	50
4.2.2	Helmholtz Free Energy	56
4.2.3	The Specific Heat	61
4.2.4	Entropy	67
4.2.5	Magneto-Caloric Effect (MCE)	72
4.3	Magnetic Properties	78
4.3.1	The Magnetization	78
4.3.2	Magnetic Susceptibility	83
4.4	The Effects of Hydrostatic Pressure and Temperature Dependent of the Electronic Properties	89
Chapter Five	Discussion	102
References		103
ملخص		109

List of Tables

Table #	Title of Table	Page
1.1	The effect of spatial confinement on DOS as a function of energy	5

List of Figures

Figure #	Title of Figure	Page
1.1	Schematic diagram of energy band structures in atoms, bulk semiconductors and quantum nanostructure	3
1.2	Schematic diagram for the classification of low dimensional nanostructures	4
1.3	Quantum confinement and density of state versus energy for various nanostructure systems	5
1.4	Geometry of Quantum dot	6
1.5	Schematic comparison of a real 3D atom and a disk shaped quantum dot	7
1.6	Schematic diagram of energy band structures in bulk semiconductors and quantum nanostructure	8
1.7	Example of size-dependent fluorescence spectra of different colors for QDs	9
1.8	Geometry of Quantum ring	11
1.9	Schematic diagram of magneto-caloric cycle	13
1.10	Schematic representation of quantum dot/quantum ring structure.	14
4.1	Energy of the lowest two confined states for a confined electron versus the applied magnetic field (B) for (a) QD ($\xi=0$) and (b) QD/QR ($\xi=1$)	31
4.2	Energy of the lowest two confined states for a confined electron versus the ω_0 - frequency for (a) QD ($\xi=0$) and (b) QD/QR ($\xi=1$)	32
4.3	Energy of the lowest two confined states for a confined electron versus the V_0 - potential for (a) QD ($\xi=0$) and (b) QD/QR ($\xi=1$)	33
4.4	Energy of the lowest two confined states for a confined electron versus the R_0 - radius for (a) QD ($\xi=0$) and (b) QD/QR ($\xi=1$)	34
4.5	Energy of the lowest two confined states for a confined electron in the 2QD/QR versus the ξ -parameter	35

4.6	Energy of the lowest confined state for a confined electron in the QD/QR versus the magnetic field for different values of V_0 -potential	36
4.7	The ground state and the first excited state binding energies versus (a) magnetic field (B), (b) the confining frequency (ω_0), (c) the potential (V_0) and (d) the radius (R_0)	37
4.8	The ground state binding energy versus R_0 (a) $R_0 = 0-50$ nm and (b) $R_0 = 50-200$ nm for different confinement potential	38
4.9	The ground state binding energy versus confinement frequency in the range of (a) 0-300 THz and (b) 300-700 THz for different potential depths	39
4.10	The ground state and the first excited state binding energies versus the dimensionless parameter ξ	40
4.11	The ground state binding energy versus the dimensionless parameter ξ for different confinement frequencies	41
4.12	The density of state of the QD/QR system with and without impurity effect for n ($1 \rightarrow 5$) and specific magnetic field strengths: (a) 1 T, (b) 20 T, and (c) 40 T and $\Gamma = 0.005$	42
4.13	The density of state of the QD/QR system with and without impurity effect for n ($1 \rightarrow 5$) and specific magnetic field strengths: (a) 1 T, (b) 20 T, and (c) 40 T	43
4.14	The density of state of the QD/QR system for n ($1 \rightarrow 10$) and specific magnetic field strength (1 T), (a) $\kappa = 0$, (b) $\kappa = +1$ and (c) $\kappa = -1$	44
4.15	The density of state of the QD/QR system for n ($1 \rightarrow 10$) and specific magnetic field strength (20 T), (a) $\kappa = 0$, (b) $\kappa = +1$ and (c) $\kappa = -1$	45
4.16	The density of state of the QD/QR system for n ($1 \rightarrow 10$) and specific magnetic field strength (40 T), (a) $\kappa = 0$, (b) $\kappa = +1$ and (c) $\kappa = -1$	46
4.17	The density of state of the QD/QR system for n ($1 \rightarrow 20$) and specific magnetic field strength (1 T), (a) $\kappa = 0$, (b) $\kappa = +1$ and (c) $\kappa = -1$	47
4.18	The density of state of the QD/QR system for n ($1 \rightarrow 20$) and specific magnetic field strength (20 T), (a) $\kappa = 0$, (b) $\kappa = +1$ and (c) $\kappa = -1$	48

4.19	The density of state of the QD/QR system for n ($1 \rightarrow 20$) and specific magnetic field strength (40 T), (a) $\kappa = 0$, (b) $\kappa = +1$ and (c) $\kappa = -1$	49
4.20	Statistical average energy versus number of basis calculated at different values of temperature for QD/QR system without impurity	50
4.21	Statistical average energy versus number of basis calculated at different values of temperature for QD/QR system with (a) donor impurity and (b) acceptor impurity	51
4.22	Mean energy versus temperature with and without the impurity effect for (a) $\xi = 0$ and (b) $\xi = 1$	52
4.23	Mean energy versus temperature for donor impurity case at different magnetic field values	53
4.24	Mean energy versus magnetic field with and without the impurity effect for (a) $\xi = 0$ and (b) $\xi = 1$	54
4.25	Mean energy versus magnetic field for donor impurity case at different temperature values	55
4.26	Mean energy versus temperature for donor impurity case at different confinement potential values	56
4.27	Free energy versus temperature with and without the impurity effect for (a) $\xi = 0$ and (b) $\xi = 1$	57
4.28	Free energy versus temperature for donor impurity case at different magnetic field values	58
4.29	Free energy versus magnetic field with and without the impurity effect for (a) $\xi = 0$ and (b) $\xi = 1$	59
4.30	Free energy versus magnetic field for donor impurity case at different temperature values	60
4.31	Free energy versus temperature for donor impurity case at different confinement potential values	61
4.32	Specific heat versus temperature with and without the impurity effect for (a) $\xi = 0$ and (b) $\xi = 1$	62
4.33	Specific heat versus temperature for donor impurity case at different magnetic field values	63
4.34	Specific heat versus magnetic field with and without the impurity effect for (a) $\xi = 0$ and (b) $\xi = 1$	64

4.35	Specific heat versus magnetic field for donor impurity case at different temperature values	65
4.36	(a) 3D plot and (b) contour plot of specific heat with temperature and magnetic field	66
4.37	Specific heat versus temperature for donor impurity case at different confinement potential values	67
4.38	Entropy versus temperature with and without the impurity effect for (a) $\xi=0$ and (b) $\xi=1$	68
4.39	Entropy versus temperature for donor impurity case at different magnetic field values	69
4.40	Entropy versus magnetic field with and without the impurity effect for (a) $\xi=0$ and (b) $\xi=1$.	70
4.41	Entropy versus magnetic field for donor impurity case at different temperature values	71
4.42	Entropy versus temperature for donor impurity case at different confinement potential values	72
4.43	Variation of entropy versus temperature with and without the impurity effect for (a) $\xi=0$ and (b) $\xi=1$	73
4.44	Variation of entropy versus temperature for donor impurity case at different magnetic field values	74
4.45	Variation of entropy versus magnetic field with and without the impurity effect for (a) $\xi=0$ and (b) $\xi=1$	75
4.46	Variation of entropy versus magnetic field for donor impurity case at different temperature values	76
4.47	Variation of entropy versus temperature for donor impurity case at different confinement potential values	77
4.48	Magnetization versus temperature with and without the impurity effect for (a) $\xi=0$ and (b) $\xi=1$	79
4.49	Magnetization versus temperature for donor impurity case at different magnetic field values	80
4.50	Magnetization versus magnetic field with and without the impurity effect for (a) $\xi=0$ and (b) $\xi=1$	81

4.51	Magnetization versus magnetic field for donor impurity case at different temperature values	82
4.52	Magnetization versus temperature for donor impurity case at different confinement potential values	83
4.53	Magnetic susceptibility versus temperature with and without the impurity effect for (a) $\xi=0$ and (b) $\xi=1$	84
4.54	Magnetic susceptibility versus temperature for donor impurity case at different magnetic field values	85
4.55	Magnetic susceptibility versus magnetic field with and without the impurity effect for (a) $\xi=0$ and (b) $\xi=1$	86
4.56	Magnetic susceptibility versus magnetic field for donor impurity case at different temperature values	87
4.57	(a) 3D plot and (b) contour plot of magnetic susceptibility with temperature and magnetic field	88
4.58	Magnetic susceptibility versus temperature for donor impurity case at different confinement potential values	89
4.59	Energy of $n=1$ state for a confined electron versus the applied pressure with and without impurity for (a) QD ($\zeta=0$) and (b) QD/QR ($\zeta=1$)	90
4.60	Energy of $n=1$ state for a confined electron with three different values of pressure versus (a) the applied magnetic field, (b) confining frequency, (c) confinement potential and (d) the dot radius for QD/QR ($\zeta=1$) with donor impurity	91
4.61	The binding energy of $n=1$ state for a confined electron with three different values of pressure versus (a) the applied magnetic field, (b) confining frequency, (c) confinement potential and (d) the dot radius for QD/QR ($\zeta=1$)	92
4.62	The density of state of the QD/QR system with and without impurity effect for $n(1 \rightarrow 5)$ and three different values of pressure: (a) 0.0 KPa, (b) 0.5 KPa, and (c) 1.0 KPa	93
4.63	The 3D plot of the density of state, energy and pressure of the QD/QR system with and without impurity effect for $n(1 \rightarrow 5)$	95
4.64	The density of state of the QD/QR system for $n(1 \rightarrow 10)$ and specific pressure values (0.0 KPa) for (a) $\kappa=0$, (b) $\kappa=+1$ and (c) $\kappa=-1$	96

4.65	The density of state of the QD/QR system for n ($1 \rightarrow 10$) and specific pressure values (0.5 KPa) for (a) $\kappa = 0$, (b) $\kappa = +1$ and (c) $\kappa = -1$	97
4.66	The density of state of the QD/QR system for n ($1 \rightarrow 10$) and specific pressure values (1.0 KPa) for (a) $\kappa = 0$, (b) $\kappa = +1$ and (c) $\kappa = -1$	98
4.67	The density of state of the QD/QR system for n ($1 \rightarrow 20$) and specific pressure values (0.0 KPa) for (a) $\kappa = 0$, (b) $\kappa = +1$ and (c) $\kappa = -1$	99
4.68	The density of state of the QD/QR system for n ($1 \rightarrow 20$) and specific pressure values (0.5 KPa) for (a) $\kappa = 0$, (b) $\kappa = +1$ and (c) $\kappa = -1$	100
4.69	The density of state of the QD/QR system for n ($1 \rightarrow 20$) and specific pressure values (1.0 KPa) for (a) $\kappa = 0$, (b) $\kappa = +1$ and (c) $\kappa = -1$	10

List of Definitions of Abbreviations

Abbreviations	Title
QD	Quantum dot
QR	Quantum ring
QW	Quantum well
QWR	T-shaped quantum wire
3D	Three dimension
2D	Two dimension
1D	One dimension
0D	Zero dimension
DoS	Density of state
E	Energy
LCD	Liquid crystal display
FIB	Focused ion beam
EB	Electron beam
NOR	Nonlinear optical rectification
QWW	Quantum well-wire
QPD	Quantum pseudo dot
AIM	Asymptotic iteration method
MCE	Magneto-caloric effect
$\langle E \rangle$	Average energy
F	Free energy
C_v	Specific heat
S	Entropy
B	Magnetic Field
A	Vector potential

ω_0	Confinement frequency
V_0	Confinement potential
R_0	Dot radius
T	Temperature
$V(r)$	parabolic-inverse square confinement potential
H_0	Hamiltonian
m^*	Effective mass
\hbar	Planck's constant
c	Velocity of light
e	Charge of electron
r	Electron position
ζ	Dimensionless parameter characterizing the external magnetic field strength
ω_c	Cyclotron frequency
V_{mgp}	Modified Gaussian potential
PEP	Power exponential potential
GP	Gaussian potential
ψ^0	Eigenstate of pure QD without impurity
E^0	Eigenvalue of pure QD without impurity
m	Magnetic quantum number
n	Quantum number
ψ_{mn}	Eigenfunction of the perturbed QD
E_{mn}	Eigenvalue of the perturbed QD
E_b	Binding energy
Z	Partition function

k_B	Boltzmann constant
ΔS	Magneto-caloric potential
ΔT	Temperature change
M	Magnetization
χ	Magnetic susceptibility

Chapter One: Introduction

1.1 Artificial Atoms

The puzzle of atomic spectra was a chief motivation for quantum mechanics development. The wavelike nature of electrons allowed them to occupy only discrete orbits in an atom, with quantized energies. Advancements in modern semiconductor technology have made it possible to fabricate structures that are very small (only a few hundred angstroms in size) in order to resolve their discrete quantum level structure [1].

Artificial atoms are nanoscale systems designed to replicate the essential properties of real atoms, allowing scientists to investigate quantum mechanical phenomena in a controlled conditions. Many technologies, including semiconductor quantum dots, superconducting circuits, and trapped ions, can be used to realize these systems.

Essentially, the spacing between atoms in a semiconductor crystal is typically about 0.3-0.4 nm, whereas artificial atoms are small boxes about 100 nm on a side, contained in a semiconductor, this means that artificial atoms are typically much larger than real atoms. Therefore, an artificial atom in a crystal comprises many natural atoms. The Coulomb energy, which results from the repulsion between electrons orbiting the nucleus, diminishes, as it gets larger because the average spacing between electrons rises, there is another energy scale in the problem that is the separation in energy of the electrons orbits in the artificial atom [2]. The differences in orbital energies drop more quickly than the Coulomb energy as atomic size rises.

For more understanding of artificial atoms, it is helpful to know how to fabricate them. One way to confine electrons to a small region within a semiconductor by using electric field. Alternatively, one employs material boundaries for example by surrounding a metal particle with insulator. Both methods require fabricating very small structures. Electron and X-rays lithography techniques employed to achieve such structures [1].

The study of artificial atoms is a widely expanding research area. It is natural to ask whether the artificial atoms will be useful for applications to electronics. Only one electron at a time can pass through the atom because of the electron-electron interaction. This is achieved in the "turnstile" device [3]. Other applications can be imagined like sensitive electrometers [4].

1.2 Nanotechnology

Nanotechnology is the field of manipulation of matter at nanometer scale length (1–100 nm). It works with materials that range in size from 1 to 100 nm, but due to their small size, these materials noticeably differ from bulk materials in terms of their electrical conductance, chemical reactivity, magnetism, optical effects, and physical strength [5].

Nanotechnology is creating and using structures and devices which have remarkable properties because of their small size. Thus, they can be used for a wide range of applications and the creation of various types of nano devices.

Nanotechnology is one of the most important scientific fields today because it combines knowledge from the fields of medicine, chemistry, biology, physics, engineering and informatics. The most economically significant aspects of nanotechnology today, and presumably in the near future, are the application and use of nanomaterials in mechanical and electronic devices, magnetic and optical components, quantum computing and tissue engineering [6].

The nanofabrication techniques allow us to control precisely both the shape and size of the low dimensional system. The world will be significantly affected by nanotechnology, and because of its endless potential to further enhance daily living, it appears to hold the key to the future of the world. With the use of this technology, it is now possible to adjust a material's strength, durability, reactivity, conductivity, and a number of other characteristics to the needs of a project of interest [7, 8].

1.3 Low- Dimensional Systems and Quantum Confinement Effect

In a low-dimensional system, electron motion is constrained from traveling through all three dimensions of our space. In the past two decades, low dimensional quantum systems have attracted a large attention due to their significance in theoretical physics and practical applications.

The electrons are restricted from moving in three dimensions due to the quantum confinement effect in the heterostructure materials. When at least one of the three dimensions of a semiconductor structure is reduced to a length lower than the Fermi wavelength (1-100 nm), quantization effects become extremely significant [9].

Quantum confinement effect is the most popular term in the nano world, that is essentially due to the atomic structure changes as a result of direct influence of ultra-small length scale on the energy band structure [10]. The potential barriers confine the motion of the carriers (electron and hole) in one or more directions in a quantum confined structure. The energy levels become discrete as particle size decreases until reaches the nanoscale (the decrease in confinement dimension), which confines the motion of an electron moving at random to a specific range of energy levels. The splitting of the electronic energy levels is caused by the presence of many atoms in a bulk material, which leads to continuous energy bands separated by a forbidden zone as shown in Figure 1.1.

The continuous energy bands of a bulk material collapse into discrete, atomic like energy levels when the particle dimension of a semiconductor near to and below the bulk semiconductor Bohr exciton radius (the distance in an electron-hole pair) [11].

As more number of dimensions are confined, more discrete energy levels can be found. In contrast to the continuous absorption spectrum of a bulk semiconductor, the discrete structure of energy levels leads to a discrete absorption spectrum [12].

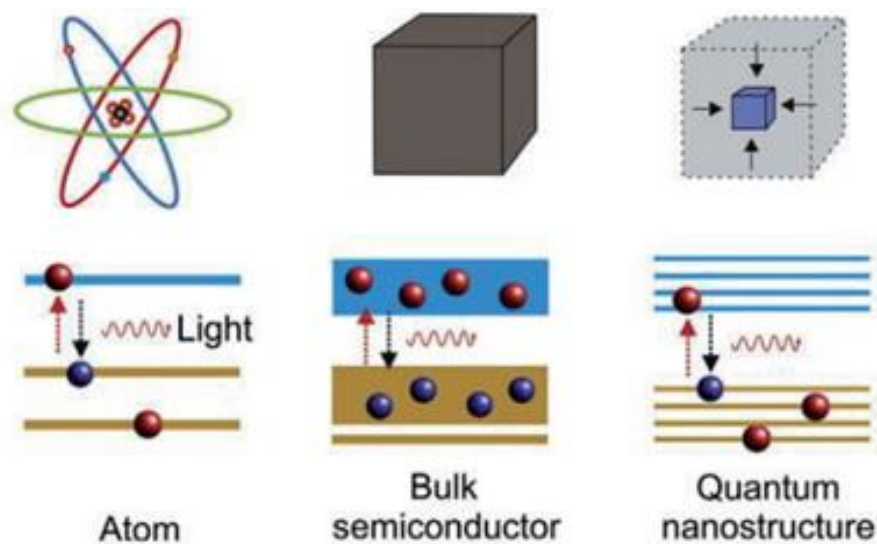


Figure 1.1: Schematic diagram of energy band structures in atoms, bulk semiconductors and quantum nanostructure [12].

Typically, the classification of low-dimensional structures is based on the number of reduced dimensions they contain. A quantum confined structure will be divided into

four categories based on the direction of confinement: bulk structure, quantum well, quantum wire, and quantum dot [13].

In bulk structure or three-dimensional (3D) structure: charge carriers can move freely in the three spatial dimensions (No quantization of the particle motion occurs). In quantum well or two-dimensional (2D) structure: charge carriers are confined in one direction, and free to move in the other two directions. In quantum wire (one-dimensional (1D) structure), the charge carriers have free movement along only one direction. In quantum dots or zero-dimensional structures (0D), charge carriers are eventually confined in all three dimensions [14]. Figure 1.2 summarizes the types of low dimensional systems.

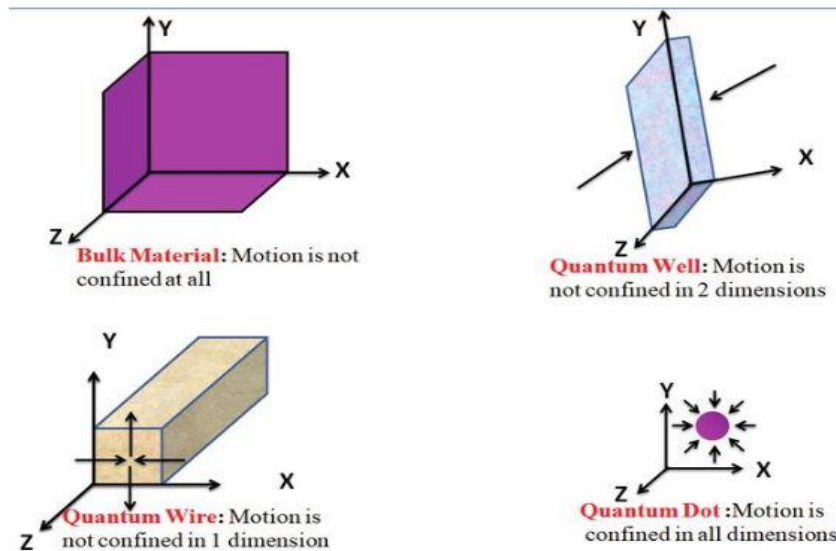


Figure 1.2: Schematic diagram for the classification of low dimensional nanostructures

1.3.1 The Density of State (DoS)

The density of states describes the number of states per energy interval at every energy level that are available to be occupied by electrons. It is dependent upon the dimensional limits of the structure. The units of DoS in a system characterized by three orthogonal parameters (3 dimensions) are $Volume^{-1}Energy^{-1}$, the units of DoS are $Area^{-1}Energy^{-1}$ in two dimensions, the units of DoS are $Length^{-1}Energy^{-1}$ in one dimension.

Table 1.1 and Figure 1.3 shows the density of electron states in bulk, two-dimensional, one-dimensional and zero-dimensional semiconductor structure, Quantum dot has very well defined and quantized energy levels, its density of state shows a discrete behavior unlike to the other confinements which have a continuous density of state [15].

Table 1.1: The effect of spatial confinement on DoS as a function of energy

System	Dimensionality	DoS (E)
Bulk	3D	$DoS \propto \sqrt{E}$
Quantum well	2D	$DoS \propto constant$
Quantum wire	1D	$DoS \propto 1/\sqrt{E}$
Quantum dot	0D	$DoS \propto \delta(E - E_n)$

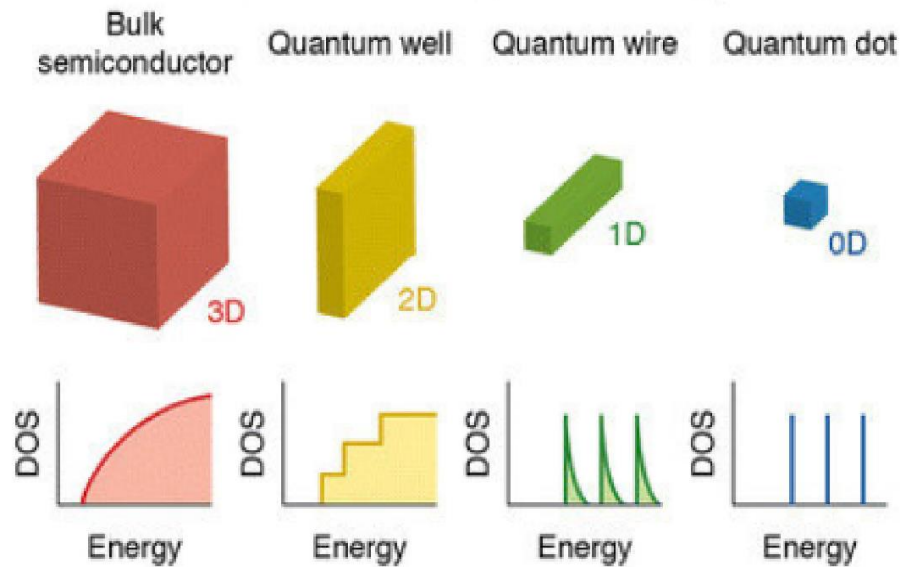


Figure 1.3: Quantum confinement and density of state versus energy for various nanostructure systems.

1.3.2 Quantum Dots (QDs)

With the immense technological advancement during the last two decades, especially in the field of nano-processing, the development of semiconductor heterostructures through different potentials with different shapes allow carrier confinement in all three dimensions and consequently, they behave like electronic quantum dots (QDs). This attracted attention of several researchers worldwide in recent years [16].

Quantum dot is the typical example of ultra-small systems in the field of electronics and optoelectronics. QDs are usually ranging from (2 to 10) nanometers and (10 to 50) atoms in diameter; Figure 1.4 represents the geometry of QD. QDs are conducting islands of a size comparable to the Fermi wavelength; the wavelength that correspond to the highest occupied energy level at absolute zero. In QDs the charge carriers are confined in all three spatial dimensions using artificial confining potentials. Due to this confinement, the electron states are fully quantized into discrete and narrow electronic energy levels [17].

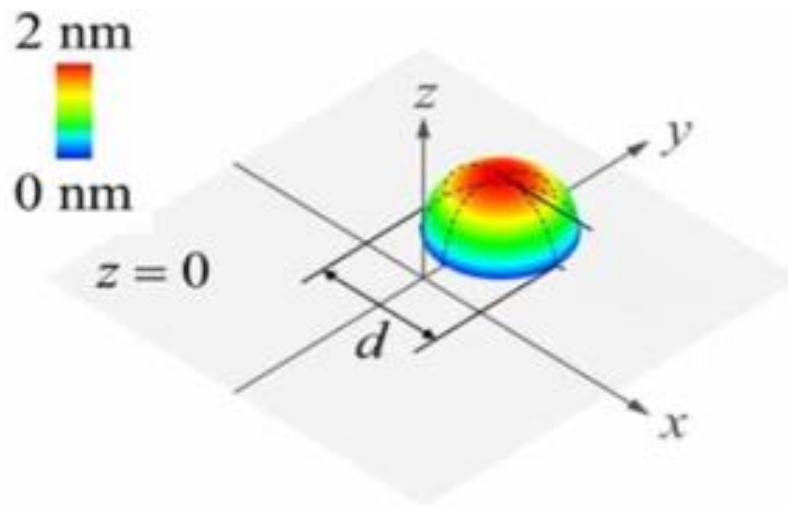


Figure 1.4: Geometry of quantum dot.

Quantum dots are often called the artificial atoms due to the similarity between real atoms and quantum dots. Both have a small number of electrons and discrete energy levels. Electrons in both real and artificial atoms are attracted to a central potential, in artificial atom these electrons trapped in a bowl as parabolic potential, while in a real atom this is a positively charged nucleus (coulomb potential) [18].

In QD's number of electrons can be controlled by artificial external potential, whereas in real atoms can be controlled by ionization. the number of electrons needed to fill each shell in QD is different from real atoms. This comparison is illustrated in Figure 1.5 [18].

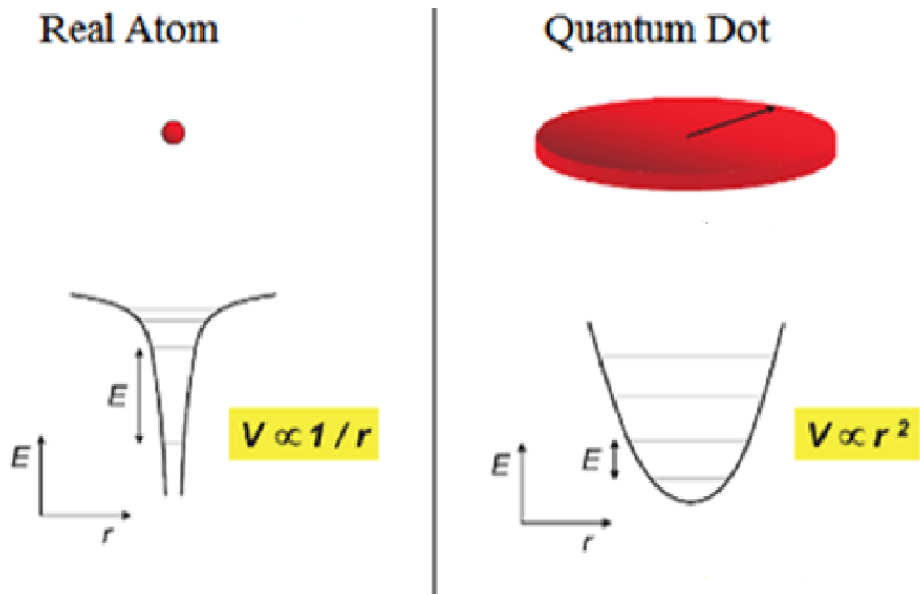


Figure 1.5: Schematic comparison of a real three dimensional atom and a disk-shaped QD.

In an area from a few nanometers to a few hundred nanometers, electrons can move around freely in a bulk semiconductor when energy is applied in the form of heat or an electric field, so the continuous conduction energy band and valence energy band are separated by an energy gap. In contrast, in a quantum dot, discrete atomic like states with energies determined by the quantum dot radius appear because the excitons cannot move freely [12].

The electronic properties of quantum dots are closely related to their composition, size and shape. This makes properties like the optoemission color, absorption spectrum and band gap to be highly tunable, as the QDs size distribution is controlled during fabrication [19]. For instance, the band gap in a quantum dot, that decides the emitted light frequency range, is inversely related to its size. This is represented in Figure 1.6.

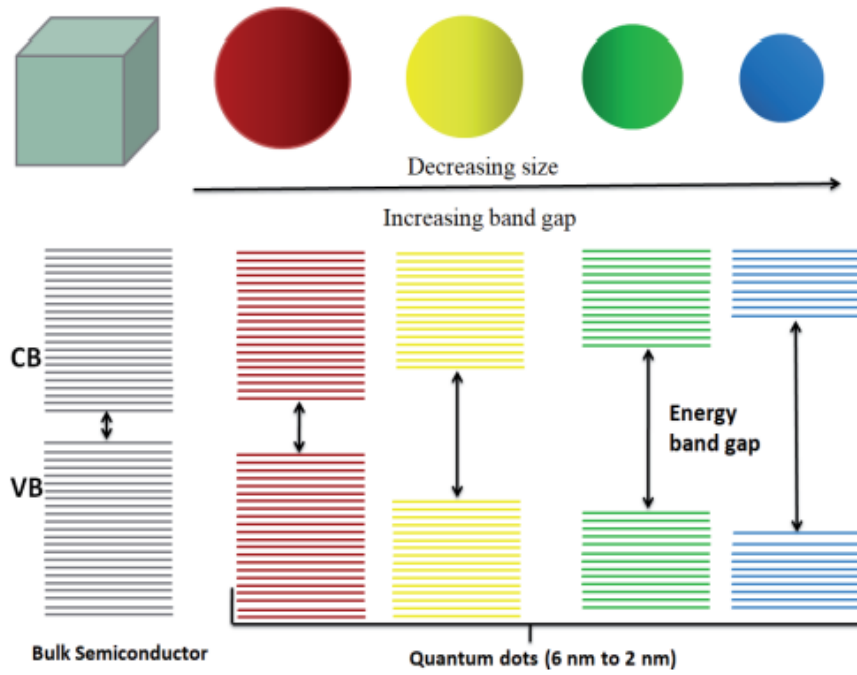


Figure 1.6: Schematic diagram of energy band structures in bulk semiconductors and quantum dots [12].

Longer wavelengths as red are emitted by bigger dots, whereas shorter wavelengths like blue are emitted by smaller dots as shown in Figure 1.7. This property promises the potential for higher performance and more efficient lasers and light emitting diodes (LEDs) [20, 21].

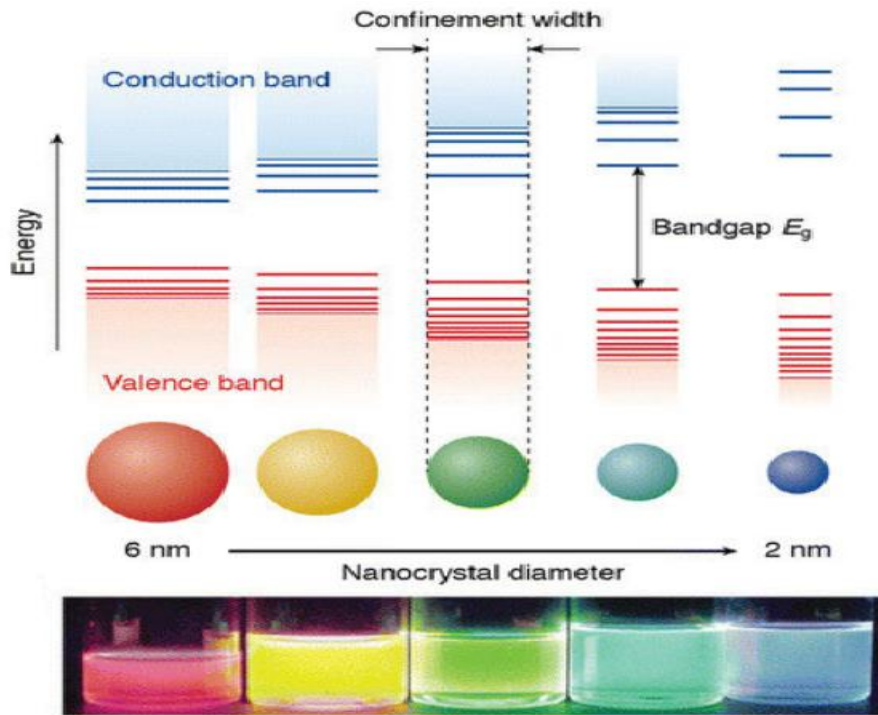


Figure 1.7: Example of size-dependent fluorescence spectra of different colors for QDs [22].

Quantum dots are the subject of interest research because they have remarkable applications in lighting, optical applications and biological applications. For all sorts of applications where the colored light control is vital, QD are perfectly used. The monochromatic light emission with pure and saturated color is produced by the easily tunable band gap of quantum dots. A thin filter made of quantum dots has been developed so it can fit on top of a fluorescent or led lamp especially for enhancing the red emission [23].

Quantum dots are important in present research for both pure and applied physics due to the wealth of applications it has. For example: medical imaging, diode lasers, single electron transistors, solar cells and quantum computing. These QDs materials have unique electronic properties [12].

Different experimental procedures can be used to control the size, shape, and other characteristics of the QDs. Such confinement of charge carriers at the nanoscale in three dimensions results in the full quantum nature of those structures. In other words, QDs are made in a way that allows them to acquire atom-like characteristics like discrete energy levels and shell structures. [16, 24].

Patterning quantum wells (QWs) to create QDs was thought to be the simplest method of QDs fabrication. Because QD size and spatial arrangement may be realized, patterning still has a lot of advantages and attracts much attention. Lithographic techniques come in many different varieties. The most common and traditional technology is optical lithography, which is based on excimer lasers (resolution below 0.2 μm) and UV optics and resists with steep photosensitivity curves. X-rays lithography can be used to create nanostructures it has the advantage of much shorter wavelengths.

The most advanced methods for direct lateral patterning are focused ion beam (FIB) and electron beam (EB) lithography (resolution below 50 nm), produced structures, but their feature sizes were still beyond the desired level. Substrate encoded epitaxy, a more recent technique, enables the creation of tiny nanostructures from a much bigger template [25].

The fabrication of quantum dots through experimental advances and precise measurements of numerous electrical and optical properties have created an interesting situation for theorists and experimentalists alike. There have been several exciting developments where the theoretical predictions and experimental surprises have resulted in deeper understanding of QDs [11].

Future technical developments involving quantum dots are believed to have enormous promise, including quantum cryptography, quantum computation, memory chips and room-temperature quantum-dot lasers [26].

1.3.3 Quantum Rings (QRs)

Modern solid-state physics in the twenty-first century is characterized by the research, design, manufacture, and applications of the wide range of nanostructures that are currently available. Among them, quantum rings, which are low-dimensional structures and have unusual and very new electrical and optical properties as a result of the specific geometrical and structural features of the confining region and potential [27].

Nanoscale sizes and nontrivial topologies are combined in quantum rings, which can have doubly connected rings or even more complex topological characteristics. Once more, this combination results in the appearance of unique physical characteristics,

particularly persistent currents. For quantum mechanical paradigms, quantum rings offer an exceptional playing field [28].

Many geometries of QRs can be considered, the oval and elliptic or circular, although they can be not homogeneously shaped [29]. The morphology of the QRs exhibits variations in their height with respect to the azimuthal angle, which makes the azimuthal quantum number invalid [30]. Experimentally fabricated one-dimensional QRs have a very clearly defined circular shape. The geometry of model QR is presented in Figure 1.8.

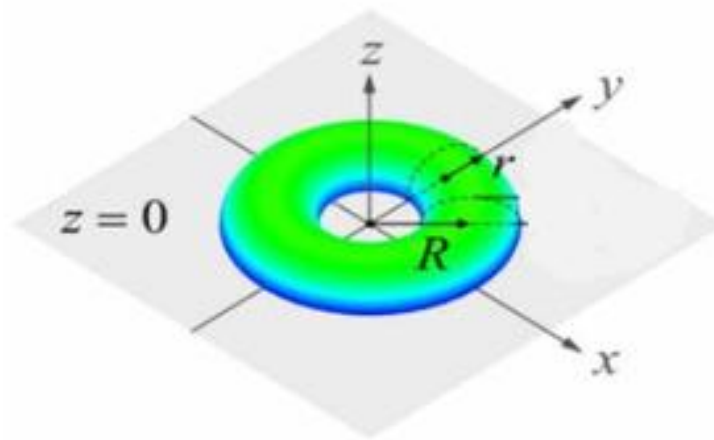


Figure 1.8: Geometry of quantum ring.

Quantum rings are highly prospective as the fundamental building block for numerous applications, including photonic detectors and sources, such as single-photon emitters, nanoflash memories, qubits for spintronic quantum computing, magnetic random access memory, recording medium, and other spintronic devices [29].

1.4 The Magneto-Caloric Effect (MCE)

The temperature change (heating or cooling) of a magnetic material brought on when subjected to magnetic field variation is known as the magnetocaloric effect. This effect has been known as adiabatic demagnetization. Warburg observed MCE in 1881. Debye and Giauque explained the origin of the MCE. They also suggested the using of

adiabatic demagnetization for reaching temperatures lower than the lowest achievable experimental temperature (temperature of liquid He) [31].

The great step towards room temperature magnetic refrigeration was covered by Brown's research, he developed a magnetic refrigerator with the help of metallic gadolinium. He achieved a temperature drop of 319 K to 272 K with a magnetic field fluctuation of 0 to 7 T in his prototype magnetic refrigerator.

The use of the MCE as an alternative technology for refrigeration is currently very popular, from room temperature to the temperatures of hydrogen and helium liquefaction (~ 20 -4.2 K). An alternative to the common vapor-cycle refrigeration technology today in use is magnetic refrigeration, which has the possibility to be energy-efficient and environmental friendly [31].

The thermodynamics is used to explain the magnetocaloric effect origin, that connects the magnetic variables (magnetic field and magnetization) to entropy and temperature. MCE is intrinsically shown in all magnetic materials, although the effect intensity depends on each material properties. The coupling of the magnetic sublattice to the applied magnetic field, which modifies the magnetic contribution to the solid's entropy, is the physical origin of the MCE [31].

The temperature change process through the magnetic field variation has been roughly described as follows: when the magnetic field is adiabatically applied to a usual ferromagnetic material, their magnetic moments become ordered, then the magnetic part of the total entropy is decreased. As a result, the crystalline lattice entropy should increase in order to keep the total entropy constant in the adiabatic process. Therefore, the material heats up. An opposite effect occurs and the material cools down if the magnetic field is adiabatically removed (Figure 1.9).

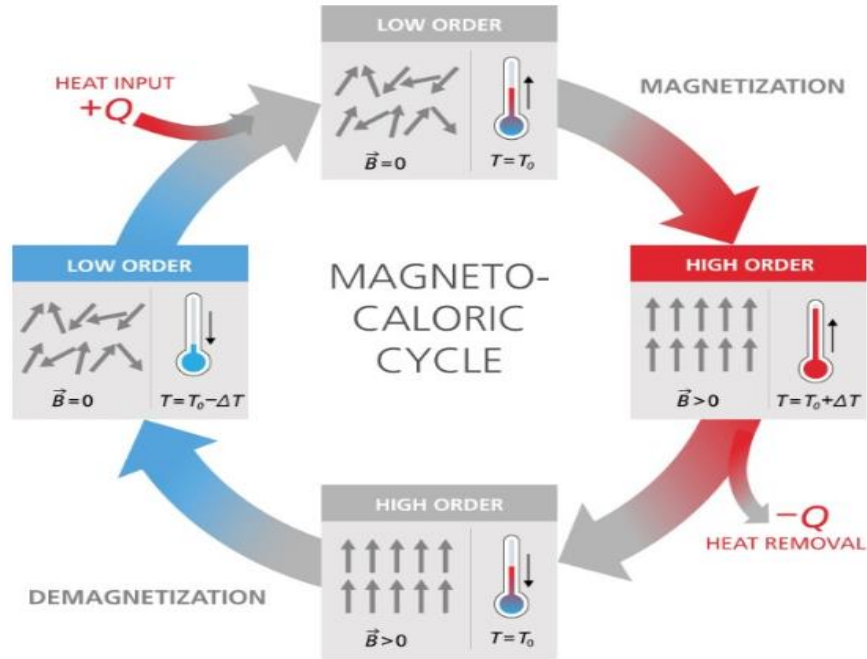


Figure 1.9: Schematic diagram of the magnetocaloric cycle.

There are some technological uses for the magnetocaloric effect. For example, the magnetocaloric effect can be used to physically treatment of some cancer types [32]. Such a use depends on the availability of biocompatible magnetic nanoparticles, which are mostly absorbed by malignant cells. Therefore, it is believed that these magnetic nanoparticles, when heated via magnetic field fluctuation, can destroy cancerous cells without harming healthy ones.

Nowadays, magnetic refrigeration is the primary application of the magnetocaloric effect. Magnetic refrigeration is an environmentally benign technique since it uses water or non-toxic fluids as the heat exchanger and magnetic compounds as the cooling materials. When compared to the common vapor cycle refrigerators, magnetic refrigerators are predicted to function with an energy savings of up to 30% [33].

1.5 Problem Statement

The study of QD/QR system is a challenge problem which has been under the focus of researchers. The previous works studied the thermodynamic and magnetic properties of QD system that subjected in parabolic-inverse squared potential modulated with modified Gaussian potential under the influence of magnetic field and impurities [34].

Other work studied the optical properties of the GaAs QD/QR systems subjected to same potentials [27].

Motivated by all previous researches, we investigate the effects of parabolic-inverse squared confinement potential modulated with modified gaussian potential on the electronic, thermal and magnetic characteristics of a 2D-QD/QR GaAs system (Figure 1.10) doped with donor/acceptor impurity. Here we have a system depending on different variables like magnetic field, temperature, hydrostatic pressure, confining frequency, confinement potential and the QD size.

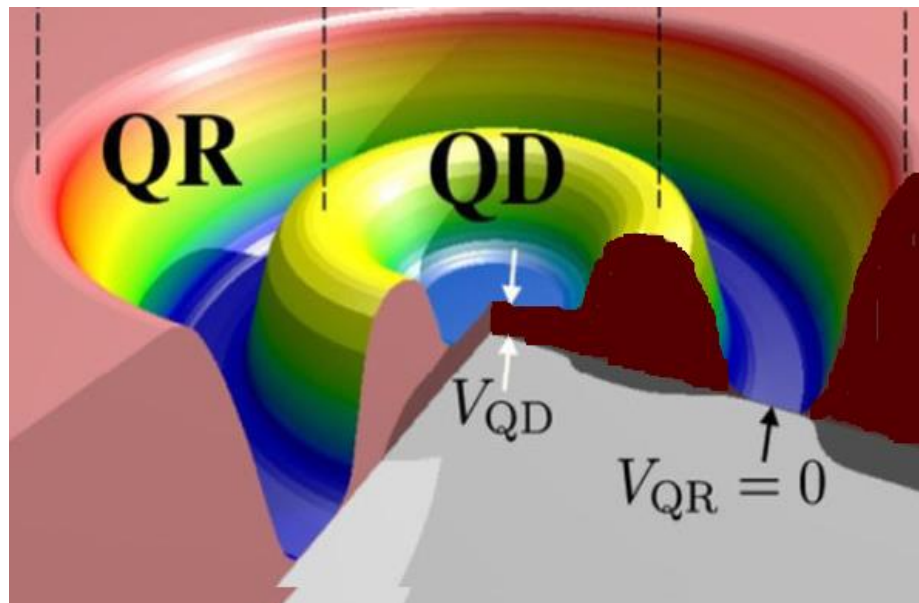


Figure 1.10: Schematic representation of quantum dot/quantum ring structure.

The Hamiltonian of the system is well defined. after fixing the Hamiltonian, analytical and simulation solution are to be used to solve the eigenvalue problem. The eigenenergy spectra of this system are derived within the framework of effective-mass and parabolic band approximation. One important step is to analyze the system statistically through the calculation of the partition function.

The electronic, thermal and magnetic properties of the system such as energy spectra, density of states, Helmholtz free energy, heat capacity, entropy, magnetization, magnetic susceptibility and magneto-caloric effect will be considered under the influence of changing temperature, magnetic field and impurity. This will carry out using

computational and analytical method. MATLAB program will be used for this purpose. The findings will be analyzed to determine the field of applications.

1.6 Thesis Layout

The five chapters that make up this thesis each focus on a different aspect of the investigation. Chapter One that titled with Introduction includes a general introduction about artificial atoms, nanotechnology, the quantum confinement of the charge carriers, density of state, quantum dots, quantum rings and magneto-caloric effect. In addition to an analysis of the problem statement. Chapter two provides the literature review for previous works related to this research and.

In chapter three which is titled with theoretical background, the theories of this study including the energy of the QD and QD/QR system was calculated including the effect of an external applied magnetic field and the confinement parameters taking into consideration the absence and presence of impurity. This is the starting point for thermodynamics quantities calculations, magnetic variables calculations and the density of state of QD/QR system.

In chapter four which is titled with results, the primary computational results and the theoretical behavior of all these physical characteristics were investigated and presented as a function of the magnetic field (B) and the temperature (T). Additionally, the pressure dependence of electronic properties has been investigated. Also, the results had been shown in figures and discussed in this chapter. The final chapter (chapter five) devoted to discussions, it summarizes the main findings, and suggests potential directions for future work.

Chapter Two: Literature Review

Most of theoretical studies focused on the energy spectra of few-electron QDs and QRs and used numerical and computational techniques, for example: A diagonalization method was used to obtain the energies and wave functions for a confined electron in the QRs region [27]. Comparing the results of a QR while taking the effects of an applied lateral electric field into account has a same direction disk-shaped heterostructure. In addition, using a diagonalisation technique investigated a two dimensional QR under lateral electric field and hydrostatic pressure [35], resulting from this that geometry and hydrostatic pressure are particularly effective instruments for adjusting a blue- or red-shift for the absorption spectrum, but the electric field effect can only be employed to generate the blue-shift.

The eigenvalues and eigenfunctions were calculated by the same numerical procedure under the combined effects of non-resonant intense laser and applied electric field [36]. The shallow impurity related nonlinear optical rectification (NOR) for a QR under applied magnetic fields had been studied by Bejan [37] using the variational method, results clearly show that the NOR is affected by the impurity position and magnetic field intensity.

In Similar, the effects of applied magnetic field on the linear, nonlinear, and total optical absorption coefficient together with the harmonic generation in QWs were investigated by Niculescu and Beja [38]. Systems called quantum well-wires (QWW) often have the passage of confined carriers in free direction.

A very powerful way to describe 0D systems like QDs is the combination of QRs by adiabatic approximation. Using the diagonalization and variational techniques, The effects of impurities, excitons, temperature, hydrostatic pressure, and external electric and magnetic fields in QWW, QDs, and quantum wells with the most varied geometries and stoichiometry were studied [39].

The study of impurities in semiconductor quantum dots (QDs) has attracted much attention recently, due to the fact that their presence can dramatically alter the performance of semiconductor devices and their optical, electrical and transport properties [40]. Therefore, it is vital to understand the nature of impurity states in semiconductor structures.

The conductivity of a semiconductor is greatly increased by shallow hydrogenic donors. To understand the optoelectronic properties of these heterostructures. Many researchers focused their attention on energy quantized states of the charge carriers to understand how a hydrogenic donor impurity affects the spectrum of a single electron in low-dimensional semiconductor structures [41-43]. In the presence of a hydrogenic donor impurity, the confinement of quasiparticles in QDs magnifies the strength of oscillator of electron-impurity excitations. It enables tuning of the optical transition energy's resonance frequency, which is affected by impurity presence and confinement strength.

Despite increased interest in impurity doping in nanocrystallites, variational techniques were used in the majority of theoretical investigations on shallow donors in spherical QD [44]. Moreover, the exact (numerical) wave functions and energies of a spherical nanocrystallite, with a shallow donor-impurity located anywhere inside are presented in [45].

A two-dimensional QD system doped with a hydrogenic donor impurity was examined to determine the effects of a parabolic-inverse squared confinement potential modulated with a modified Gaussian potential on the linear and nonlinear optical absorption and refractive index change coefficients. Also, the role of different confinement parameters and impurity on the optical absorption coefficient, and relative refractive index change were investigated [27].

The binding energy of donor impurities in QD's are influenced by the materials, geometry, shape and size. The impurity position along the heterostructures and the typical dimensions of the heterostructures may have a critical impact on the impurity binding energy. Particularly, Zhu et al. [46] and Perez- Merchancano et al. [47] conducted the first researches on the confinement effects on the impurity states in QDs. In these studies, the binding energies for the ground and excited states as a function of the impurity position and dot size were calculated.

In addition, the variational approach was used in [48] in order to calculate the binding energy of an on-center and off-center shallow hydrogenic impurity in a GaAs quantum dot under hydrostatic pressure. In addition to changing the charge carriers in the presence of hydrogenic impurities, it also alter when electric and magnetic fields are present.

The effective tools for studying the characteristics of impurities in semiconductor

QDs are the external fields. The effects of electric and magnetic fields on the impurity states in quantum pseudo dot (QPD) are studied recently. The Schrodinger equation for this potential has been the subject of different theoretical studies employing a variety of techniques, including the variational method, perturbation method [49] and the asymptotic iteration method (AIM) [50].

Moreover, simultaneous effects of electric field, pressure, temperature on the binding energy of an off center hydrogenic donor confined by spherical Gaussian potential had been considered based on the effective mass approximation within a matrix diagonalization scheme in [51]. Another research [52] had carried out the magnetic field effects on binding energies in spherical QD with finite confinement potential. Also, investigations are made into the energy spectrum, optical, and electromagnetic characteristics of a donor impurity confined by a pseudoharmonic electron confined by a 2D potential in the presence of a strong magnetic field [53, 54].

Recently, variational and exact diagonalization methods had been used by Elsaid et al. to study the electronic, thermodynamic and magnetic properties of single and coupled QDs [55, 56].

Chapter Three: Methodology

In this chapter, the model and method used in calculations that we have made will be discussed in detail in successive and sequential steps

3.1 Hamiltonian of Quantum Dot/Quantum Ring (QD/QR) System

The model considers an electron subjected to a parabolic-inverse square confinement potential with Gaussian modification $V(r)$ [57] and a perpendicular magnetic field B in z -direction. The Hamiltonian H_0 of such system is:

$$H_0 = -\frac{1}{2m^*} \left[-i\hbar\nabla + \frac{e}{c} \vec{A} \right]^2 + V(r) \quad 3.1$$

The stationary states of an electron are given by the eigen states of this Hamiltonian using the effective-mass approximation. The constant m^* is the effective mass within the lattice of the material, \hbar is the Planck constant, e is the electrical charge and c is the velocity of light. Using Coulomb gauge $[\vec{A} = (0, Br/2, 0)]$, where \vec{A} is the vector potential, B is the magnetic field. And $V(r)$ is the confinement potential. The form of the confinement potential that combines an inverse squared and a parabolic potential function assumes the form [58, 59].

$$V(r) = V_1(r) + V_{mgp}(r) \quad 3.2$$

The first term $V_1(r)$ is expressed by:

$$V_1(r) = \frac{1}{2} m^* \omega_0^2 r^2 + \frac{\hbar^2}{2m^*} \frac{\xi}{r^2} \quad 3.3$$

Where, ω_0 is the harmonic confinement frequency, r is the electron position and ξ being a dimensionless parameter, which characters the external field strength. Assuming $\xi > 0$ for a repulsive potential to get low energy bound state. The first term in equation (3.3) represent the potential of QD that confines electron in the centre, the second term represent the repulsive potential of quantum ring.

A modified Gaussian potential (V_{mgp}) is applied to the system. It can be further tuned to represent the confinement properties and the shape of specific quantum structures under study. Such potential is expressed as the power exponential potential (PEP) expressed such potential as follows:

$$V_{mgp}(r) = -V_0 \exp[-(r/R_0)]^q \quad 3.4$$

Here V_0 and R_0 are the depth and stretching range of the confinement potential, where R_0 can be assumed as the radius of the QD [57]. The potential will reduce to the Gaussian potential (GP) when choosing $q=2$. It is to be noted that the Gaussian potential (GP) is approximated by the anisotropic harmonic-oscillator (parabolic) potential near the QD centre for $r/R_0 \ll 1$ [60].

$$V_{mgp}(r) = -V_0 \left[1 - \left(\frac{r}{R_0} \right)^2 \right] \quad 3.5$$

Considering the model mentioned above, one can analytically acquire the energy eigenvalues and wave functions, thus H_0 turns out to be:

$$H_0 = -\frac{1}{2m^*} \left(-i\hbar\nabla + \frac{eBr}{c} \frac{\partial}{\partial \theta} \right) \left(i\hbar\nabla + \frac{eBr}{c} \frac{\partial}{\partial \theta} \right) + \frac{1}{2} m^* \omega_0^2 r^2 + \frac{\hbar^2}{2m^*} \frac{\xi}{r^2} - V_0 + \frac{V_0 r^2}{R_0^2} \quad 3.6$$

$$H_0 = -\frac{\hbar^2}{2m^*} \left(\frac{\partial^2}{\partial r^2} + \frac{1}{r} \frac{\partial}{\partial r} + \frac{1}{r^2} \frac{\partial^2}{\partial \theta^2} \right) + \frac{i\hbar}{2m^*} \frac{eB}{c} \frac{\partial}{\partial \theta} - \frac{1}{2m^*} \frac{e^2 B^2 r^2}{c^2} + \frac{1}{2} m^* \omega_0^2 r^2 + \frac{\hbar^2}{2m^*} \frac{\xi}{r^2} - V_0 - \frac{V_0 r^2}{R_0^2} \quad 3.7$$

$$H_0 = -\frac{\hbar^2}{2m^*} \left(\frac{\partial^2}{\partial r^2} + \frac{1}{r} \frac{\partial}{\partial r} + \frac{1}{r^2} \frac{\partial^2}{\partial \theta^2} \right) + \frac{1}{2} m^* \left(\omega_0^2 + \frac{\omega_c^2}{4} \right) r^2 - \frac{V_0 r^2}{R_0^2} - V_0 - i\hbar \frac{\omega_c}{2} \frac{\partial}{\partial \theta} + \frac{\hbar^2}{2m^*} \frac{\xi}{r^2} \quad 3.8$$

Or,

$$H_0 = -\frac{\hbar^2}{2m^*} \left(\frac{\partial^2}{\partial r^2} + \frac{1}{r} \frac{\partial}{\partial r} + \frac{1}{r^2} \frac{\partial^2}{\partial \theta^2} \right) + \frac{1}{2} m^* \Omega^2 r^2 - V_0 - i\hbar \frac{\omega_c}{2} \frac{\partial}{\partial \theta} + \frac{\hbar^2}{2m^*} \frac{\xi}{r^2} \quad 3.9$$

Define

$$\Omega^2 = (\omega_0^2 + \omega_c^2/4 + 2V_0/m^*R_0^2) \quad 3.10$$

Ω is the effective frequency, with ω_c is cyclotron frequency given by:

$$\omega_c = eB/m^* \quad 3.11$$

The model Hamiltonian sensibly represents a 2D-QD with a single carrier electron [16]. 2D-QD means the charge carriers are confined in a plane, typically in the x-y plane, with their motion confined in all directions within that plane.

The confinement potential form coincides to kind of electrons lateral electrostatic confinement (parabolic) in the xy plane [61, 62].

The time-independent Schrödinger equation becomes:

$$H_0\psi^0 = E^0\psi^0 \quad 3.12$$

Where ψ^0 is the eigenstate of pure QD with the absence of impurity, and E^0 is the corresponding eigenvalue. ψ^0 is customary proposed as:

$$\psi^0(r, \theta) = \chi(r) \frac{e^{im\theta}}{\sqrt{2\pi}} \quad 3.13$$

Here m is magnetic quantum number. By substituting equation (3.13) in equation (3.12), it turns out to be:

$$\left[-\frac{\hbar^2}{2m^*} \left(\frac{\partial^2}{\partial r^2} + \frac{1}{r} \frac{\partial}{\partial r} + \frac{1}{r^2} \frac{\partial^2}{\partial \theta^2} \right) + \frac{1}{2} m^* \Omega^2 r^2 - V_0 - i\hbar \frac{\omega_c}{2} \frac{\partial}{\partial \theta} + \frac{\hbar^2}{2m^*} \frac{\xi}{r^2} \right] \chi(r) \frac{e^{im\theta}}{\sqrt{2\pi}} = E^0 \chi(r) \frac{e^{im\theta}}{\sqrt{2\pi}} \quad 3.14$$

Cancelling equal terms in both sides of the equation,

$$\left[-\frac{\hbar^2}{2m^*} \left(\frac{\partial^2}{\partial r^2} + \frac{1}{r} \frac{\partial}{\partial r} + \frac{m^2}{r^2} \right) + \frac{1}{2} m^* \Omega^2 r^2 - V_0 + \frac{m\omega_c \hbar}{2} + \frac{\hbar^2}{2m^*} \frac{\xi}{r^2} \right] \chi(r) = E^0 \chi(r) \quad 3.15$$

$$\frac{d^2 \chi(r)}{dr^2} + \frac{1}{r} \frac{d\chi(r)}{dr} + \left[\alpha^2 - \frac{\beta^2}{r^2} - \Omega^2 r^2 \right] \chi(r) = 0 \quad 3.16$$

Where α and β are defined as

$$\alpha^2 = \frac{2m^*(E + V_0)}{\hbar^2} - \frac{meB}{\hbar} \quad 3.17$$

$$\beta^2 = m^2 + \xi \quad 3.18$$

The below relations is employed

$$\chi(r) = r^\beta e^{-\frac{\Omega r^2}{2}} h(r), \quad 3.19$$

$$x = \Omega r^2 \quad 3.20$$

It yields

$$\frac{d^2 h(x)}{dx^2} + [\beta - x + 1] \frac{dh(x)}{dx} + nh(x) = 0 \quad 3.21$$

Where $h(x)$ is the Henkel function, the solution is denoted by $h(x) = L_n^\beta(x)$ and n is an integer expressed as:

$$n = \frac{\alpha^2}{4\Omega} - \frac{\beta + 1}{2} \quad 3.22$$

After several steps with help of software, the energy eigenvalue was finally found to be [27]:

$$E_{mn}^0 = \left(2n + \sqrt{m^2 + \xi} + 1\right) \hbar\Omega + \frac{m\hbar\omega_c}{2} - V_0 \quad 3.23$$

Where E_{mn}^0 is the energy eigenvalue of unperturbed QD/QR system and n is the principle quantum number.

3.2 Impurity Effect

In this research the system is considered to be doped with a hydrogenic impurity [63]. When the potential of impurity is added to the Hamiltonian, it becomes:

$$H(r) = H_0(r) + H'(r) \quad 3.24$$

$$H'(r) = V_{imp}(r) = -e^2/4\pi\epsilon\epsilon_0 r = \kappa k/r \quad 3.25$$

Where ϵ , ϵ_0 are the dielectric constant of the medium and permittivity of the vacuum, respectively. $k = -e^2/4\pi\epsilon\epsilon_0$ and $\kappa = 0$ without impurity, $\kappa = +1$ for attractive donor impurity and $\kappa = -1$ for repulsive acceptor impurity, r denotes the electron-impurity distance.

The time-independent Schrödinger equation now is:

$$H(r)\psi_{mn} = (H^0 + H')\psi_{mn} \quad 3.26$$

$$H(r)\psi_{mn} = \left(H^0 + \frac{\kappa k}{r}\right)\psi_{mn} \quad 3.27$$

$$H(r)\psi_{mn} = E_{mn}\psi_{mn} \quad 3.28$$

Where, ψ_{mn} is the eigenfunction of the perturbed QD system and E_{mn} is the corresponding energy eigenvalue which can be derived by the perturbation method:

$$E_{mn} = E_{mn}^0 - \langle \psi_{mn}^0 | H' | \psi_{mn}^0 \rangle \quad 3.29$$

The impurity spectrum is given by [63],

$$E_{mn} = \left(2n + \sqrt{m^2 + \xi} + 1\right) \hbar\Omega + \frac{m\hbar\omega_c}{2} - V_o - \frac{k}{\Omega_1} \frac{1}{\sqrt{2n + \sqrt{m^2 + \xi} + 1}} \quad 3.30$$

$$\text{Where, } \Omega_1 = \sqrt{\hbar/m^*\Omega} \quad 3.31$$

3.3 The Binding Energy (E_b)

The binding energy is an important quantity in physics, which is defined as:

$$E_b = E_{\text{without impurity}} - E_{\text{with impurity}} \quad 3.32$$

The binding energy is amount of energy required to separate a particle from a system of particles or to disperse all the particles of the system.

3.4 The Density of States (DoS)

The density of states in quantum dots and quantum rings is a fundamental concept in nanotechnology, which is influenced by quantum confinement, resulting in discrete energy levels. It is essential for understanding optical and electronic properties in these nanostructures, Making them important in quantum computing and optoelectronic devices applications. DoS can be expressed as a sum of δ functions:

$$DoS = \sum_i \delta(E - E_n) \quad 3.33$$

Where E_n are the discrete energy levels of the quantum dot, DoS is numerically calculated with a Gaussian distribution as:

$$DoS = \sum_i \frac{eB}{h} \times \frac{1}{\sqrt{2\pi}\Gamma(B)} \times \exp\left(\frac{-(E - E_n)^2}{2\Gamma^2(B)}\right) \quad 3.34$$

Where,

$$\Gamma(B) = \frac{\hbar e}{m^*} \sqrt{\frac{2B}{\pi\mu^h}} \quad 3.35$$

is the broadening factor, with μ^h is the hole mobility at zero magnetic field. The prefactor

eB/h accounts for the orbital degeneracy [64].

3.5 Thermodynamic Properties

In order to calculate thermodynamic properties of the system, the partition function, denoted by Z , is built. It is a fundamental quantity in statistical mechanics that characterizes the equilibrium properties of a system. Z is obtained by direct summation over all possible states available to the system, weighted by their Boltzmann factors. When dealing with a quantum system, the energy spectra of single electrons in the system are taken into consideration in order to determine the partition function [65]:

$$Z(n, m, B, \omega_0, V_0, R_0, \xi, T) = \sum_{mn} e^{-\beta E_{mn}} \quad 3.36$$

Where $\beta = 1/k_\beta T$, k_β is Boltzmann constant that is $8.672 \times 10^{-5} \text{ eV.K}$ and T is the temperature in Kelvins.

3.5.1 Statistical Average Energy $\langle E \rangle$

The average energy was calculated from the statistical energy expression:

$$\langle E(n, m, B, \omega_0, V_0, R_0, \xi, T) \rangle = \frac{\sum_{mn} E_{mn} e^{-\beta E_{mn}}}{Z} \quad 3.37$$

This expression allows us to determine the average energy with the temperature and the system's energy levels. The average energy is the expectation value of the energy operator over all possible states of the system. It represents the average value of the energy that the system possesses [65].

3.5.2 Helmholtz Free Energy (F)

The Helmholtz free energy (F) is a fundamental thermodynamic potential that measures the amount of useful work that may be obtained from a closed system at constant volume and temperature. The Helmholtz free energy is closely related to the partition function (Z) of the system. It can be expressed as [66]:

$$\langle F(n, m, B, \omega_0, V_0, R_0, \xi, T) \rangle = -k_B T \ln Z(n, m, B, \omega_0, V_0, R_0, \xi, T) \quad 3.38$$

This equation emphasizes the importance of statistical mechanics in providing a microscopic interpretation of thermodynamic quantities and is particularly useful in systems where the volume is held constant, allowing for a comprehensive analysis of energy and entropy contributions.

3.5.3 Specific Heat (C_v)

The specific heat is considered as the most important thermal property, which measures the heat stored in the quantum dot system. It is defined as the amount of heat that is required to raise the material's temperature by one degree [66]. Specific heat is equal to the derivative of the average energy with respect to temperature.

$$C_v(n, m, B, \omega_0, V_0, R_0, \xi, T) = \frac{\partial \langle E(n, m, B, \omega_0, V_0, R_0, \xi, T) \rangle}{\partial T} \quad 3.39$$

3.5.4 Entropy (S)

Entropy of a system indicates to the degree of disorder or randomness in the system and depends on the number of possible microstate for the system and its partition function. It provides information about the configuration and arrangement of the locations and energies of the atoms or molecules that involve a system as the following [67]:

$$S(n, m, B, \omega_0, V_0, R_0, \xi, T) = \frac{\partial k_B T \ln \langle Z(n, m, B, \omega_0, V_0, R_0, \xi, T) \rangle}{\partial T} \quad 3.40$$

3.5.5 Magneto-Caloric Effect (MCE)

The magneto-caloric effect describes how magnetic materials react, at a specific temperature, to an external magnetic field. This is an interesting property of magnetic materials: when the magnetic field changes, they can either exchange heat with a thermal reservoir or change their temperature. Two quantities apply when characterizing the magneto-caloric effect. The first one is the magneto-caloric potential (ΔS), and the second one is the temperature change (ΔT). Thus, the magnetic entropy change is obtained from the entropy which was evaluated above, with and without magnetic field. For an isothermal process, ΔS is given by [33]:

$$\Delta S = S(B \neq 0 T) - S(B = 0 T) \quad 3.41$$

3.6 Magnetic Properties

3.6.1 The Magnetization (M)

The magnetization is one measure of the magnetic properties of a material, it results from the magnetic moment, which is caused by the motion of electrons in the atoms or the spin of electrons or the nuclei. The magnetization is caused by the material response to the applied magnetic field, together with any unbalanced magnetic dipole moment which is inherent in the material due to its electrons motion.

When a magnetic field is applied, it influences the energy levels of the electrons within the system, leading to changes in the average mean energy of the system. So, magnetization can be calculated from the average energy according to the following relation [34]:

$$M(n, m, B, \omega_0, V_o, R_0, \xi, T) = - \frac{\partial \langle E(n, m, B, \omega_0, V_o, R_0, \xi, T) \rangle}{\partial B} \quad 3.42$$

3.6.2 The Magnetic Susceptibility (χ)

Another important physical quantity is the magnetic susceptibility (χ). χ is defined as the change of the magnetization as the magnetic field (B) varies. It shows whether the material is attracted to the magnetic field ($\chi > 0$), in this case a material can be classified as paramagnetic. These materials are temperature dependent. Oxygen, aluminium and Alkaline earth metal are some of the examples of paramagnetic materials. When the material is called diamagnetic, it will be repulsive to the magnetic field ($\chi < 0$),. These materials are independent of temperature, water, gold and mercury are examples of diamagnetic materials.

On the other hand, when the magnetic susceptibility has very high and positive value and it depends on the applied field, the materials are known as ferromagnetic materials. Iron and nickel are examples of these materials. The susceptibility relates to the magnetization by the following equation [68].

$$\chi(n, m, B, \omega_0, V_o, R_0, \xi, T) = \frac{\partial M(n, m, B, \omega_0, V_o, R_0, \xi, T)}{\partial B} \quad 3.43$$

3.7 The Dependence of Dielectric Constant and Effective Mass on the Hydrostatic Pressure and Temperature

The hydrostatic and temperature dependent effective mass $m^*(P, T)$ and dielectric constant $\varepsilon(P, T)$ of GaAs are given by [69]:

$$\frac{m_e}{m^*(P, T)} = 1 + E_p^\Gamma \left(\frac{2}{E_p^\Gamma(P, T)} + (E_p^\Gamma(P, T) + \Delta_0)^{-1} \right) \quad 3.44$$

Where m_e is the free electron mass, E_p^Γ is the energy related to the momentum matrix element equals 7.51 eV, Δ_0 is the spin-orbit splitting equals 0.341 eV and $E_p^\Gamma(P, T)$ is GaAs energy gap at Γ point which is given by:

$$E_p^\Gamma(P, T) = E_p^\Gamma(0, T) + bP + cP^2 \quad 3.45$$

And,

$$E_p^\Gamma(0, T) = 1.519 - \frac{5.405 \times 10^{-5} T^2}{(T + 204)} \quad 3.46$$

$$b = 1.26 \times 10^{-1} \text{ eV/GPa and } c = -3.77 \times 10^{-3} \text{ eV/(GPa)}^2$$

The dependence of dielectric constant on pressure and temperature is given as:

$$\varepsilon(P, T) = \begin{cases} 12.74 \exp(-1.73 \times 10^{-3} P) \exp[9.4 \times 10^{-5} (T - 75.6)] & T \leq 200K \\ 13.18 \exp(-1.73 \times 10^{-3} P) \exp[9.4 \times 10^{-5} (T - 200)] & T \geq 200K \end{cases} \quad 3.47$$

3.8 Simulation Approach

This thesis builds the simulation approach using MATLAB, a powerful computing environment renowned for its abilities in numerical analysis, data visualization, and algorithm building. Researchers may more easily model complicated systems and produce intricate simulations that are suited to particular research topics with the help of of MATLAB's comprehensive functionalities.

This study intends to investigate and evaluate a variety of scenarios pertinent to the research objectives by utilizing MATLAB's powerful computing capabilities. Because it facilitates the real-time viewing of results and the manipulation of parameters, which

enhances understanding of system behavior, MATLAB is an essential tool in the search of meaningful insights and conclusions throughout this investigation.

Initially, the eigen energy of GaAs QD/QR system in the absence of impurity was obtained by programming equations (3.10), (3.11) and (3.23), all parameters submitted in the equations are provided in chapter three (entered as constant numbers in the program). Equation (3.30) was coded to examine the impurities effect on the system.

Additionally, the binding energy and the density of the levels was determined by programming equations (3.23) and (3.34).

Later, all previous steps were repeated to investigate the effect of hydrostatic pressure on the electronic properties of the system by entering the values of dielectric constant and effective mass of GaAs as functions of pressure and temperature not as numbers. This was obtained by programming the equations in section (3.7) before equation (3.23).

The research of thermodynamic properties became the main focus after the electronic properties. After programming a partition function, the average energy was determined by programming equation (3.37), using the general definition of the derivative. Equation (3.39) was then programmed to get the specific heat capacity, using the derivative of the average energy with respect to temperature.

Equation (3.40) was programmed using MATLAB to investigate the entropy of the QD/QR system, taking note that any derivative was implemented in MATLAB using the general definition of the derivative. Following the examination of thermodynamic properties, attention turned to using equation (3.41) to program in order to investigate the phenomena of the magneto-caloric effect.

By programming equations (3.42) and (3.43), the magnetic characteristics of the system were examined in the thesis. This allowed for the determination of the magnetization and the magnetic susceptibility, respectively.

In summary, the efficiency and accuracy of the analysis have been much improved by the use of MATLAB throughout the computations. A greater comprehension of the behavior of the system was made possible by the methodical derivation of essential electric, thermodynamic, and magnetic properties through the programming of key equations. MATLAB's incorporation into the thesis was quite helpful in handling the complex calculations required to investigate the relevant physical processes.

Chapter Four: Results

This chapter presents the computed numerical results for the energy spectra (E_{mn}), binding energy (E_b), density of states (DoS), average energy ($\langle E \rangle$), Helmholtz free energy ($\langle F \rangle$), specific heat (C_v), entropy (S), magneto-caloric effect (MCE), magnetization (M) and magnetic susceptibility (χ) for GaAs QD/QR system presented in the perpendicular magnetic field, taking into account the absence of impurity and the doping process with donor/acceptor impurity. The material parameters for GaAs in this work have been chosen to be: $m^* = 0.065m_0$ and $\varepsilon = 12.4\varepsilon_0$ [27].

4.1 Electronic Properties

4.1.1 Energy Spectra (E_{mn})

Firstly, in this work, the energy spectra with and without impurity of GaAs QD/QR system were calculated using equations 3.23 and equation 3.30. In Figures 4.1–5, the energy (E_{mn}) of the two lowest confined electron states ($n= 1$ and 2 , $m= 0$) in a GaAs QD ($\zeta= 0$) and QD/QR ($\zeta= 1$) is found for several values of the κ -parameter: without impurity ($\kappa= 0$), with donor impurity ($\kappa= +1$) and with acceptor impurity ($\kappa= -1$). The results are shown in each figure by changing one parameter, leaving the others fixed. The variations in the parameters have been chosen to be consistent with the effective Bohr radius in GaAs ($a_0 = 10$ nm) have been chosen [70]. This means that the sizes of the QD (or QR) are of the order of 10 nm.

The energy of the lowest two-confined electron states for an electron that is confined in the QD and QD/QR as a function of the external magnetic field in a range from 0 to 40 T is presented in Figure 4.1. Calculations are without impurity and with donor and acceptor impurities for $\omega_0= 10$ THz, $V_0= 30$ meV, $R_0= 15$ nm, $\zeta= 0$ in and $\zeta= 1$ in Figure 4.1 (a) and (b). The presence of the donor impurity reduces the energy of the electron due to the attractive energy contribution in QD and the acceptor impurity increases the energy. The behavior of energy spectrum is the same in (a) and (b) with small different values.

In the absence and presence of impurity, the energies of ground state and first excited state increase with increasing the magnetic field. For the three cases of impurity, a greater extension over space are observed for the excited state than those for ground state, which is most sensitive to the effects of the perpendicular magnetic field. This effect must be understood in light of the fact that the applied magnetic field is responsible for two effects: The first one is that there is an additional parabolic confinement to the one that already exists due to the presence of ω_0 (see the second term in equation 10), and the second effect is a rigid displacement of the energy towards higher or lower energies, depending on the quantum number m . So this is only becomes visible on the excited state because of its non-zero value of the m -quantum number [27].

The more extended a state in space, the more sensitive it will be to the variations in the parabolic potential height that confines it. The confinement is enhanced and the electronic wave functions are shrunk to a smaller region of space located around the center of the structure with an enhancement of the magnetic field. As a result, the energy also increases [27].

The energy increases as the QR is added to the QD disk this is because the QR has an annular geometry where electrons are confined in a ring-like potential. This adds larger orbital paths and more pronounced interactions with the magnetic field, causing more substantial shifts in energy as magnetic field increases.

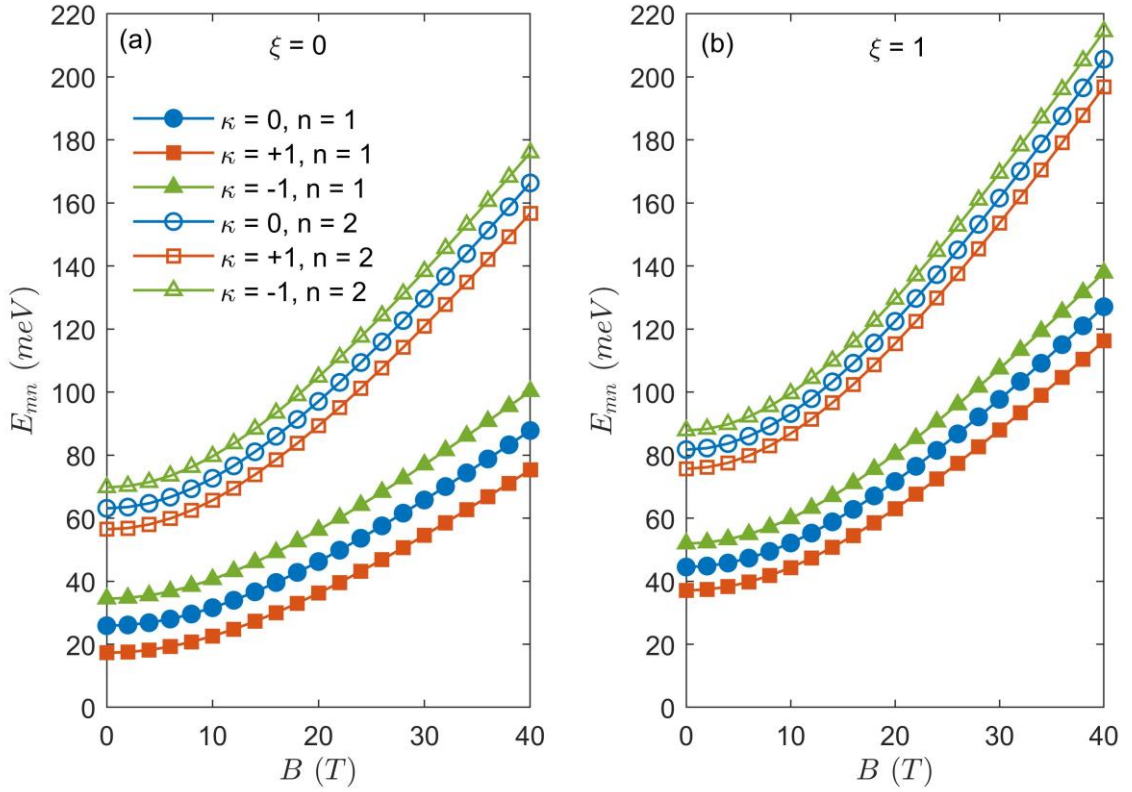


Figure 4.1: Energy of the lowest two confined states for a confined electron versus the applied magnetic field for (a) QD ($\xi=0$) and (b) QD/QR ($\xi=1$).

Figure 4.2 presents the same energies as a function of ω_0 -frequency in a range from 0 to 80 THz. Calculations are without impurity and with donor and acceptor impurities for $B=5$ T, $V_0=30$ meV, $R_0=15$ nm, $\xi=0$ and $\xi=1$ in Figure 4.2 (a) and (b). The energy is increasing with frequency and this behavior of energy spectrum is the same in (a) and (b) with small different values.

Considering the data presented in the Figure 4.2 (b), in the absence of impurity ($\kappa=0$), the energy of ground state increases from 42 meV to 193 meV, while the energy of first excited state increases from 78 meV to 305 meV. For donor impurity ($\kappa=+1$), the energy of ground state increases from 35 meV to 180 and the energy of first excited state rises from 72 meV to 294 meV. If impurities are acceptors ($\kappa=-1$), the ground state increases its energy from 50 meV to 205 meV, while the first excited state increases its energy from 84 meV to 315 meV. Here the discussions of Figure 4.1 would be useful for both the ground and the first excited states.

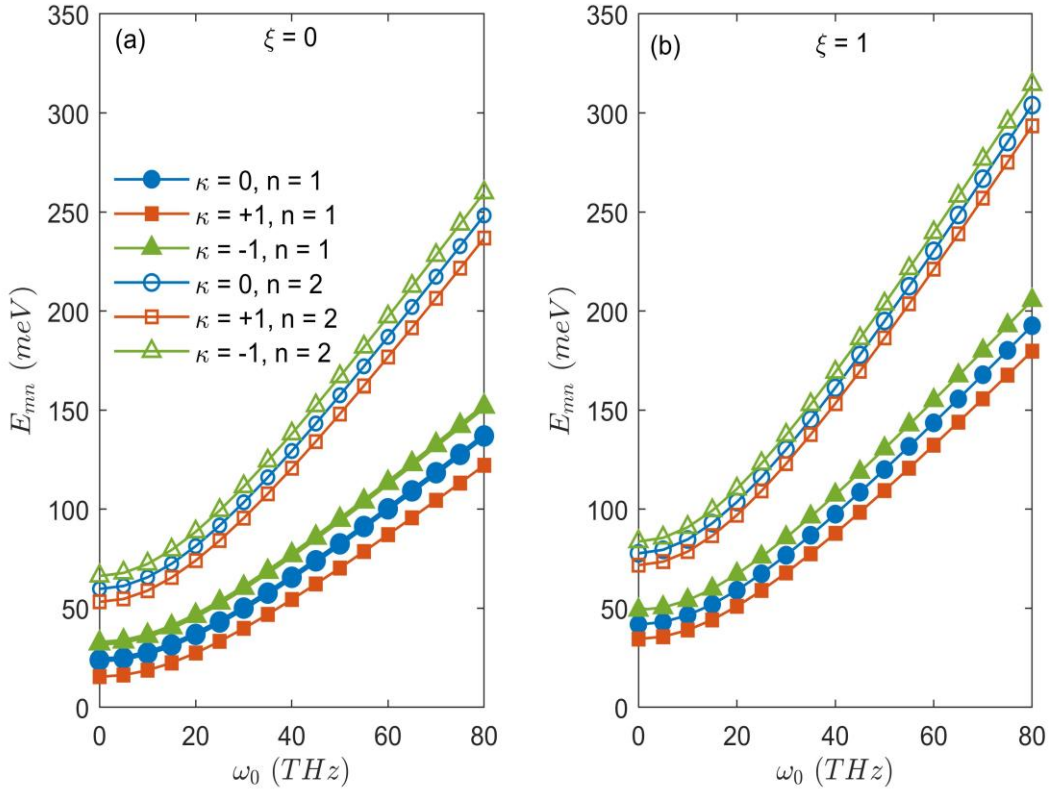


Figure 4.2: Energy of the lowest two confined states for a confined electron versus the ω_0 -frequency for (a) QD ($\xi=0$) and (b) QD/QR ($\xi=1$).

Figure 4.3 shows the energy of the lowest two confined electron-impurity states for a confined electron in the QD ($\xi=0$) and QD/QR ($\xi=1$) as a function of V_0 -potential in a range from 0 to 100 meV. Calculations are without impurity and with donor and acceptor impurities for $B=5$ T, $\omega_0=10$ THz and $R_0=15$ nm. The behavior of energy spectrum is the same in (a) and (b) with different values.

By increasing the potential, the energies of two states in the QD case begin to increase then they are decreasing the energies. The ground state is most sensitive to the difference in the potential V_0 and it exhibits the same behavior by adding the QR, whereas the energy of first excited state does not affected by increasing the potential in the range of 50-100 meV.

The reason for the decreasing character of the energies as the potential V_0 rises is that as the potential increases, the bottom of the potential well moves to lower energies thereby reducing the energy of the confined states [27].

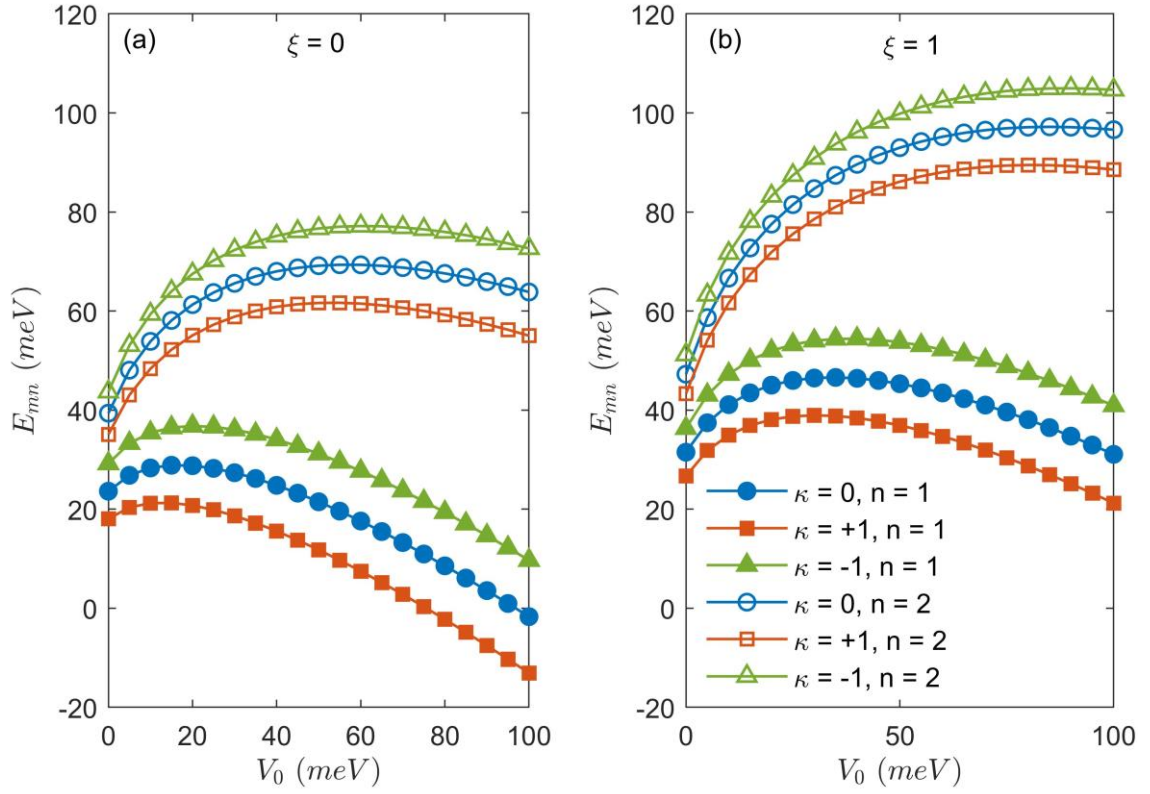


Figure 4.3: Energy of the lowest two confined states for a confined electron versus the V_0 -potential for (a) QD ($\xi=0$) and (b) QD/QR ($\xi=1$).

Figure 4.4 describes the energy of the lowest two confined electron states for an electron confined in the QD and QD/QR as a function of R_0 -radius in a range from 3 to 30 nm. Calculations are without impurity and with donor and acceptor impurities for $B=5$ T, $\omega_0=10$ THz, $V_0=30$ meV. The behavior of energy spectrum is the same in (a) and (b) with small different values.

As R_0 increases, both ground and first excited energy decrease because the electron becomes less confined and shifts towards lower energies at the potential well bottom [27].

The first excited state is most sensitive to variations of the quantum dot radius (R_0). Figure 4.4 clearly shows that the excited state with and without impurity presents its largest differences in energy for R_0 range and justifies the small variations of the ground state. It is also observed that there is a weak influence of impurity on both states energies with increase in R_0 .

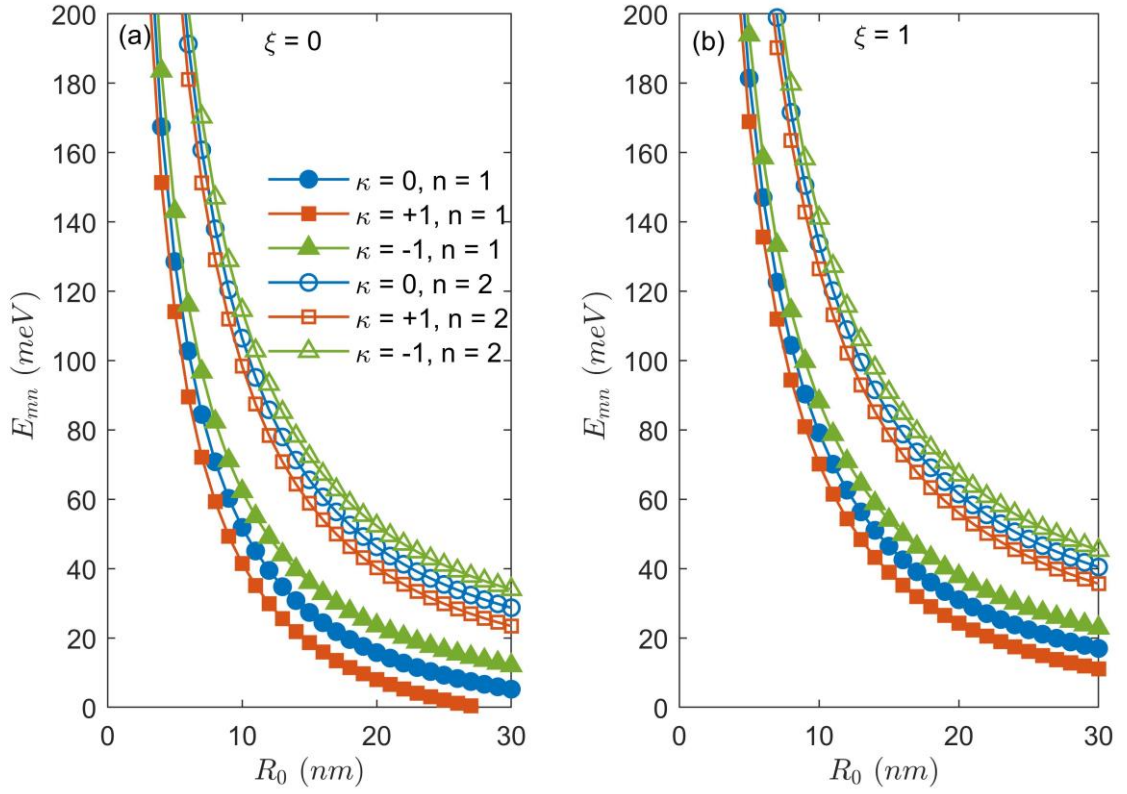


Figure 4.4: Energy of the lowest two confined states for a confined electron versus the R_0 -radius for (a) QD ($\xi=0$) and (b) QD/QR ($\xi=1$).

Figure 4.5 depicts the energy of the lowest two confined electron states for a confined electron in the 2D-QD/QR against the ξ -parameter in a range from 0 to 5. Calculations are without impurity and with donor and acceptor impurities for $B=5$ T, $\omega_0=10$ THz, $V_0=30$ meV and $R_0=15$ nm. For $\kappa=0$, the ground state and the first excited energies are increasing with ξ -parameter

When ξ goes from zero to one i.e. when the system evolves from a 2D-quantum disk to a 2D-quantum ring, the highest variations for the first excited state energy occur. An increase in ξ consequently raises the inner radius of the annular region where the carriers are confined as well as the repulsive potential at the center of the structure. Since the outer radius of this annular zone remains relatively constant (depending on the parabolic potentials), a greater confinement of the electron and in turn a shift of the energy towards higher values are predicted [27].

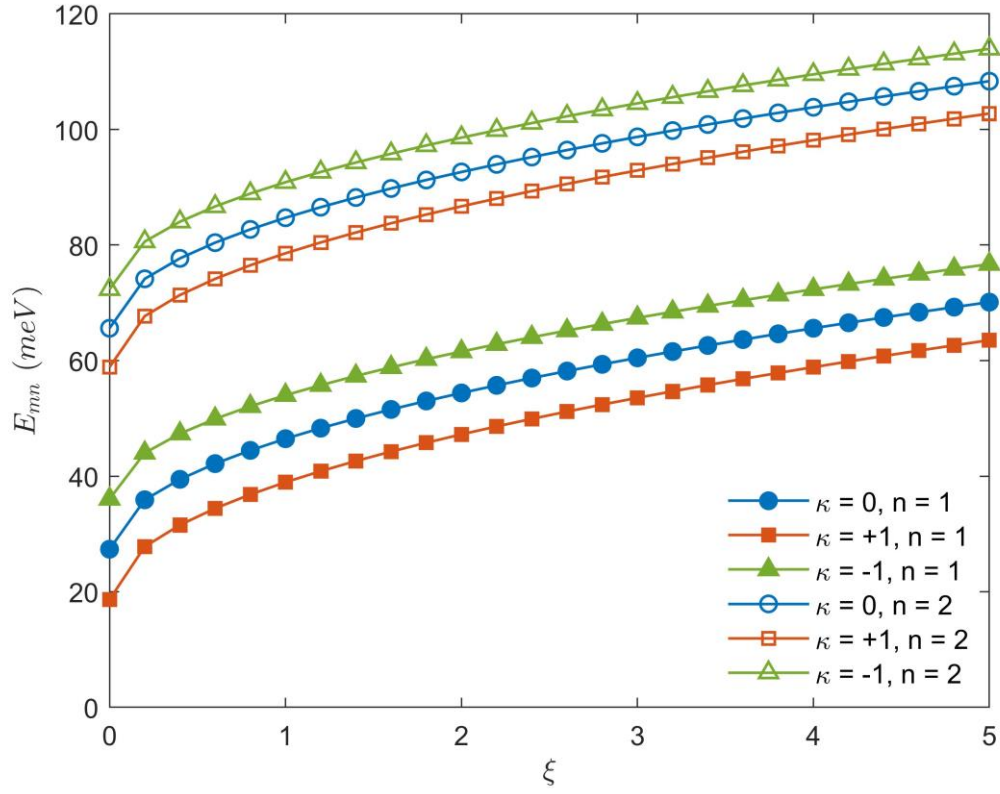


Figure 4.5: Energy of the lowest two confined states for a confined electron in the 2D-QD/QR versus the ζ -parameter.

Now, The behavior of E_{mn} as a function of applied magnetic field with three different values of V_0 -potential (10 meV, 30 meV, 80 meV) is illustrated in Figure 4.6, taking a special case of ground state ($n = 1$) with $\omega_0 = 10$ THz, $R_0 = 15$ nm, $\kappa = +1$ and $\zeta = 1$. As it is seen from the figure that in the variation range of magnetic field from 0 to 40 T, E_{mn} spectra decrease by rising the value of V_0 at a fixed value of B with the same behavior.

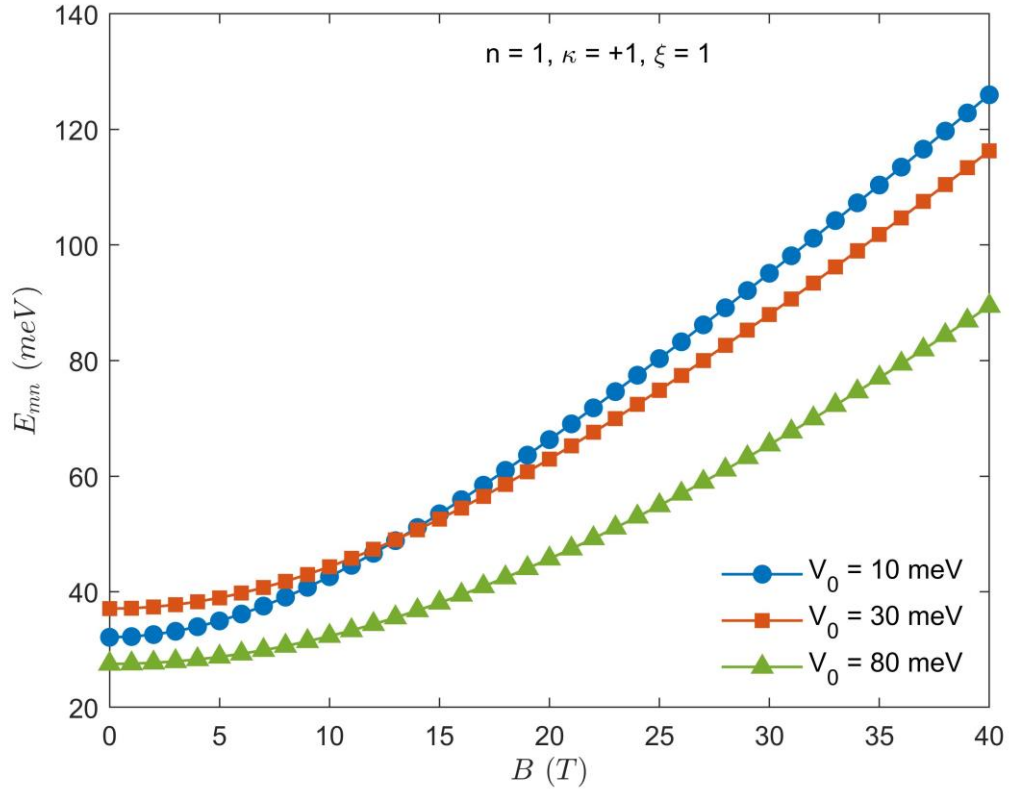


Figure 4.6: Energy of the lowest confined state for a confined electron in the 2D-QD/QR versus the magnetic field for different values of V_0 -potential.

4.1.2 Binding Energy (E_b)

The binding energy of the donor impurity has been calculated under several QD physical parameters. Figure 4.7 (a) shows the variations of the ground state and first excited state binding energies with applied magnetic field for $\omega_0 = 10$ THz, $V_0 = 30$ meV, $R_0 = 15$ nm, $\kappa = +1$ and $\xi = 1$. E_b rises with increasing the magnetic field. Note that there are two effects of the magnetic field. Equation (3.30) illustrates how it produces parabolic confinement and energy displacement toward higher or lower energies. This displacement does not exist for the ground state binding energy. The confinement rises and the electron wave function is localized in a smaller region as the magnetic field increases. As a result, the binding energy rises and the distance between the electron and impurity decreases [71].

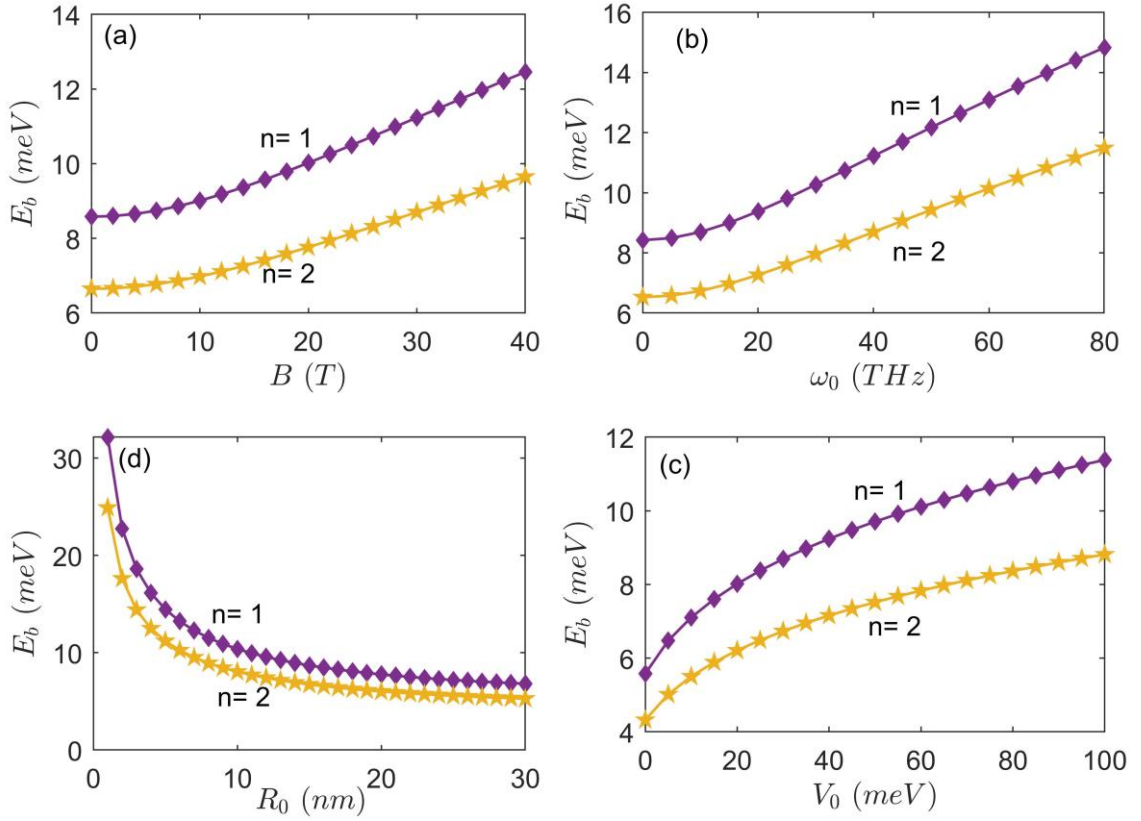


Figure 4.7: The ground state and the first excited state binding energies versus (a) magnetic field, (b) the confining frequency, (c) the potential and (d) the radius.

In Figure 4.7 (b), the variations of the ground state and first excited state binding energies with the confinement frequency ω_0 are plotted with $B=5$ T, $V_0=30$ meV, $R_0=15$ nm, $\kappa=+1$ and $\zeta=1$. As can be seen, E_b increases with rising the confinement frequency. The wave function extends a smaller region thereby the distance between electron and impurity reduces with increasing the confinement frequency. This means that the binding energy increases [71].

Figure 4.7 (c) shows the variations of the binding energies of the ground state and first excited state with the depth of potential V_0 for $B=5$ T, $\omega_0=10$ THz, $R_0=15$ nm, $\kappa=+1$ and $\zeta=1$. As the potential depth increases, E_b rises. The bottom of the well shifts toward smaller energies and the confined states energy increases when the potential depth increases. Hence, the distance between the impurity and electron reduces. Thereby the binding energy increases [71].

Finally, the variations of the ground state and first excited state binding energies with the range of radius R_0 for $B=5$ T, $\omega_0=10$ THz, $V_0=30$ meV, $\kappa=+1$ and $\zeta=1$ are

presented in Figure 4.7 (d). With rising the radius range, the binding energy reduces. This is because when the radius is increasing, the wave function extends a greater region thereby the distance between electron and impurity rises [71].

To compare the difference between the values of the binding energy for larger values of R_0 , the ground state binding energy with the range of potential $R_0=0-50$ nm and $R_0=50-200$ nm for $B=5$ T, $\omega_0=10$ THz, $V_0=30$ meV, $\kappa=+1$ and $\xi=1$ are plotted in Figure 4.8 (a) and (b), respectively. It is observed that there is a slight variation between the binding energy values for different values of confinement potential. The binding energy increases with enhancing the potential depth at a fixed potential range. This is because a deeper potential traps the carriers more effectively and leads to lower energy bound states, more energy is required to free them from the quantum confinement. The system's size remains constant at fixed potential range, so the potential depth is the dominant factor influencing the increase in binding energy.

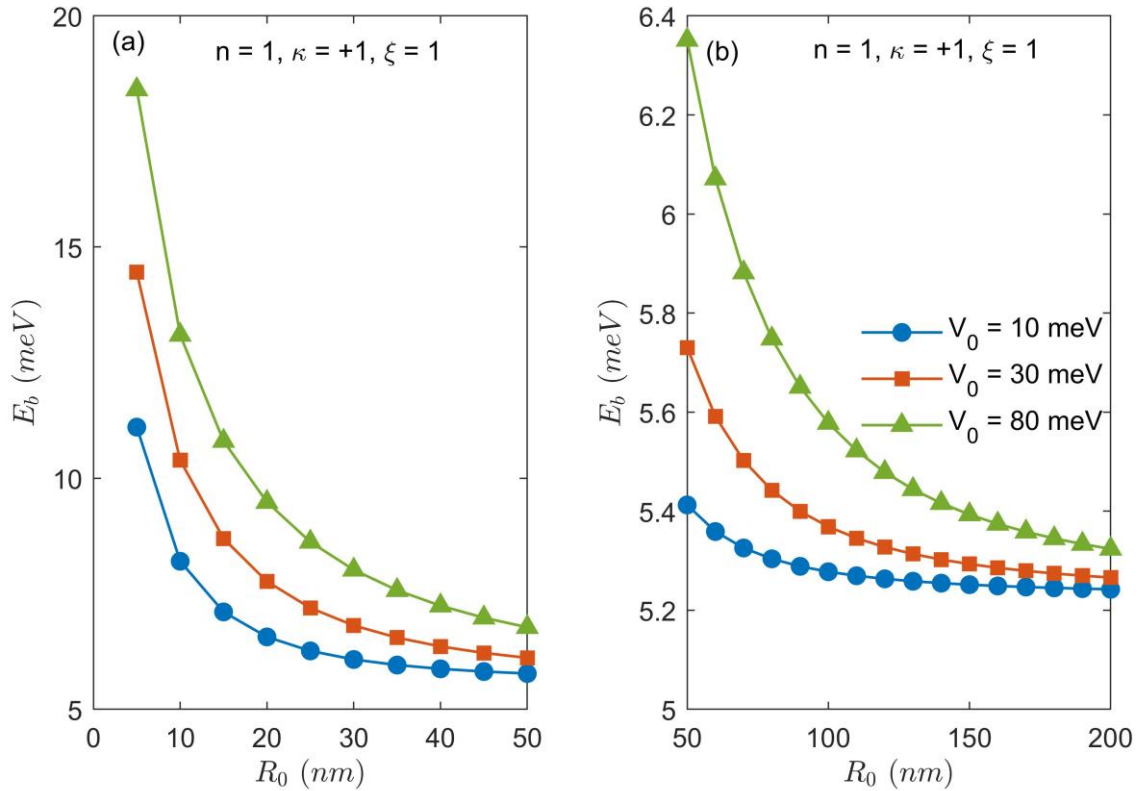


Figure 4.8: The ground state binding energy versus R_0 (a) $R_0=0-50$ nm and (b) $R_0=50-200$ nm for different confinement potential.

Moreover, to give more information about the binding energy with the confinement frequency at different potential depths, Figure 4.9 (a) achieved this aim for the ground state with the confinement frequency range of 0-300 THz for $B= 5$ T, $R_0= 15$ nm, $\kappa= +1$ and $\xi= 1$. As can be seen, the binding energy increases with rising the confinement frequency. With increasing the confinement frequency more than 300 THz all the lines tends to have the same value and show a linear growth as shown in Figure 4.9 (b).

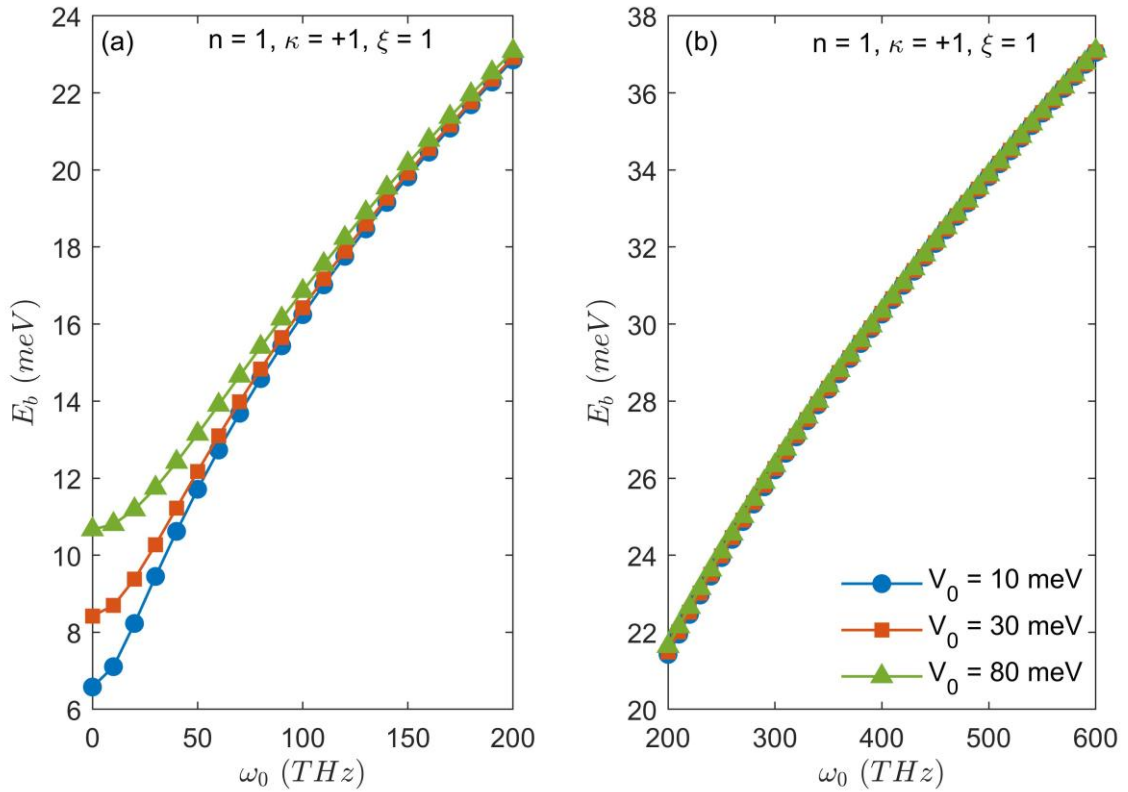


Figure 4.9: The ground state binding energy versus confinement frequency in the range of (a) 0-300 THz and (b) 300-700 THz for different potential depths.

Figure 4.10 displays the binding energies of the ground and the first excited states versus the dimensionless parameter ξ for $B= 5$ T, $\omega_0= 10$ THz, $V_0= 30$ meV, $R_0= 15$ nm and $\kappa= +1$.

It is clear that the ground state binding energy reduces with increasing the ξ parameter. The first excited state binding energy more slightly decreased with ξ parameter.

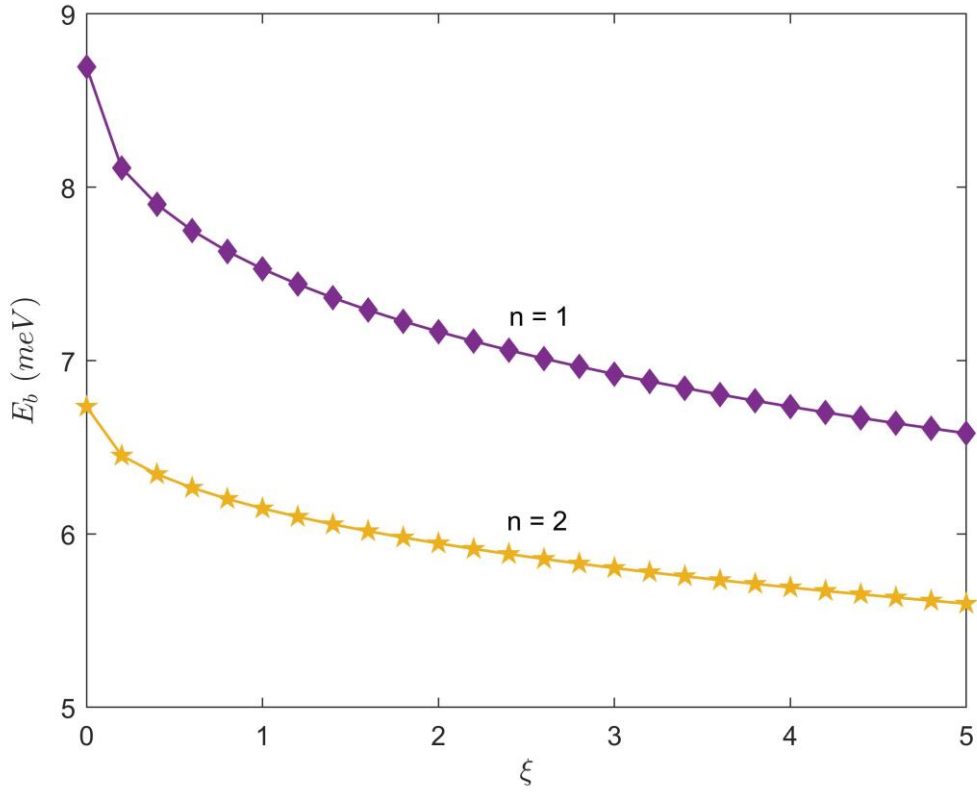


Figure 4.10: The ground state and the first excited state binding energies versus the dimensionless parameter ζ .

It is seen that the highest binding energy corresponds to $\zeta=0$ which relates to a 2D quantum disk. The repulsive potential enhances at the center of the system when ζ increases. Hence, the distance between impurity and electron rises and the binding energy reduces. Thereby, the electron is more confined. The electron confinement is changed with adjusting this ζ -parameter [71].

For different confinement frequencies, $\omega_0=100, 200, 300$ THz, the variations of the ground state binding energy have been plotted versus the dimensionless parameter ζ in Figure 4.11 with $B=5$ T, $V_0=30$ meV, $R_0=15$ nm and $\kappa=+1$. The binding energy reduces with increasing the ζ parameter. As can be seen, at a fixed value of ζ , the binding energy increases by rising the confinement frequency.

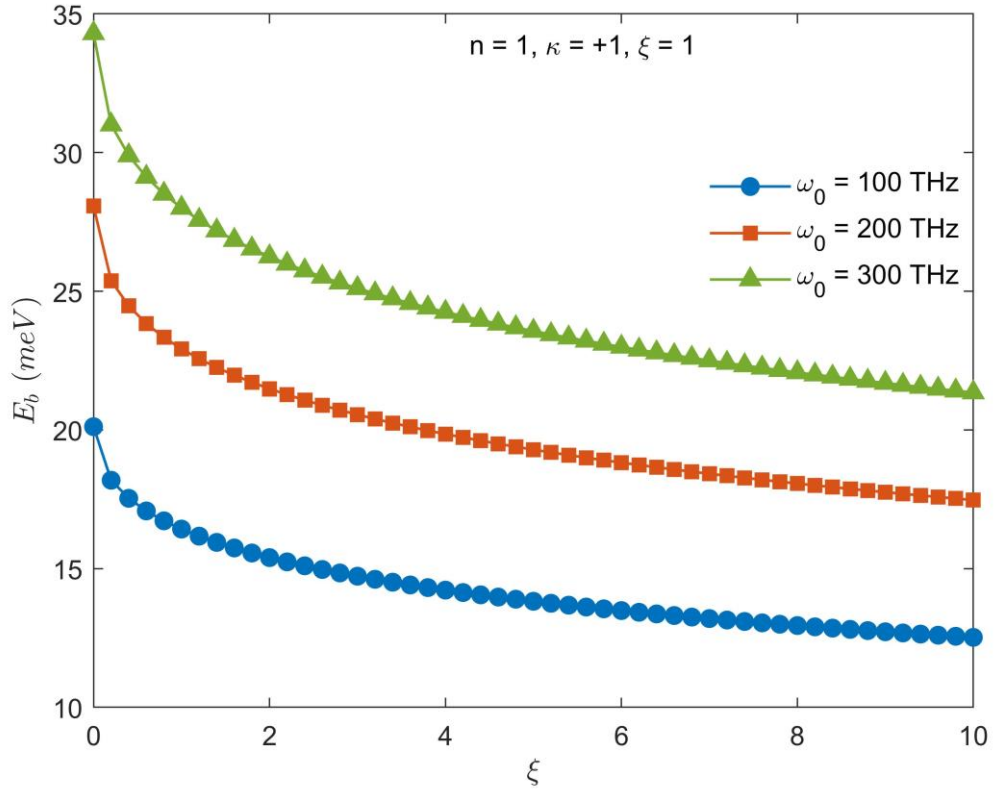


Figure 4.11: The ground state binding energy versus the dimensionless parameter ξ for different confinement frequencies.

4.1.3 The Density of States (DoS)

Figure 4.12 illustrates the DoS for a QD/QR system with and without impurity, the parameters used are $\omega_0 = 10$ THz, $V_0 = 30$ meV, $R_0 = 15$ nm and $\zeta = 1$. Each subplot shows the DoS as a function of energy (E) for quantum number n ($1 \rightarrow 5$) and specific magnetic field strengths: 1 T, 20 T, and 40 T. The energy range is 0-0.5 eV. Figure 4.12 (a) indicates how the DoS changes with energy at a low magnetic field strength ($B = 1$ T). A significant change in DoS compared to the lower magnetic field can be observed, highlighting the 20 T magnetic field's impact in Figure 4.12 (b). The Subplot (c) shows the DoS at $B = 40$ T. The energy states are expanded over wider range of energy as the magnetic field increases.

The trends and variations in DoS at this high magnetic field strength provide insights into the effects of strong magnetic fields on the electronic properties of the

QD/QR system. The splitting of the states and the quantization between the states is also clear.

As for example, low B values , ($B= 1$ T), show dense distribution of states with an energy range of 0.2 eV. Increasing the magnetic field to 20 T, shifted the states range and expanded it to 0.3 eV. Further increase in B to 40 T shifted the range more and expand it to 0.45 eV.

The DoS states around specific energy range are also splitted showing distant energy ranges between donor and acceptor impurities.

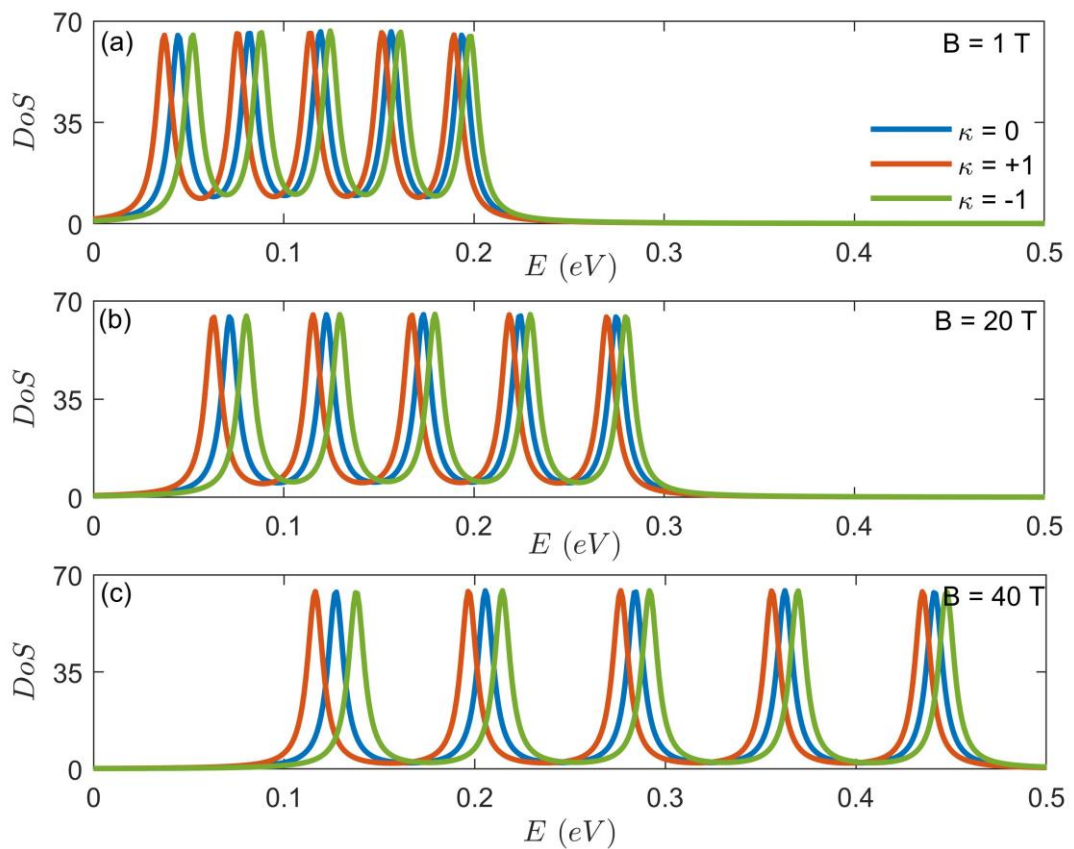


Figure 4.12: The density of state of the QD/QR system with and without impurity effect as a function of energy for n ($1 \rightarrow 5$) and specific magnetic field strengths: (a) 1 T, (b) 20 T, and (c) 40 T and $\Gamma = 0.005$.

The intensity of the peak is at the same height with and without impurity but the peak is slightly shifted toward the lower energy for $\kappa= +1$ and is shifted toward the higher energy for $\kappa= -1$.

The value of broadening factor (Γ) substituted in the DoS equation is $\Gamma = 0.005$, it controls the width and intensity of the peak. To be more clear, the above Figure of DoS

is repeated in Figure 4.13 with the same parameters except the factor $\Gamma = 0.001$. As a result of this variation, the peaks become more sharper and higher in intensity.

By increasing the magnetic field, the behavior of DoS is standard. However, as the κ -parameter changes from zero to +1 and -1, the DoS plays high-low intensity and left-right shifting. This means the structure is converted from n to p -type. Acceptor impurities cause the DoS to move toward higher energy levels by introducing additional energy levels close to the valence band. When the system becomes dominated by hole transport, more states become available for electrons at higher energies, which promotes p -type conductivity.

On the other hand, donor impurities introduce energy levels below the conduction band, donating electrons to the conduction band and increasing the number of available free electrons (negative charge carriers). This causes the DoS to shift to the left, indicating that more states are now available for electrons at lower energies. Electron transport becomes the dominant mechanism, resulting n -type conductivity.

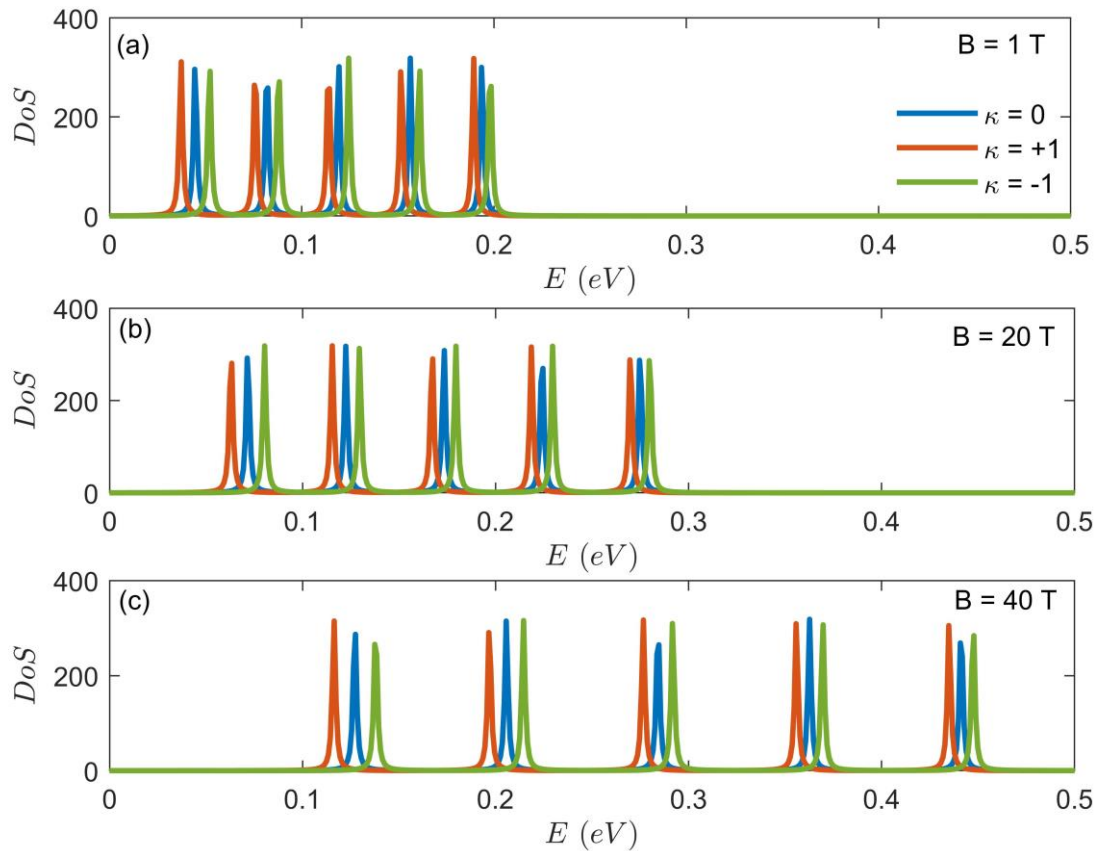


Figure 4.13: The density of state of the QD/QR system with and without impurity effect as a function of energy as a function of energy for n ($1 \rightarrow 5$) and specific magnetic field strengths: (a) 1 T, (b) 20 T, and (c) 40 T.

In literature data, the pseudo gap of GaAs is 0.46 eV [72], the intrinsic energy is 0.23 eV, which is consistent with our result (~ 0.25 eV).

The DoS for a QD/QR system with and without impurity for n ranging from 1 to 10 has been illustrated too, other parameters are the same as in Figure 4.13. The energy range is [0-0.4] eV, in order to make the plots clear and easy to explain, the figures are separated by differing B for constant n ranging with three values of κ .

At fixed value of B (see Figure 4.14), the oscillations of DoS occur at the same energy values (same energy band gap) in the absence and presence of impurity with different height.

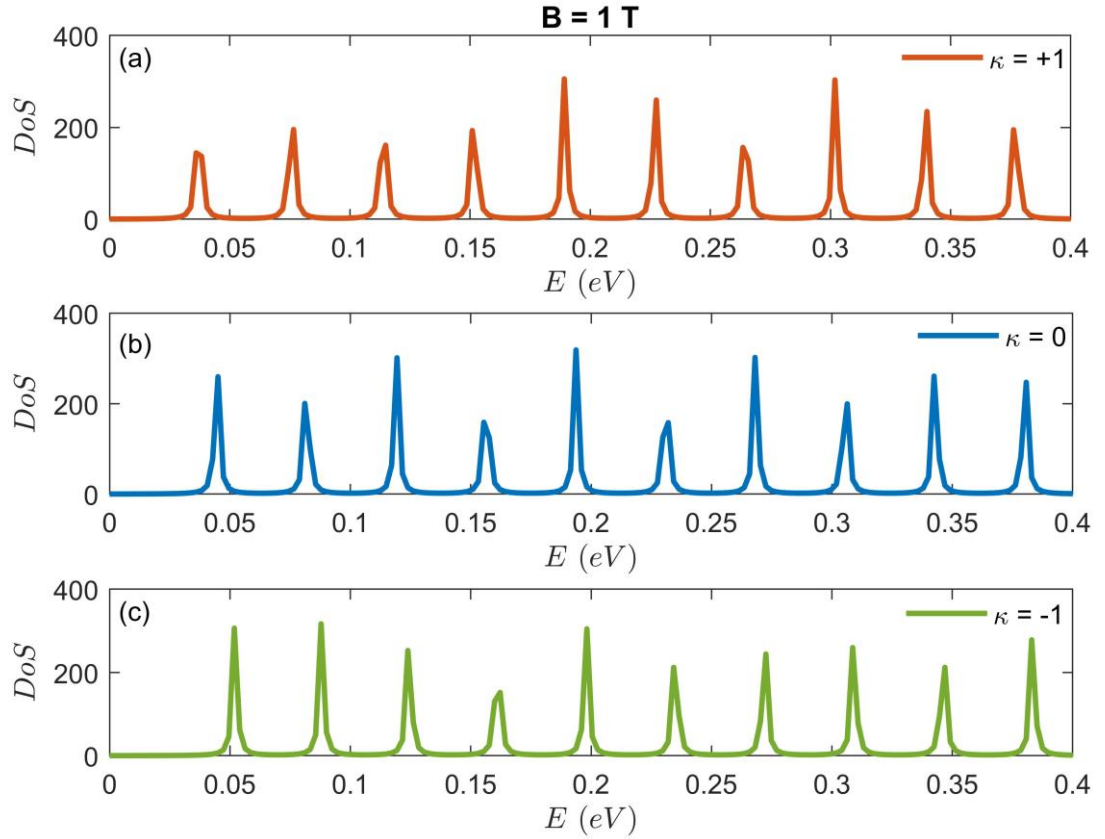


Figure 4.14: The density of state of the QD/QR system as a function of energy for n ($1 \rightarrow 10$) and specific magnetic field strength (1 T), (a) $\kappa = 0$, (b) $\kappa = +1$ and (c) $\kappa = -1$.

With magnetic field enhancement, the peaks are shifted towards the higher energy for the three values of κ . This is shown in Figures 4.15 and 4.16 that presented the DoS of the system with n ranging from 1 to 10 and $B = 20$ T and $B = 40$ T, respectively.

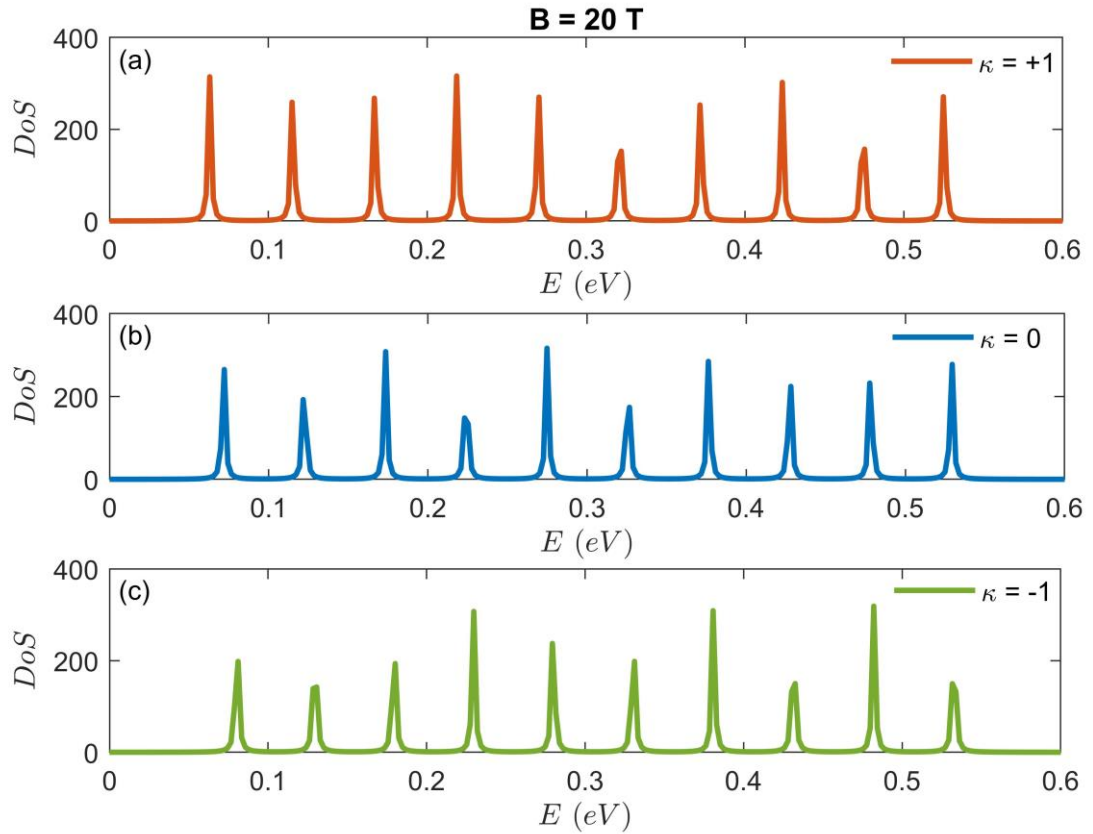


Figure 4.15: The density of state of the QD/QR system as a function of energy for n ($1 \rightarrow 10$) and specific magnetic field strength (20 T), (a) $\kappa = 0$, (b) $\kappa = +1$ and (c) $\kappa = -1$.

In addition, the increasing of B reduces the bandwidths and peaks become sharper and levels are distributed on a wide energy range (0.8 eV) in Figure 4.16, means that the magnetic field controls the band gap, the dominant band gap is not 0.46 eV. By increasing the magnetic field, the DoS extended to higher energy range, the magnetic field enhances the quantum confinement, leading to an increase in the energy gap.

It is noted that in the case of n ($1 \rightarrow 10$) as the strength of the magnetic field increases, the bandwidth of the oscillations decreases, unlike what was seen in the case of n ($1 \rightarrow 5$). This is explained as follows; Increasing the magnetic field induces a quantization of the energy levels (Landau levels) and enhances the confinement of the charge carriers, At lower quantum numbers, the energy spacing between levels increases due to this strong confinement effect resulting an increase in the bandwidth of the DoS.

However, at higher quantum numbers, the energy levels may start to compress or saturate as the magnetic field increases further, because the effects of magnetic

quantization are reduced for these higher energy states. This decreases the energy separation between states, resulting a decrease in the bandwidth of the DoS. The bandwidth basically contracts as a result of the high-lying energy states becoming less sensitive to an increase in magnetic field.

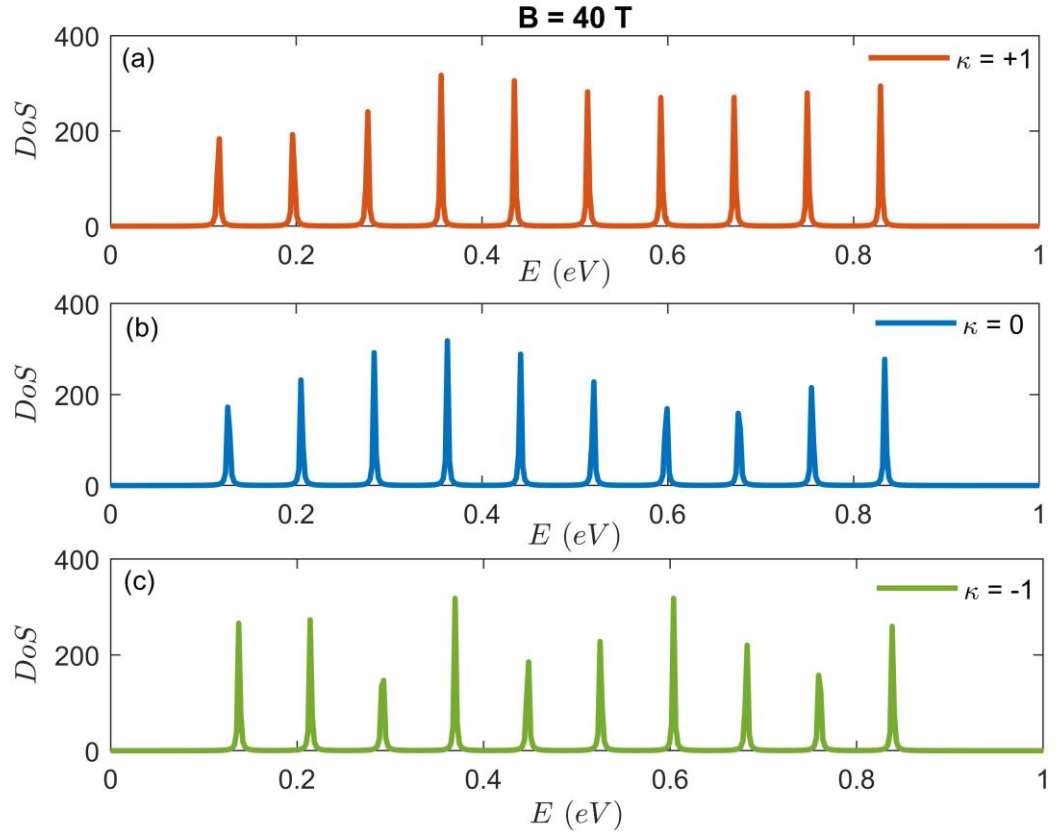


Figure 4.16: The density of state of the QD/QR system as a function of energy for n ($1 \rightarrow 10$) and specific magnetic field strength (40 T), (a) $\kappa = 0$, (b) $\kappa = +1$ and (c) $\kappa = -1$.

It is worth mentioning that the energy band gaps of GaAs exhibit the value [72],

Energy gap	1.42 eV
Energy separation ($E_{\Gamma L}$) between Γ and L valleys	0.29 eV
Energy separation ($E_{\Gamma X}$) between Γ and X valleys	0.46 eV

Again, changing n -range and altering the magnetic field values display interesting results for the DoS of QD/QR system with and without impurity. The last three figures which are shown above are repeated with new range of n ($1 \rightarrow 20$). See Figures 4.17, 4.18, 4.19.

In figures 4.17-19, the effect of magnetic field is observed in shifting the peaks toward the higher energy.

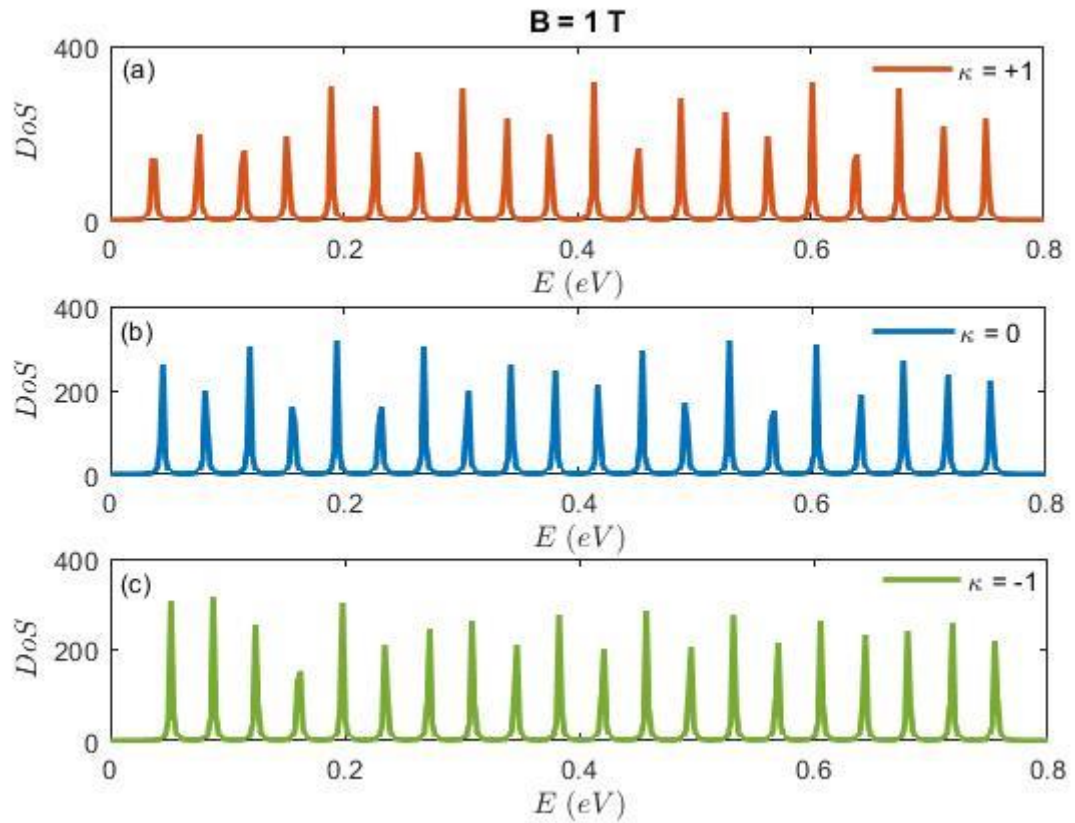


Figure 4.17: The density of state of the QD/QR system ν as a function of energy for n ($1 \rightarrow 20$) and specific magnetic field strength (1 T), (a) $\kappa = 0$, (b) $\kappa = +1$ and (c) $\kappa = -1$.

It is clear that the height of peaks differs with κ -parameter variation; the energy gap here is about 1.4 eV which is equivalent to literature data of GaAs band gap.

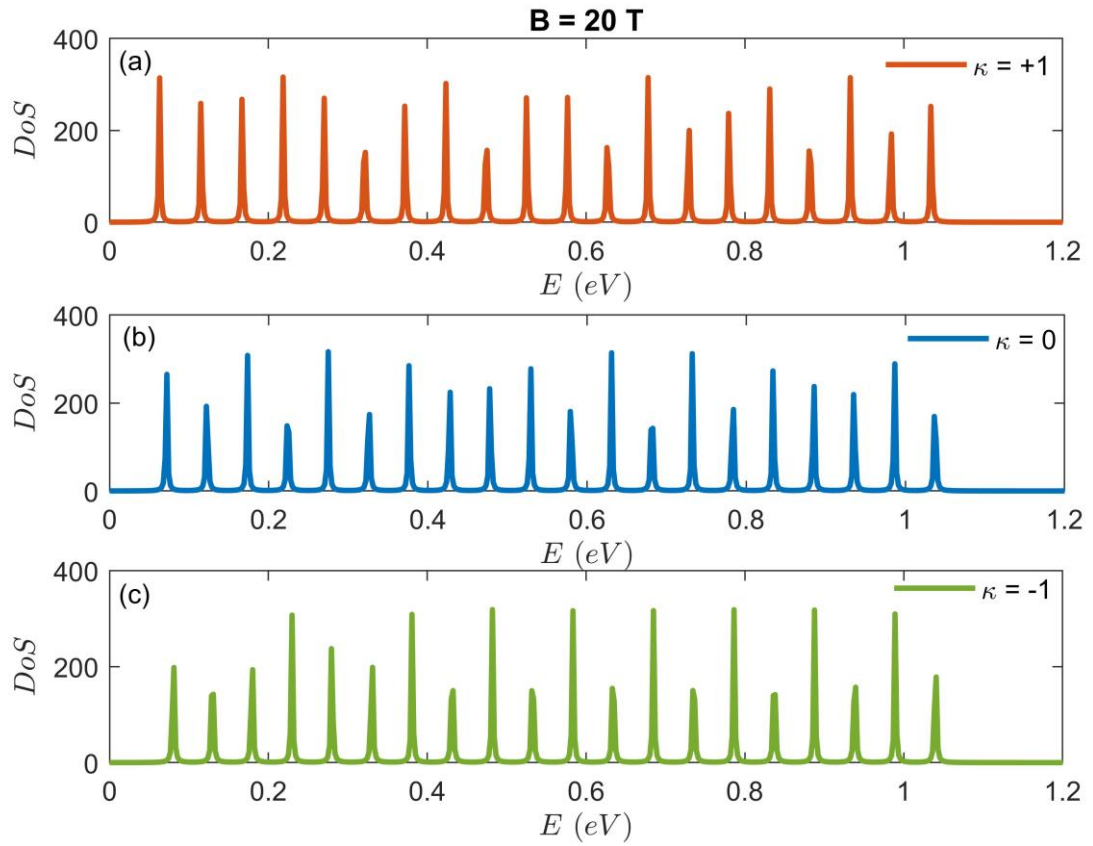


Figure 4.18: The density of state of the QD/QR system as a function of energy as a function of energy for n ($1 \rightarrow 20$) and specific magnetic field strength (20 T), (a) $\kappa = 0$, (b) $\kappa = +1$ and (c) $\kappa = -1$.

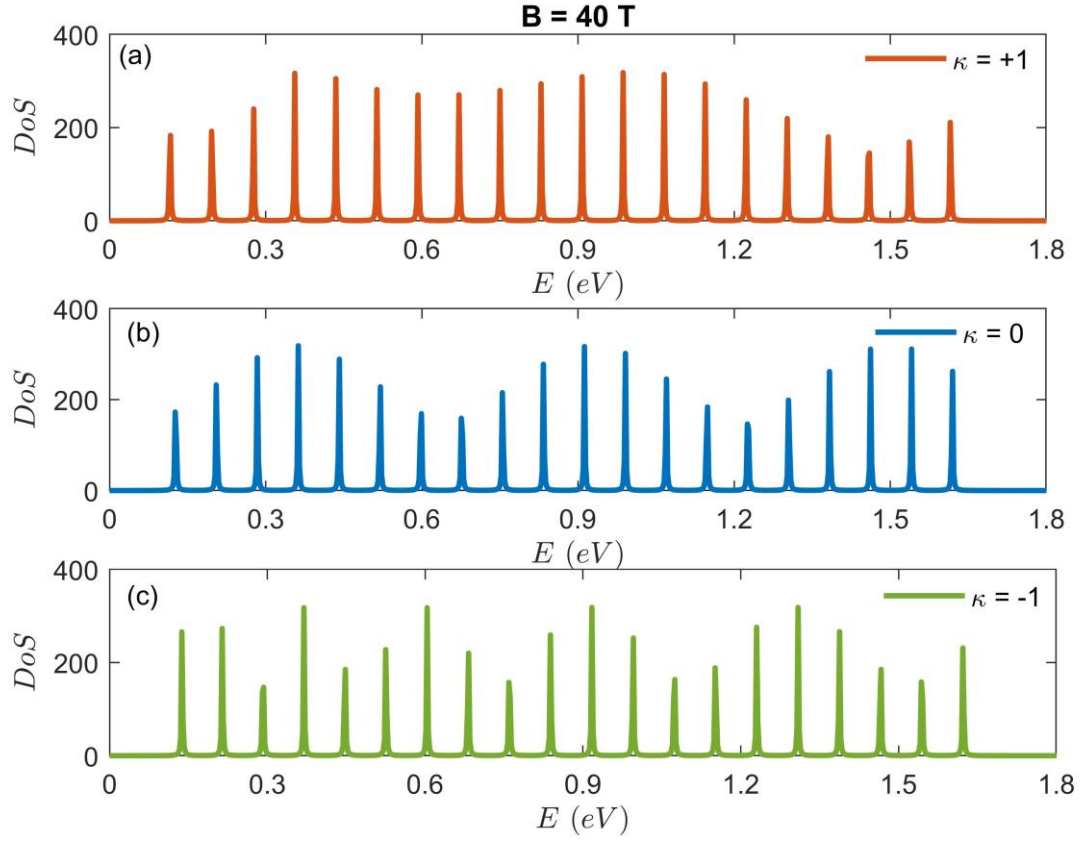


Figure 4.19: The density of state of the QD/QR system as a function of energy for n ($1 \rightarrow 20$) and specific magnetic field strength (40 T), (a) $\kappa = 0$, (b) $\kappa = +1$ and (c) $\kappa = -1$.

In short, the DoS varies with energy, showing distinct peaks and features that correspond to specific electronic states influenced by the QD/QR confinement, magnetic fields and impurities. The interaction between a changing magnetic field, impurity type and quantum number n significantly affects the DoS and the electronic properties of n -type and p -type materials. Magnetic fields can induce shifts of energy levels, impurities introduce localized states that interact with the host material's band structure, and quantum number define the energy levels that magnetic fields modulate. Understanding these effects is crucial for designing materials with tailored electronic properties for applications in magnetic sensors, spintronics, and quantum computing.

4.2 Thermal Properties

4.2.1 Convergence Test and Statistical Average Energy

Firstly, the statistical energy is computed as an important quantity because it allows all the thermodynamic quantities to be derived. An important step in this work is to ensure the accuracy and convergence of the computed numerical statistical energy of the QD/QR system, the number of basis is increased until the convergent energy values are obtained. The statistical energy given in equation (3.37) and calculated by taking quite large number of basis: n ($1 \rightarrow 20$) and plotted as function of number of basis for different set of temperatures in Figure 4.20 and Figure 4.21 for the absence and presence of impurity, respectively. The substituted parameters are $B= 5$ T, $\omega_0= 10$ THz, $V_0= 30$ meV, $R_0= 15$ nm and $\zeta= 1$. For temperature value ($T= 300$ K), the convergency is obtained at a small number of basis ($\sim \#7$), however, a number of basis ($\sim \#4$) for temperature $T= 200$ K and ($\sim \#2$) for temperature $T= 100$ K achieved the convergency of the energy.

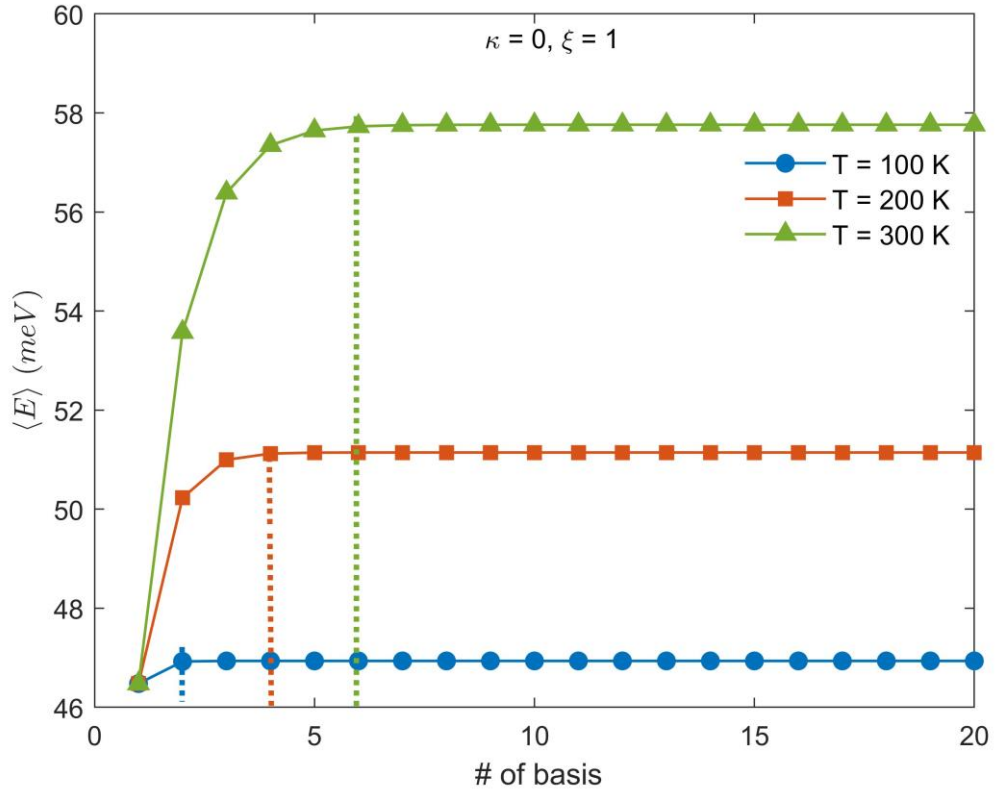


Figure 4.20: Statistical average energy versus number of basis calculated at different values of temperature for QD/QR system for $\kappa= 0$.

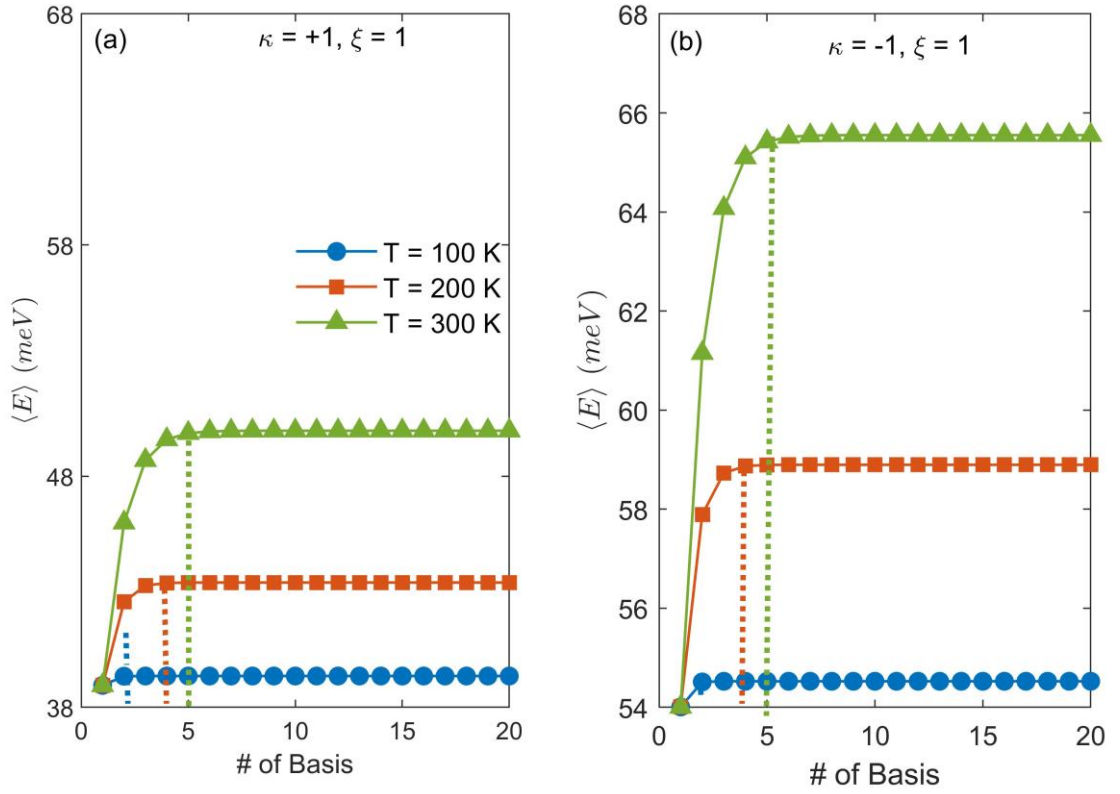


Figure 4.21: Statistical average energy versus number of basis calculated at different values of temperature for QD/QR system with (a) $\kappa = +1$ and (b) $\kappa = -1$.

To investigate the effects of impurity and external parameters such as temperature, magnetic field and confinement potential on the thermal properties of the system, the Statistical average energy is plotted against the temperature with $B = 5$ T, $\omega_0 = 10$ THz, $V_0 = 30$ meV and $R_0 = 15$ nm, considering the QD case ($\zeta = 0$) and QD/QR ($\zeta = 1$) for various values of the κ -parameter in Figure 4.22 (a) and (b). The mean energy of the system is appeared to be constant with temperature from 0 to about 100 K in $\zeta = 0$ case, Above this value, the mean energy rises with enhancement of temperature with and without the impurity.

Comparison with the $\kappa = 0$ case, the mean energy is increasing in the presence of acceptor impurity and decreasing with donor impurity, but the impurity effect on shallow states is less dominant. Above the temperature of 400 K, the energy increases slowly compared with the range of temperature less than this value. In addition, changing ζ from 0 to 1 makes the average statistical energy constant from 0 to 60 K and then increasing with temperature. The values of $\langle E \rangle$ is higher for the case of $\zeta = 1$.

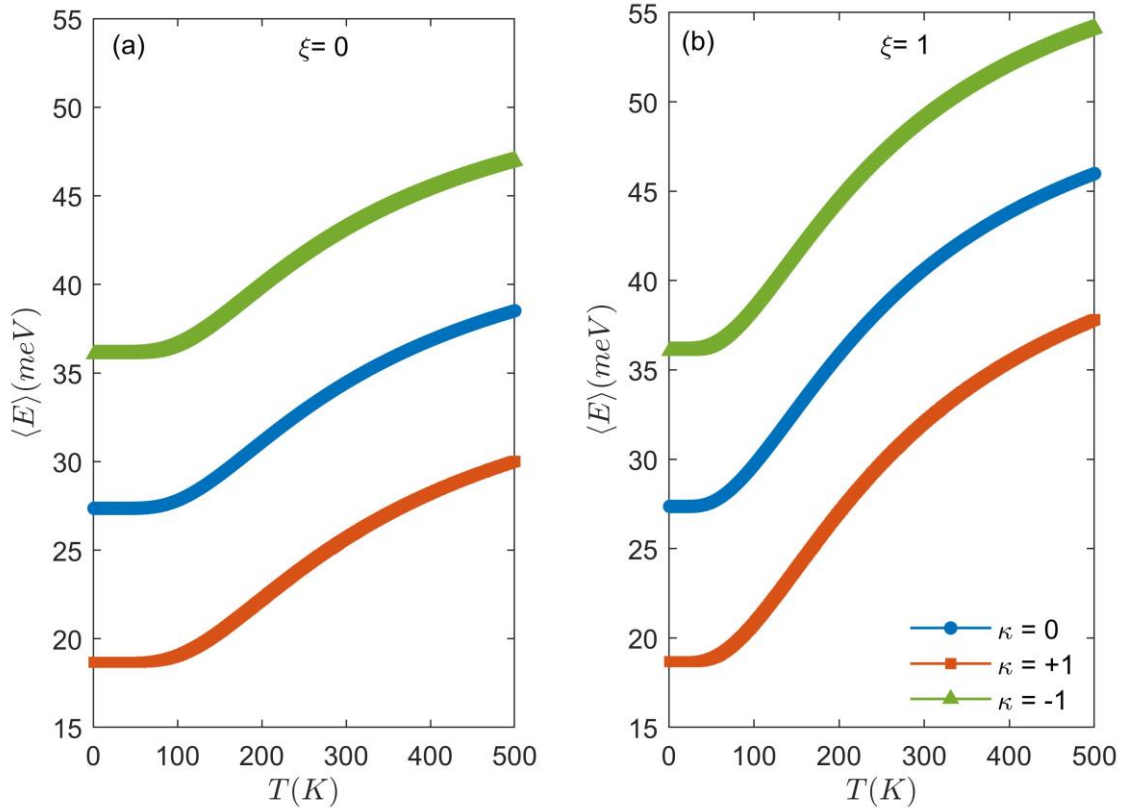


Figure 4.22: Mean energy versus temperature with and without the impurity effect for (a) $\xi = 0$ and (b) $\xi = 1$.

Figure 4.23 shows the variation of mean energy with temperature for different magnetic field values (1 T, 10 T, 20 T). in the presence of donor impurity leaving other parameters fixed ($\omega_0 = 10$ THz, $V_0 = 30$ meV, $R_0 = 15$ nm, $\kappa = +1$ and $\xi = 1$). As the temperature increases above 60 K, the average energy of the electron increases while the magnetic field is constant due to the increase in the kinetic energy and energy level range of the electron [34]. By increasing the magnetic field from 1 T to 20 T. the mean energy increases for all temperature range.

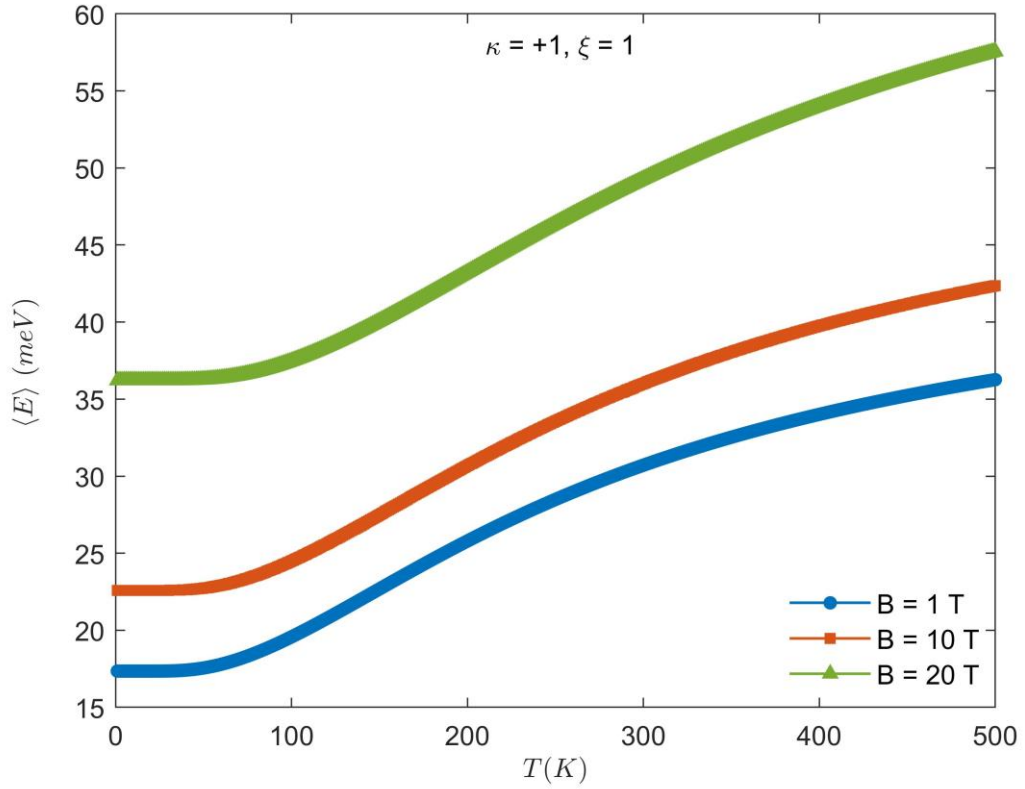


Figure 4.23: Mean energy versus temperature for donor impurity case at different magnetic field values.

The effect of magnetic field on the statistical energy is shown in Figure 4.24 with and without impurity for $\zeta = 0$ and $\zeta = 1$ leaving other parameters constant ($T = 100$ K, $\omega_0 = 10$ THz, $V_0 = 30$ meV and $R_0 = 15$ nm). Figure 4.24 shows that the mean energy starts to increase by increasing magnetic field values. When the magnetic field strength gets higher, the statistical energy gets higher too at constant temperature, that is due to the additional confinement of the electron by the magnetic field [68]. For each case of impurity, the statistical energy does not change when ζ changes from 0 to 1.

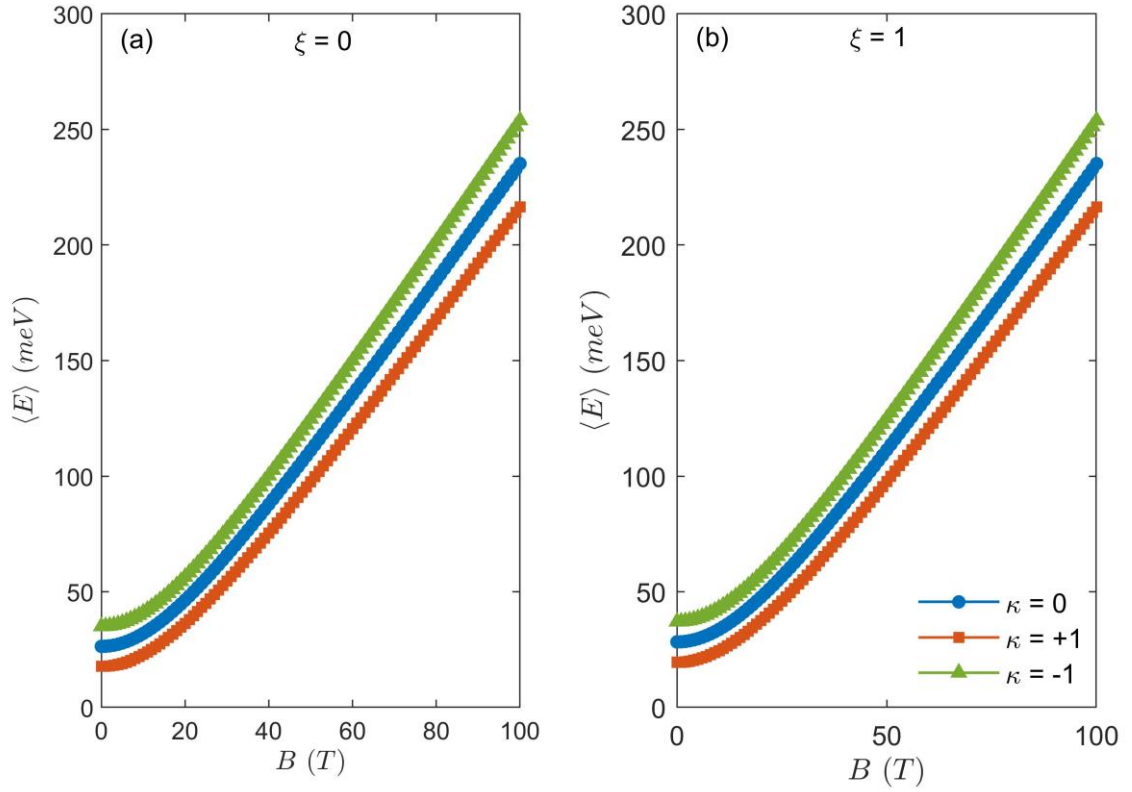


Figure 4.24: Mean energy versus magnetic field with and without the impurity effect for (a) $\xi=0$ and (b) $\xi=1$.

Moreover, the effect of magnetic field on statistical energy is studied especially for donor impurity with different values of temperature (100K, 200K, 300K) keeping other parameters constant ($\omega_0=10$ THz, $V_0=30$ meV, $R_0=15$ nm, $\kappa=+1$ and $\xi=1$). One can see from Figure 4.25 that for higher temperature, the statistical energy is higher in the range of 0-80 T, that is consistent with literature data [73]. Above this range, the average energy is not affected by changing the temperature.

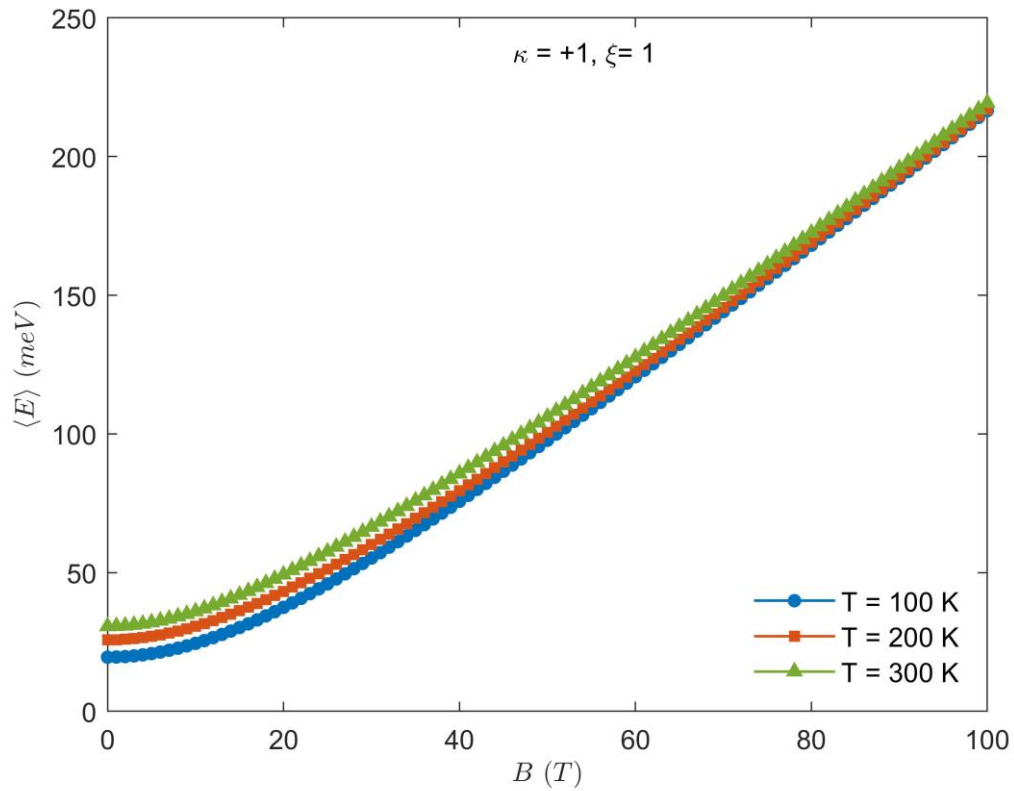


Figure 4.25: Mean energy versus magnetic field for donor impurity case at different temperature values.

In order to study the effect of confinement parameters on the average energy of the system, the average energy was plotted with temperature at three confinement potential values: 10, 30, and 80 meV in the presence of donor impurity with $B= 5$ T, $\omega_0= 10$ THz, $R_0= 15$ nm, $\kappa= +1$ and $\xi= 1$ in Figure 4.26. It appears that by increasing the confinement potential (V_0), the energy decreases at fixed temperature. This is because more energy levels result from higher confinement potentials, which in turn reduce the thermal population of higher energy states and, as a result, lower the system's average energy at a given temperature.

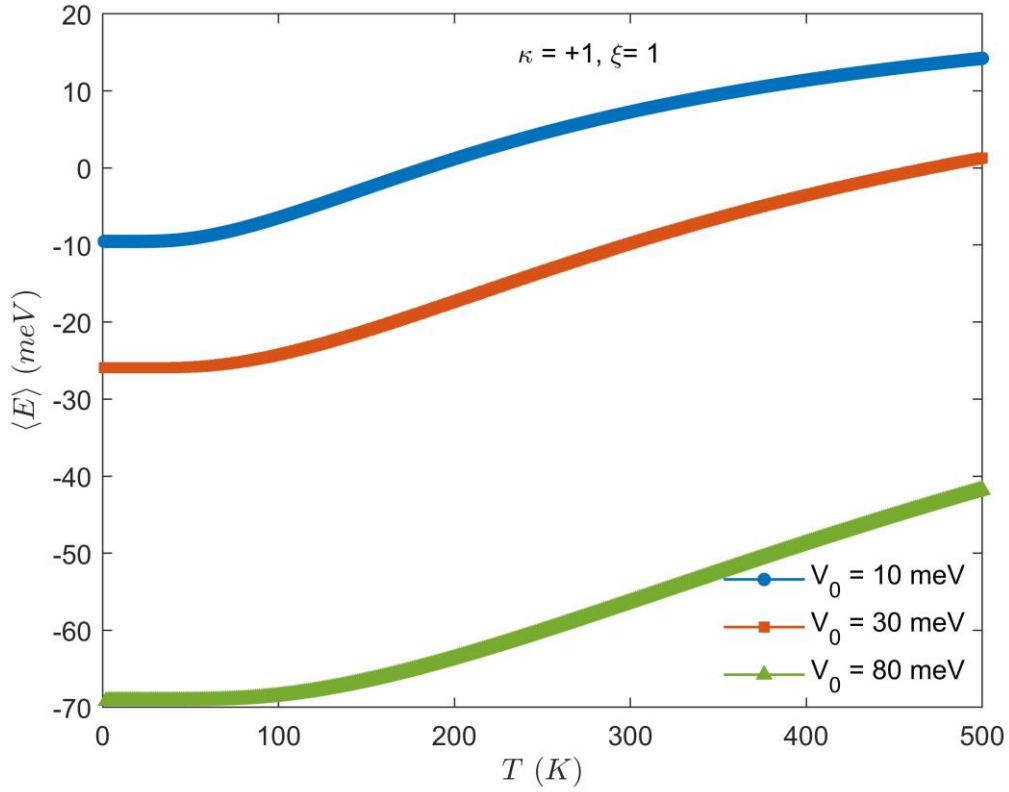


Figure 4.26: Mean energy versus temperature for donor impurity case at different confinement potential values.

Because the energy levels are discrete, the behavior of the QD average energy depends on the density of states. Thus, the temperature of the occupation probability of the states and the energy level distribution will determine the thermodynamic properties.

4.2.2 Helmholtz Free Energy (F)

The presence of free energy provides important insights on how likely the system transforms from one state to another spontaneously. The temperature dependence of the Helmholtz free energy is displayed in Figure 4.27 with and without the impurity effect for $B=5$ T, $\omega_0=10$ THz, $V_0=30$ meV and $R_0=15$ nm, considering the QD case ($\zeta=0$) and QD/QR ($\zeta=1$), it has a constant value then decreases monotonically as the temperature increases.

The decreasing trend of free energy is common and it becomes more negative during the course of any natural process. The decline in free energy is determined by the entropy (S) of the system, where the slope of this curve is a negative entropy. As

temperature rises, entropy becomes significant, and the free energy declines. The decrease in F-T curves reflects the balance between internal energy and entropy, governing phase transitions, chemical reactions, and stability [74]. Note that the plots behave the same for all impurity cases.

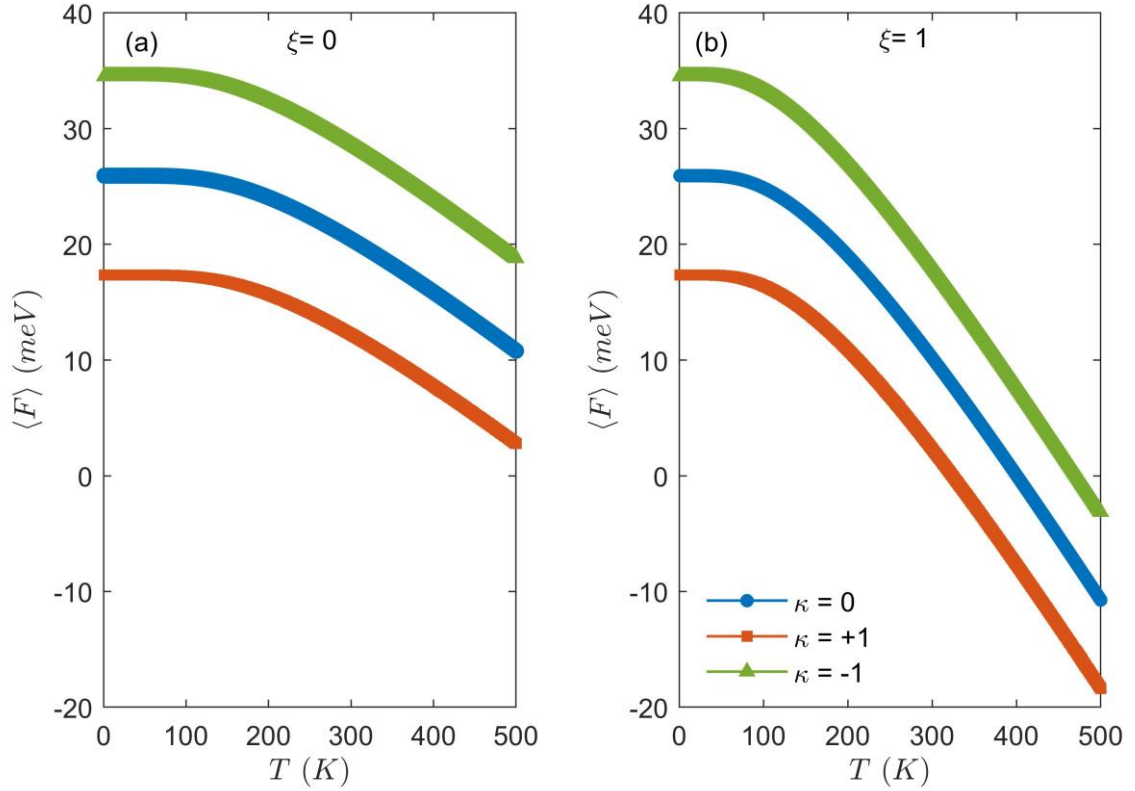


Figure 4.27: Free energy versus temperature with and without the impurity effect for (a) $\xi = 0$ and (b) $\xi = 1$.

Figure 4.28 shows the variation of Helmholtz free energy with temperature for different B values with $\omega_0 = 10$ THz, $V_0 = 30$ meV, $R_0 = 15$ nm, $\kappa = +1$ and $\xi = 1$. It is clear that the free energy reduces as temperature increase at constant magnetic field and increases by increasing the magnetic field at fixed temperature. As the temperature increases, the confinement energy and thermal energy determine the degree of change in the Helmholtz free energy of the QD.

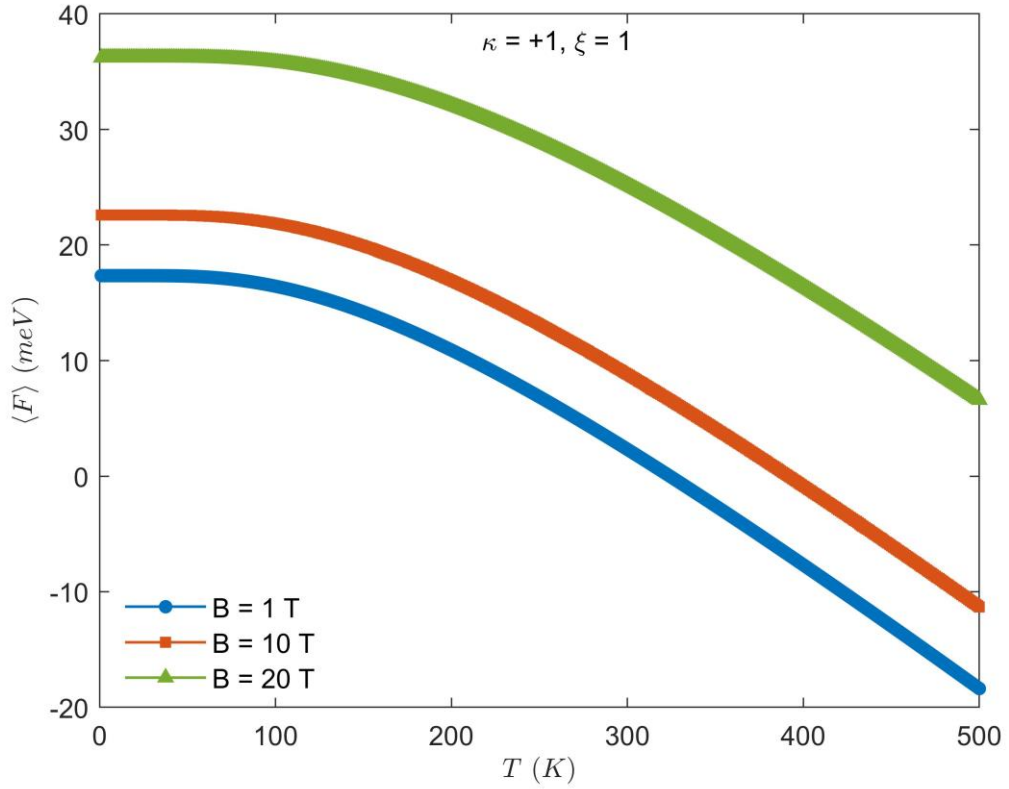


Figure 4.28: Free energy versus temperature for donor impurity case at different magnetic field values.

The influence of magnetic field and the impurity on the Helmholtz free energy of the system at a certain temperature (100 K) with $\omega_0 = 10$ THz, $V_0 = 30$ meV and $R_0 = 15$ nm, is examined in the Figure 4.29. In (a), the free energy exhibits the same behavior with and without impurity and it increases with enhancing magnetic field. The lines are the same when ξ -parameter increases to 1 as in (b).

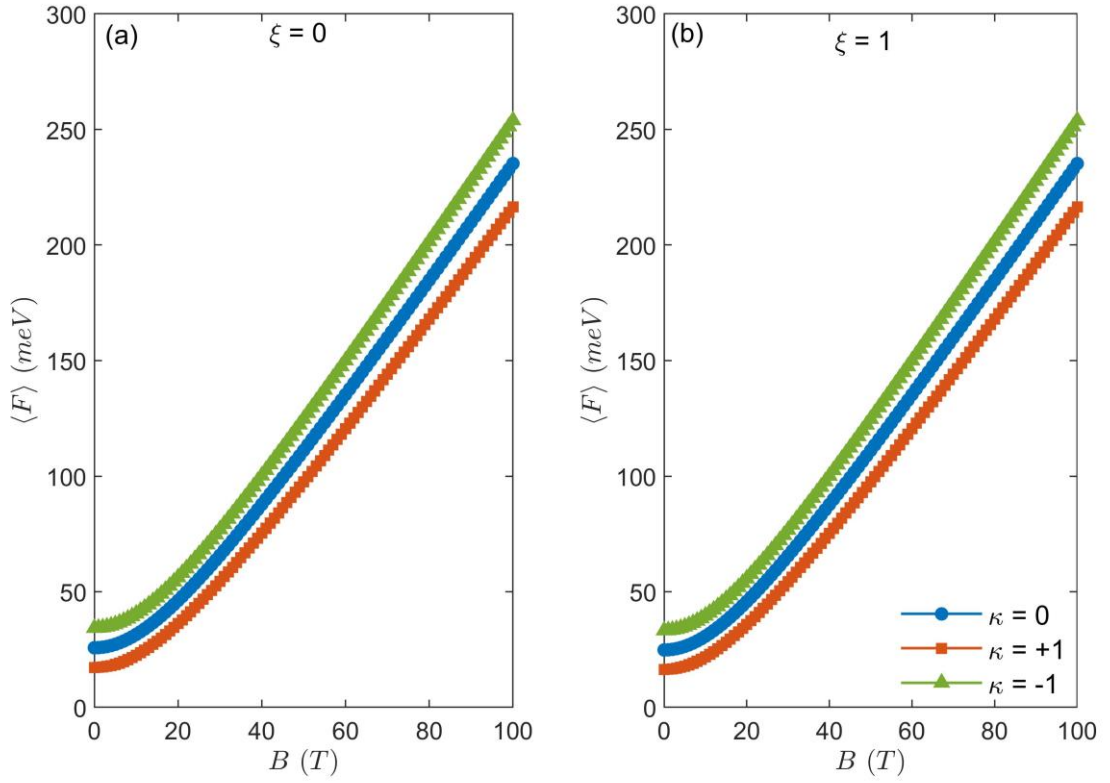


Figure 4.29: Free energy versus magnetic field with and without the impurity effect for (a) $\xi=0$ and (b) $\xi=1$.

The variation of free energy with magnetic field for three different values of temperatures are presented in Figure 4.30 in the presence of donor impurity with $\omega_0=10$ THz, $V_0=30$ meV, $R_0=15$ nm, $\kappa=+1$ and $\zeta=1$. The free energy is increasing with magnetic field and is decreasing as temperature increasing at fixed magnetic field. This behavior is dominant until $B=50$ T. Above this value, no effect of temperature appeared. At constant temperature, the increase in the magnetic field leads to an increase in the Helmholtz free energy due to the magnetic contribution to the system's internal energy, with little or no contribution from the entropic term. The temperature's effect on entropy and internal energy becomes negligible when the thermal energy is much smaller than the energy scale associated with magnetic field, So the magnetic field controls the free energy behaviour.

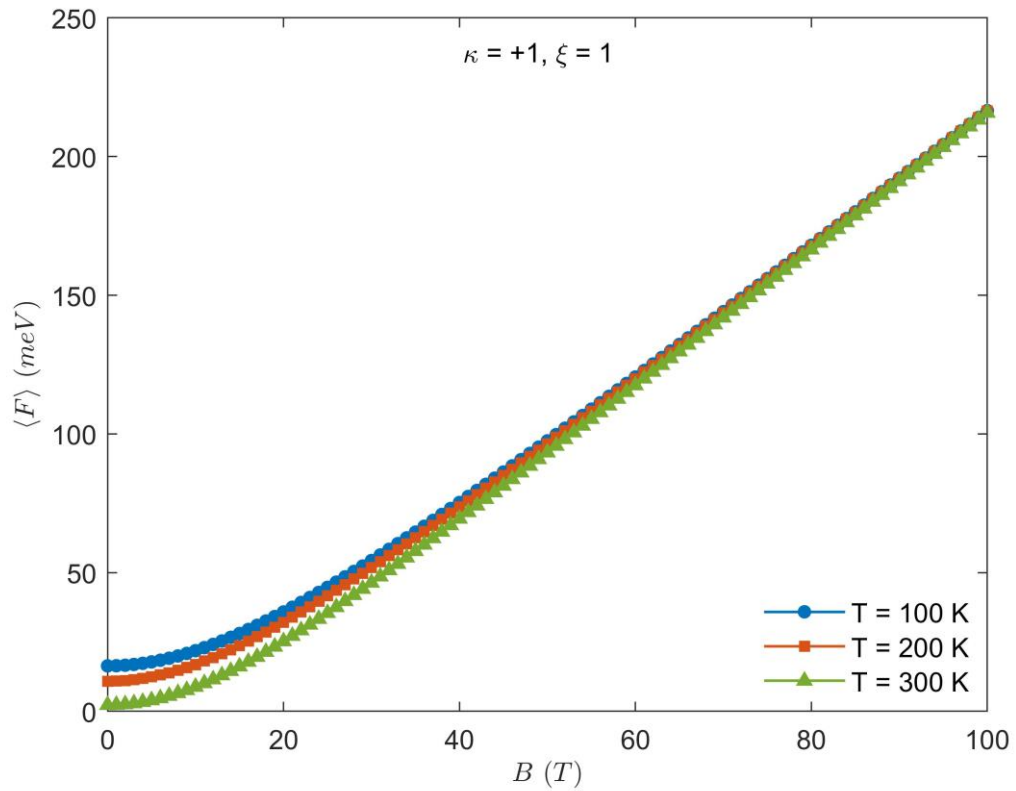


Figure 4.30: Free energy versus magnetic field for donor impurity case at different temperature values.

The effect of confinement potential on the Helmholtz free energy is presented in Figure 4.31 with three different values of potential and the parameters $B= 5\text{T}$, $\omega_0= 10$ THz, $R_0= 15$ nm, $\kappa= +1$ and $\zeta= 1$, the free energy is reduced by increasing the potential value at a given temperature. This behavior matches the behavior of average energy by varying the potential.

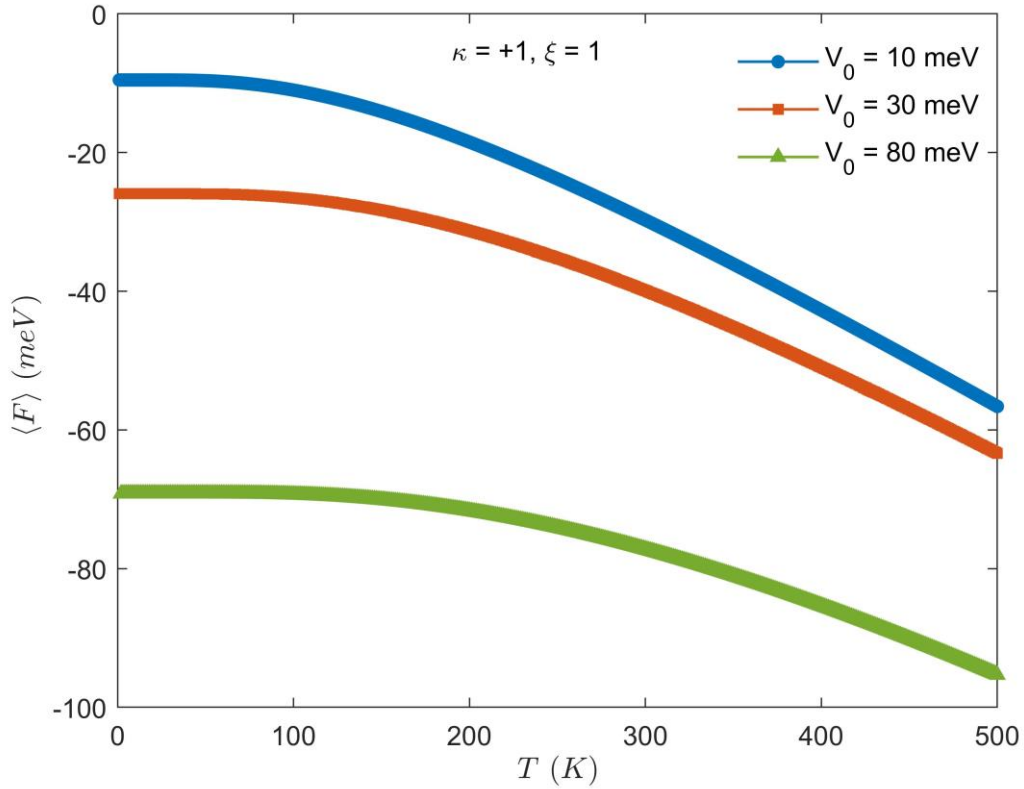


Figure 4.31: Free energy versus temperature for donor impurity case at different confinement potential values.

4.2.3 Specific Heat (C_v)

Figure 4.32 demonstrates the specific heat of the system as a function of temperature with and without the impurity term for $B= 5$ T, $\omega_0= 10$ THz, $V_0= 30$ meV and $R_0= 15$ nm, considering the QD case ($\zeta= 0$) and QD/QR ($\zeta= 1$). It could be seen that the specific heat has a sharp increase as temperature increases with and without the impurity effect. Then, the specific heat has a peak occurs at approximately 180 K that is very slightly raised and shifted toward the right when $\kappa= +1$ and it is declined and shifted toward left when $\kappa= -1$ in the case of quantum disk in Figure 4.32 (a). Moreover, the peak appears at around 150 K when $\zeta= 1$ with greater values of specific heat.

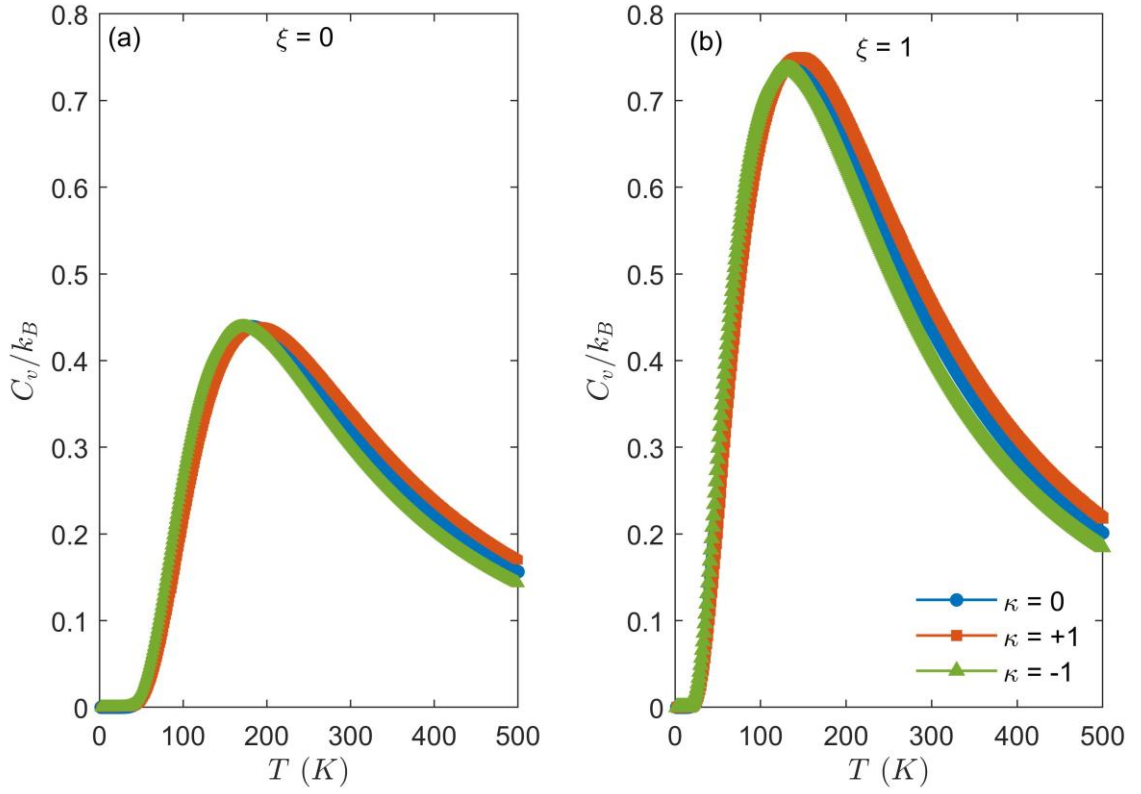


Figure 4.32: Specific heat versus temperature with and without the impurity effect for (a) $\xi = 0$ and (b) $\xi = 1$.

The specific heat usually remains constant, or increases with temperature. It occurs in systems with a restricted number of energy levels. Because the specific heat is given from the equation 3.39, it will show a peak as the temperature crosses over from one step to the next.

This observed peak is demonstrated because the energy spacing is increased when the system is under an external magnetic field. Therefore, the transition probability is small at low temperatures since the system has not sufficient energy to go to higher levels. As the temperature increases, the system gains more thermal energy, and the transition probability rises. The specific heat shows a peak structure when the thermal energy and the transition energy between the levels are equal [66].

Figure 4.33 depicts the behavior of the specific heat of a GaAs QD/QR with donor impurity as a function of the temperature for different magnetic field values: 1 T, 10 T and 20 T with $\omega_0 = 10$ THz, $V_0 = 30$ meV, $R_0 = 15$ nm, $\kappa = +1$ and $\xi = 1$. The behavior of

specific heat as discussed above is increasing with enhancing the temperature until a peak structure (resonance) is reached and after that, it decreases.

On the other hand, it is observed that the peak of the specific heat shifts towards higher temperature values and show wider band width with same intensity as magnetic fields gets stronger.

The increasing of heat capacity is due to the increase in thermal energy of electrons as the temperature increased which makes large number of states available for thermal excitations. In addition, the resonance in specific heat is regarded as the well-known Schottky anomaly [75], which is observed in magnetic systems and is closely related to the energy required for a thermal transition between the ground state and the first excited state of the system. These properties would find experimental realization in the so-called quantum dots photodetectors [76] and photodiodes [75].

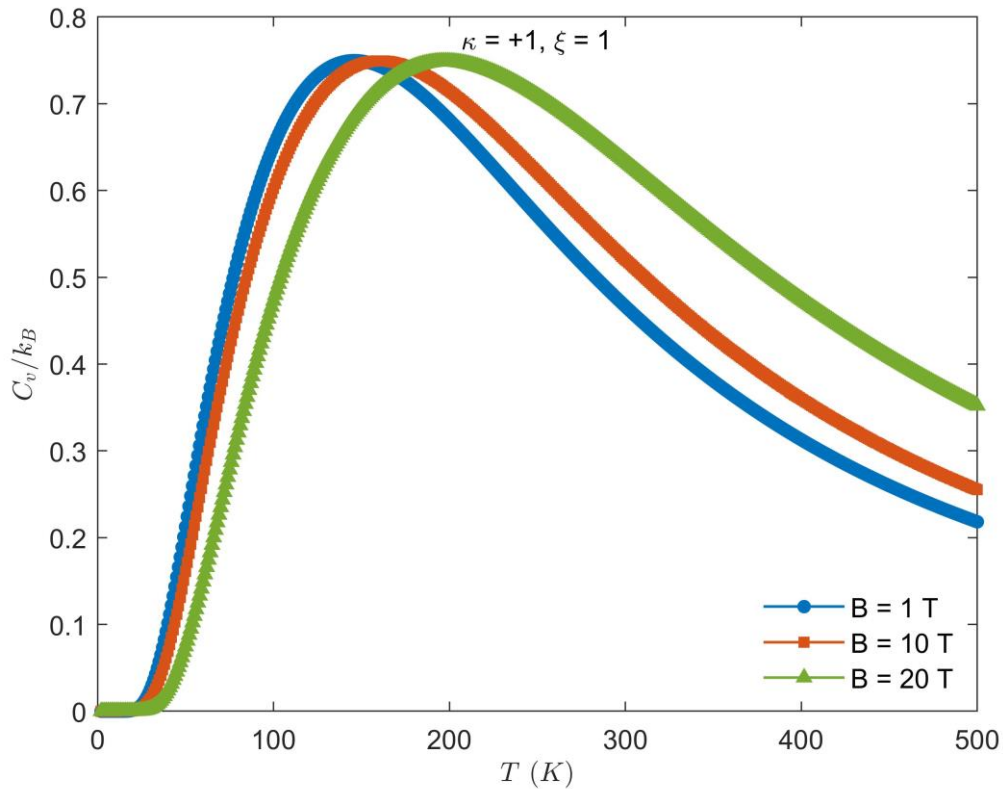


Figure 4.33: Specific heat versus temperature for donor impurity case at different magnetic field values.

The dependence of specific heat on magnetic field at constant temperature (100 K) is illustrated in Figure 4.34 for QD/QR system with $\omega_0 = 10$ THz, $V_0 = 30$ meV, and $R_0 =$

15 nm, It is seen from Figure 4.34 (a) that the specific heat decreases with enhancing the magnetic field until 50 T. Above 50 T, C_v reaches zero and remains zero to the end of the B -range and the impurity is not affected. The specific heat increases with enhancing ζ parameter to one for fixed case of impurity. The impurity effect on specific heat is clearly seen at about 20 T where C_v plays a peak before it continues with the same behavior of the first case in Figure 4.34 (a).

The quantum dot system is expected to behave as a free 2D system at low magnetic fields and high temperatures, because of the excess thermal energy available for the electron as a kinetic energy. The 2D-QD/QR system has heat capacity limit ($1 k_B$), with $k_B/2$, for each degree of freedom.

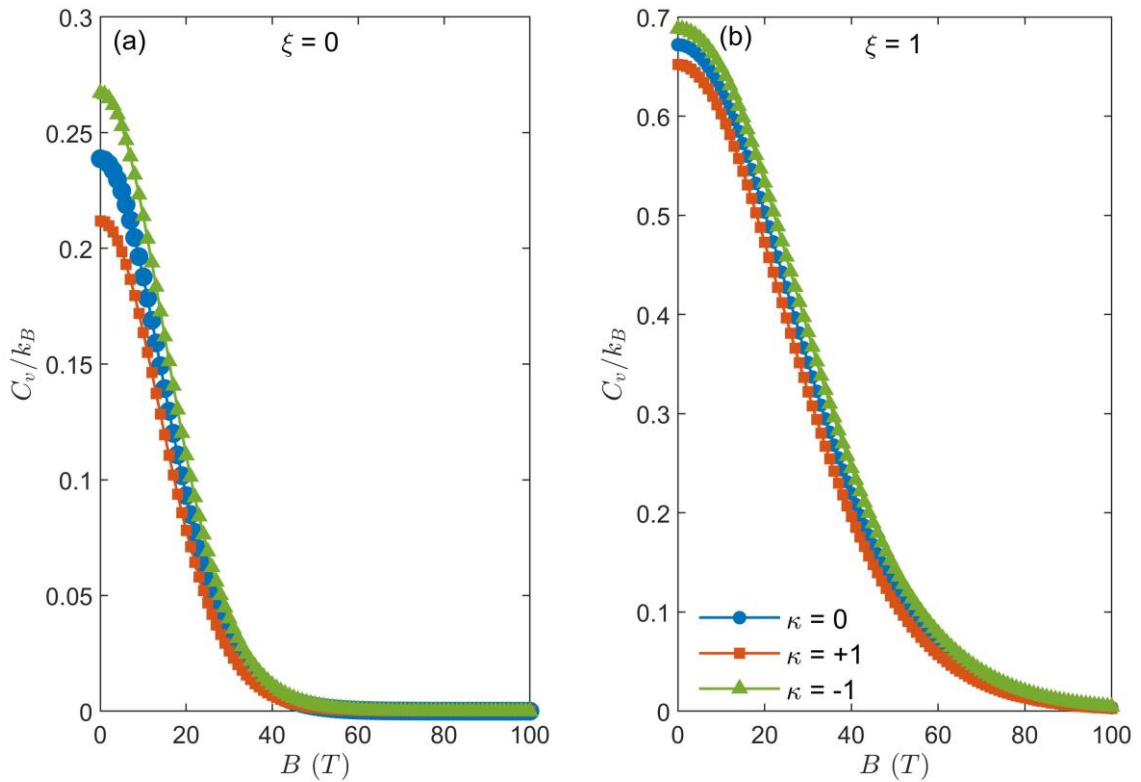


Figure 4.34: Specific heat versus magnetic field with and without the impurity effect for (a) $\zeta=0$ and (b) $\zeta=1$.

The effect of magnetic field on the specific heat of QD/QR system with donor impurity is studied for different three values of temperature with $\omega_0=10$ THz, $V_0=30$ meV, $R_0=15$ nm, $\kappa=+1$ and $\zeta=1$; At $T=100$ K, the specific heat begins with a peak at 7 K and then decreases from maximum until it reaches zero value. For $T=200$ K, the

starting peak occurs at about 30 K then it lowers. At $T= 300$ K, the C_v - B curve has the same behavior of $T= 200$ K with the peak shifted at 40 K. As seen clearly in Figure 4.35.

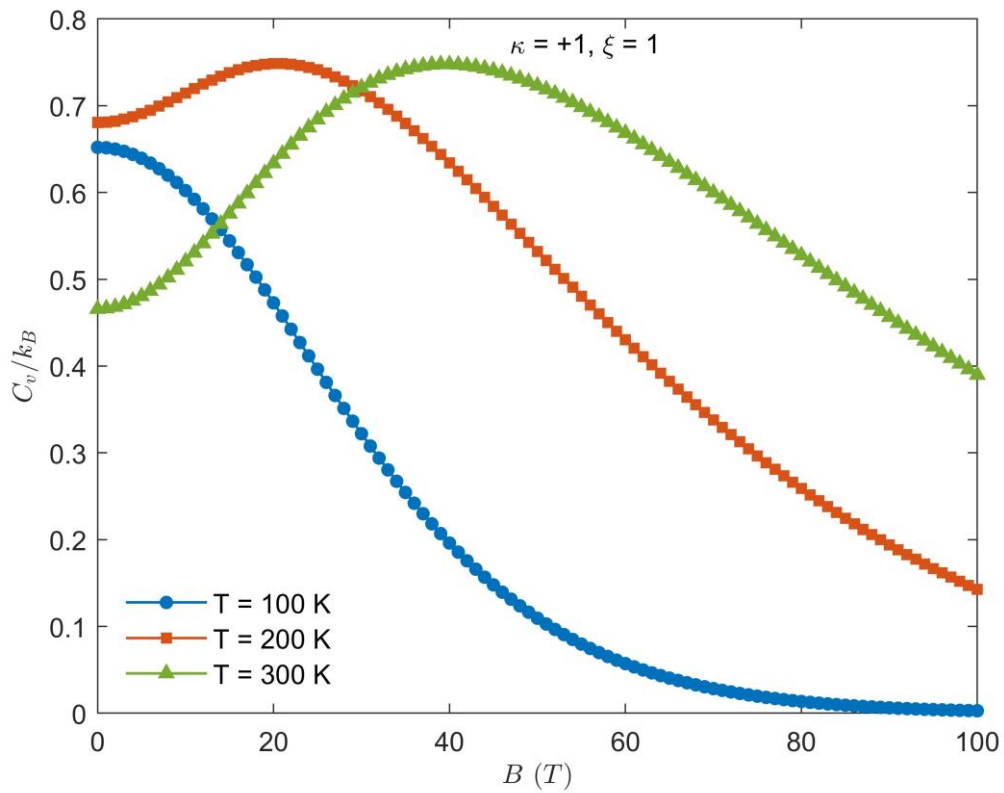


Figure 4.35: Specific heat versus magnetic field for donor impurity case at different temperature values.

The trends of specific heat were observed more clarity in Figure 4.36, which is (a) a 3D plot and (b) contour plot between temperature, magnetic field and the specific heat.

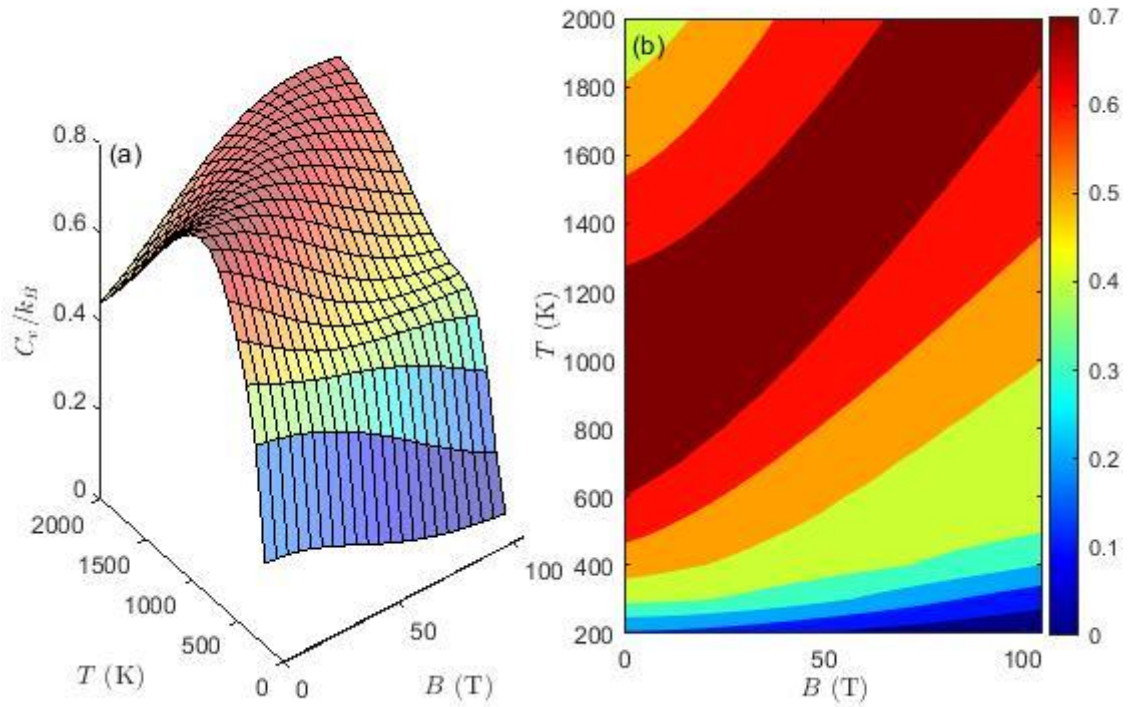


Figure 4.36: (a) 3D plot and (b) contour plot of specific heat with temperature and magnetic field.

The confinement potential significantly influences the specific heat as shown in Figure 4.37 with ($B= 5\text{T}$, $\omega_0= 10\text{ THz}$, $R_0= 15\text{ nm}$, $\kappa= +1$ and $\zeta= 1$)., when the potential is 10 meV , the specific heat is increasing rapidly with temperature and more slowly at higher V_0 . Also, the specific heat at 10 meV exhibits a peak at approximately 150 K , which shifts to higher temperature and broadens when V_0 was increased up to 30 and 80 meV . This because the strong confinement leads to higher thermal energy required to achieve maximum specific heat.

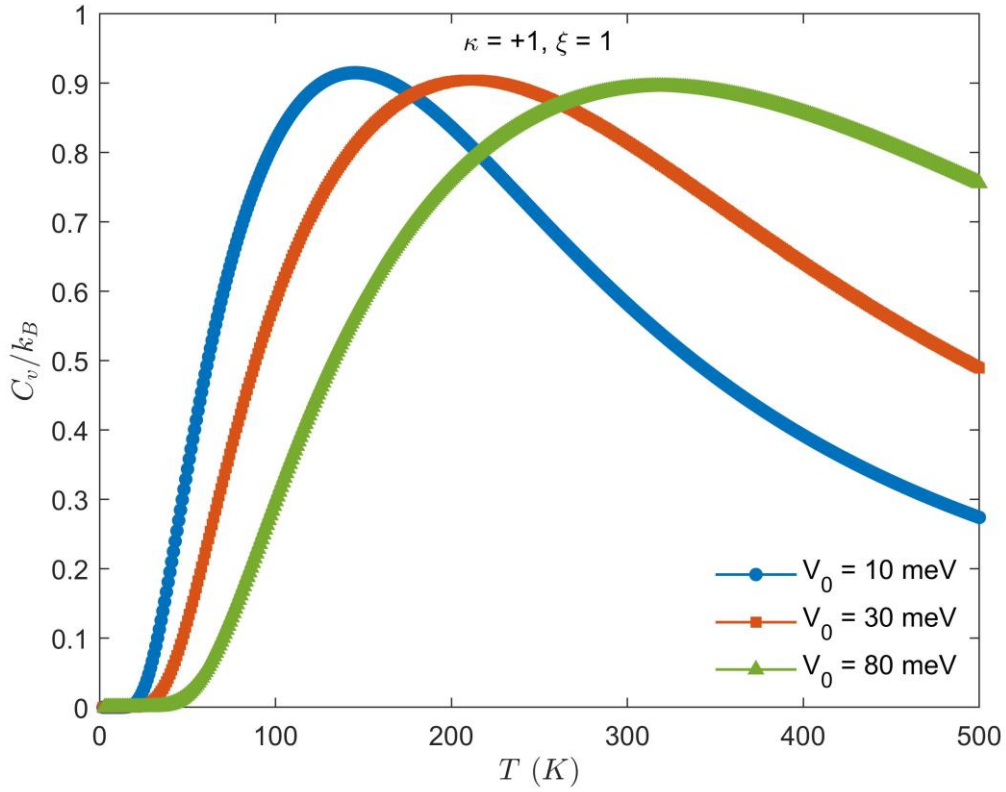


Figure 4.37: Specific heat versus temperature for donor impurity case at different confinement potential values.

4.2.4 Entropy (S)

The quantum particle populates only the lowest energy level at very low temperature, the lowest energy level is the most stable, and this explains the small value of entropy [67]. As the temperature increases, the particle's kinetic energy increases, and higher energy levels also start being populated. The probability of the particle to be at different energy levels rises, so the particle does not localize. The randomness is then increasing, and effectively the entropy of the system [67]. To ensure this, the computed results for the entropy are shown in the same order they appeared previously. Figure 4.38 illustrates the entropy against temperature with and without the impurity effect with $B=5$ T, $\omega_0=10$ THz, $V_0=30$ meV and $R_0=15$ nm, for $\zeta=0$ and 1. The entropy enhances with increasing the temperature with similar shapes for three cases of impurity. By varying the value of ζ from 0 to 1, the entropy has duplicated by values with no change in its behavior. This happens since the quantum ring adds another spatial degree of freedom compared to the purely confined quantum dot.

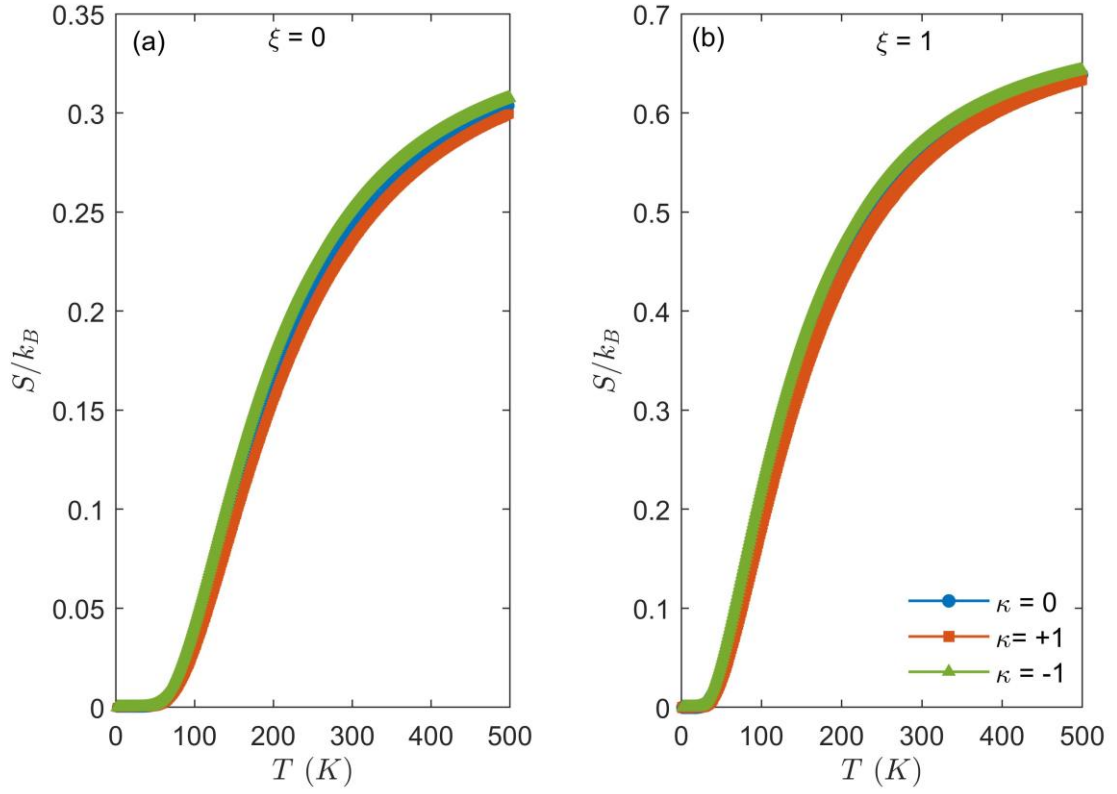


Figure 4.38: Entropy versus temperature with and without the impurity effect for (a) $\xi = 0$ and (b) $\xi = 1$.

The entropy as a function of the temperature is presented in Figure 4.39, for $B = 1, 10$ and 20 T with $\omega_0 = 10$ THz, $V_0 = 30$ meV, $R_0 = 15$ nm, $\kappa = +1$ and $\xi = 1$. It is clearly seen that the entropy rises with the temperature enhancement at a fixed value of the magnetic field. However, the entropy declines as the magnetic field enhances because the magnetic field restricts the number of available energy states and enhances confinement, which reduce the system's disorder.

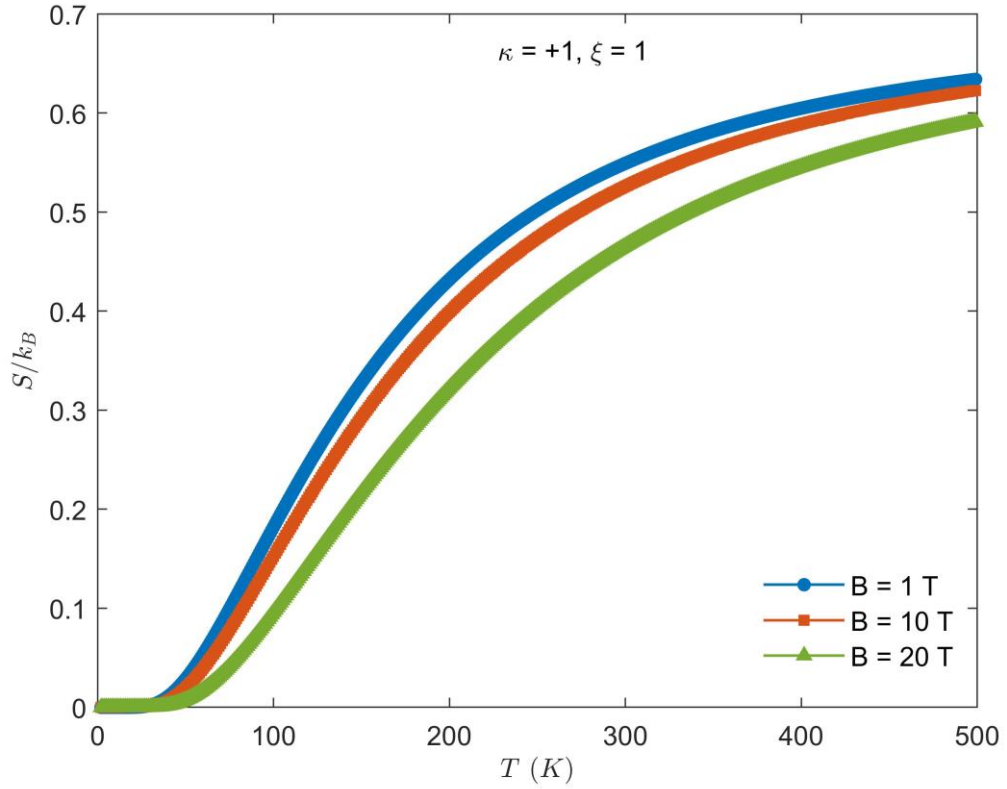


Figure 4.39: Entropy versus temperature for donor impurity case at different magnetic field values.

The influence of magnetic field on the entropy of the system at constant temperature 100 K is plotted in Figure 4.40 with and without impurity for $\zeta = 0$ and $\zeta = 1$ with $\omega_0 = 10$ THz, $V_0 = 30$ meV, $R_0 = 15$ nm. It is observed from Figure 4.40 (a) that the entropy is quickly decreasing as the magnetic field gets stronger until 30 T, above this value the entropy is decreasing slowly. Considering $\zeta = 1$, the entropy declines in the same shape as first case with magnetic field but the values become higher.

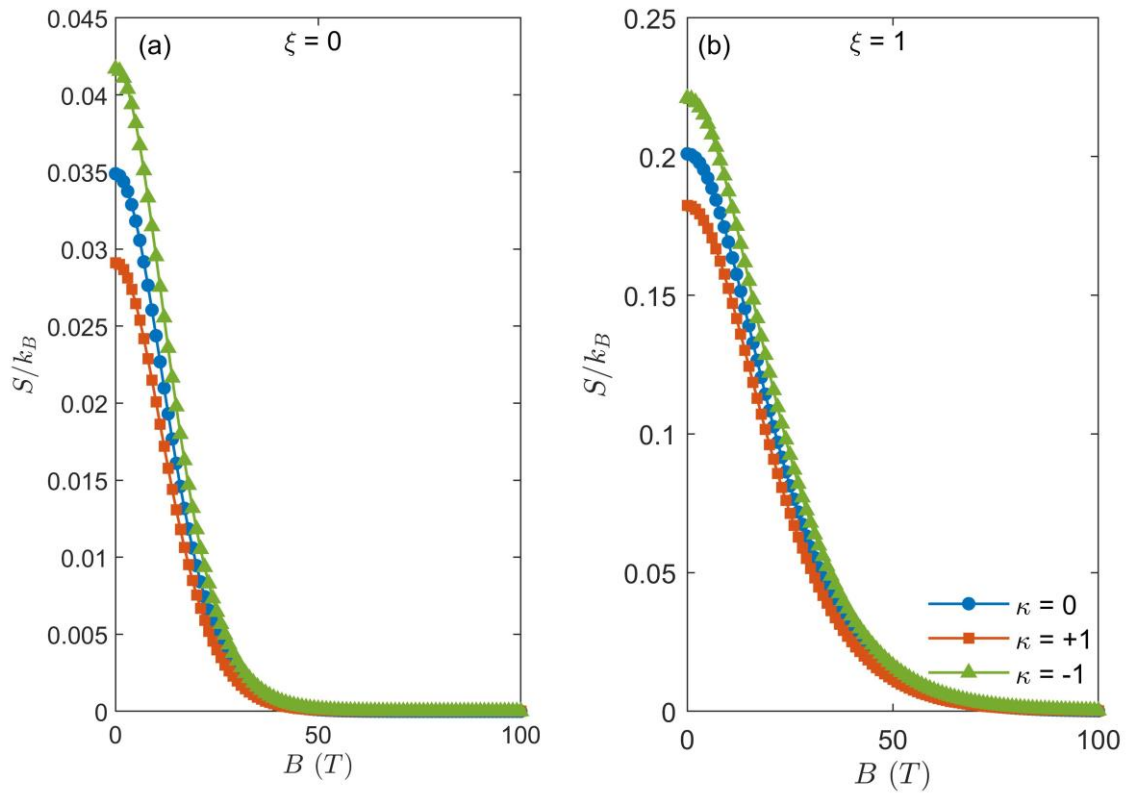


Figure 4.40: Entropy versus magnetic field with and without the impurity effect for (a) $\zeta=0$ and (b) $\zeta=1$.

In Figure 4.41, the entropy is presented as function of magnetic field with different temperatures for donor impurity QD/QR system with $\omega_0=10$ THz, $V_0=30$ meV, $R_0=15$ nm, $\kappa=+1$ and $\zeta=1$. The entropy has decreased with enhancement of the magnetic field for fixed temperature value in the same shape as discussed above. By enhancing the temperature value, the S - B lines gets higher.

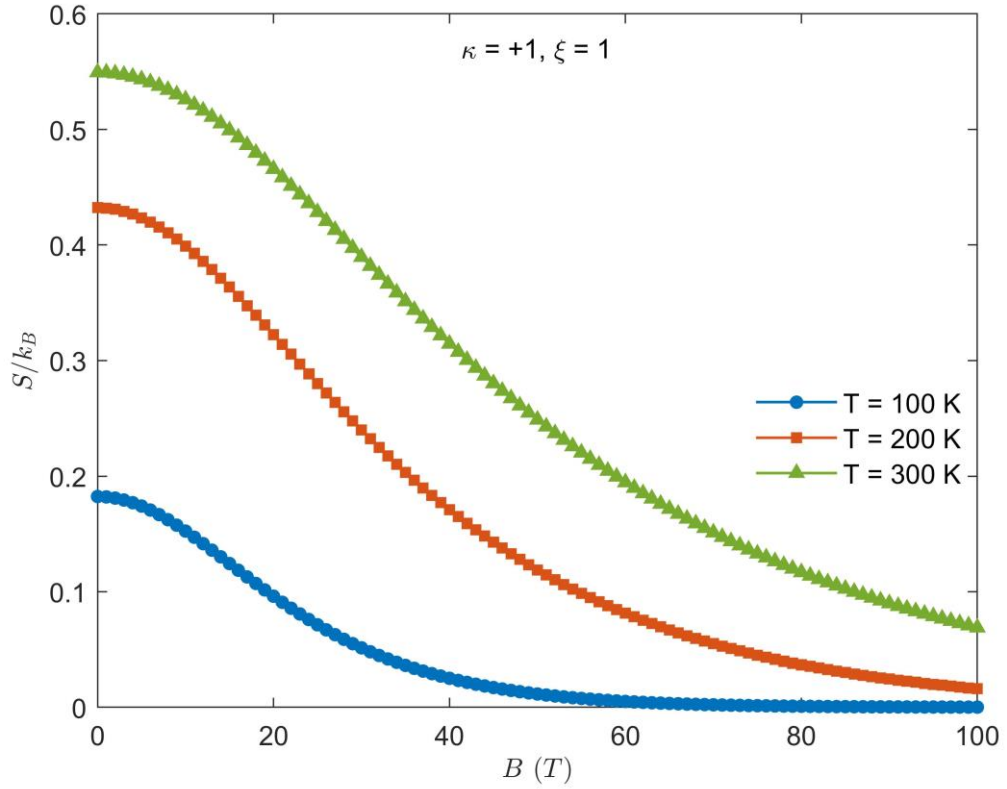


Figure 4.41: Entropy versus magnetic field for donor impurity case at different temperature values.

The entropy is significantly affected by the energy levels and their spacing, which are controlled by the confinement potential, the entropy is plotted versus confinement potential for donor impurity in QD/QR system with $B= 5$ T, $\omega_0= 10$ THz, $R_0= 15$ nm, $\kappa= +1$ and $\zeta= 1$ in Figure 4.42. At low potential, the energy levels are closely spaced, allowing more energy states to be accessible at fixed temperature, resulting in higher entropy. Whereas increasing the confinement potential leads to widely spaced energy levels, fewer particles have sufficient thermal energy to reach the higher energy levels, this reducing the number of accessible states at a given temperature, resulting lower entropy.

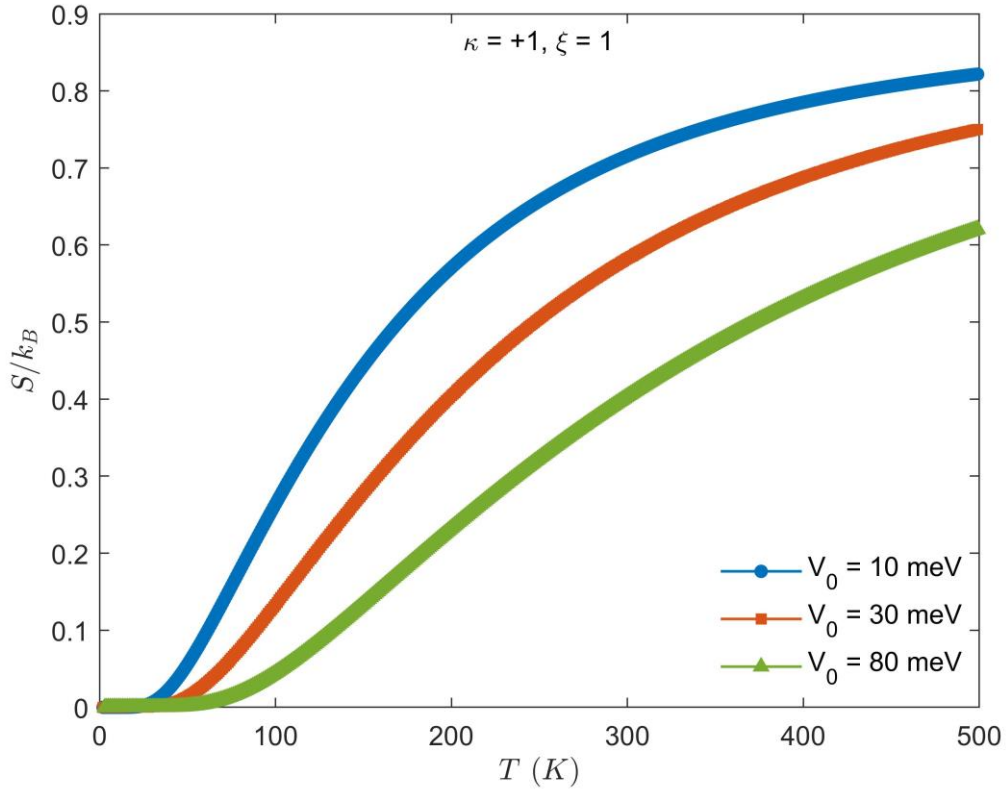


Figure 4.42: Entropy versus temperature for donor impurity case at different confinement potential values.

4.2.5 Magneto-Caloric Effect (MCE)

The changes of magnetic entropy, the entropy at a specified magnetic field $S(B= 1$ T) minus the entropy at a zero magnetic field $S(B= 0$ T) is studied in this section. The magneto-caloric effect measures the difference between these two values of entropy as a function of temperature, it has been presented in Figure 4.43 with $B= 5$ T, $\omega_0= 10$ THz, $V_0= 30$ meV and $R_0= 15$ nm, considering the QD case ($\zeta= 0$) and QD/QR ($\zeta= 1$) for several values of the κ -parameter: donor impurity ($\kappa= +1$), acceptor impurity ($\kappa= -1$), and without impurity ($\kappa= 0$).

One can see from Figure 4.43 a pronounced maximum at low temperatures (200 K). Or see a pronounced minimum because in fact the equation of ΔS is multiplied by negative sign. Regarding to the impurity effect on the magneto-caloric effect, The maximum that appears in the case of the absence of impurity is very slightly lowered and shifted toward the higher temperature for $\kappa= +1$ and rises and shifted to the left for $\kappa= -1$ case. Also, by

switching the value ζ from 0 to 1, the plot only shifts upwards with no apparent change in the shape of the plot.

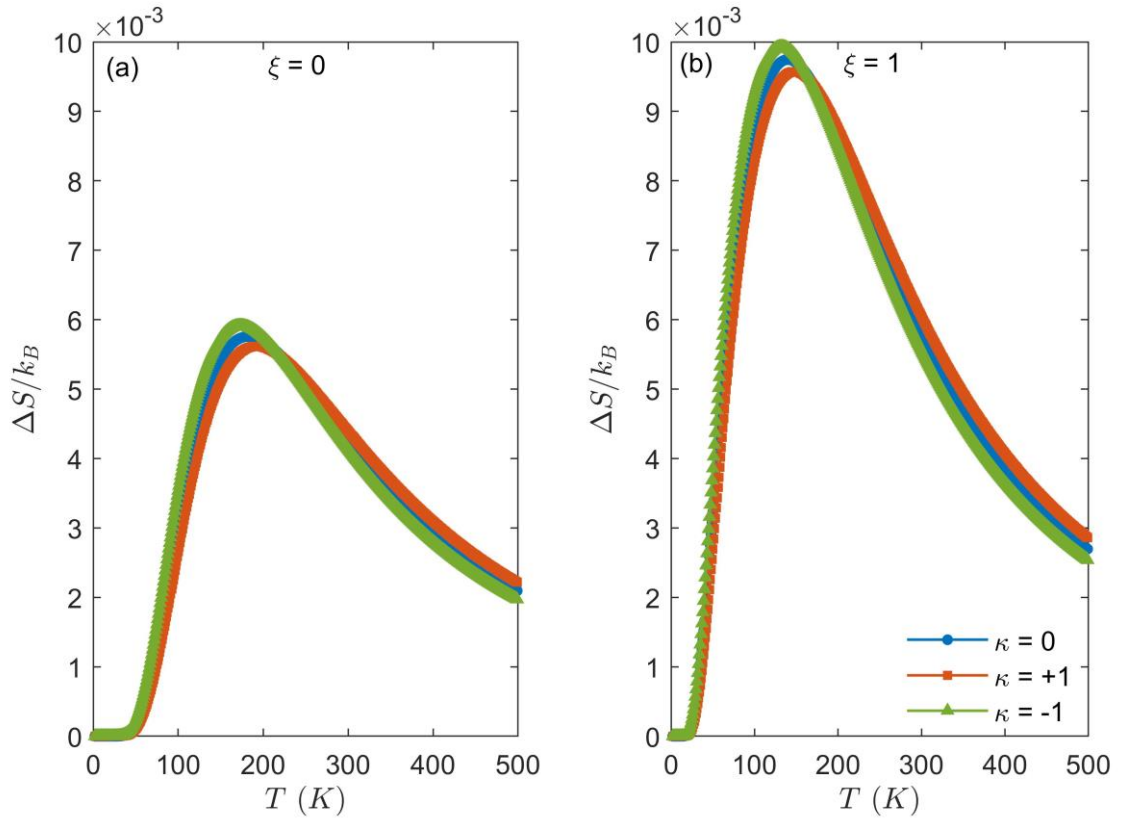


Figure 4.43: Variation of entropy versus temperature with and without the impurity effect for (a) $\xi=0$ and (b) $\xi=1$.

Figure 4.44 displays the variations of entropy as a function of the temperature for different values of B with $\omega_0=10$ THz, $V_0=30$ meV, $R_0=15$ nm, $\kappa=+1$ and $\xi=1$. It is observed that with increasing B , the height of the maximum of entropy change rises and becomes wider. At high temperatures, the effect diminishes as the entropy change becomes less significant compared to the overall thermal energy distribution.

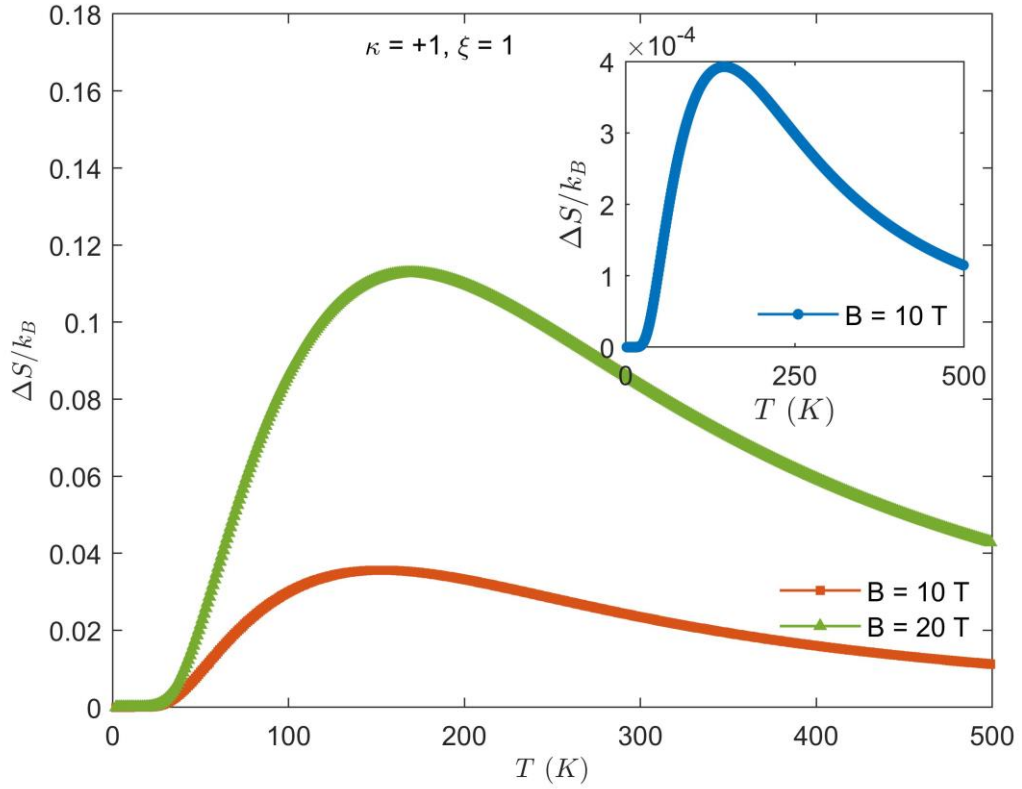


Figure 4.44: Variation of entropy versus temperature for donor impurity case at different magnetic field values.

The effect of the magnetic field on the entropy change is studied with $T= 100$ K $\omega_0= 10$ THz, $V_0= 30$ meV and $R_0= 15$ nm, considering the QD case ($\xi= 0$) and QD/QR ($\xi= 1$) for several values of the κ -parameter. In the case of QD disk, the change of entropy increases almost linearly until $B= 30$ T and then converges to the saturation. Whereas for $\xi= 1$, the entropy changes has the same behavior with higher values. With respect to the impurity effect, the behavior does not change for all impurity cases but the impurity affected above 30 T. Details are provided in Figure 4.45.

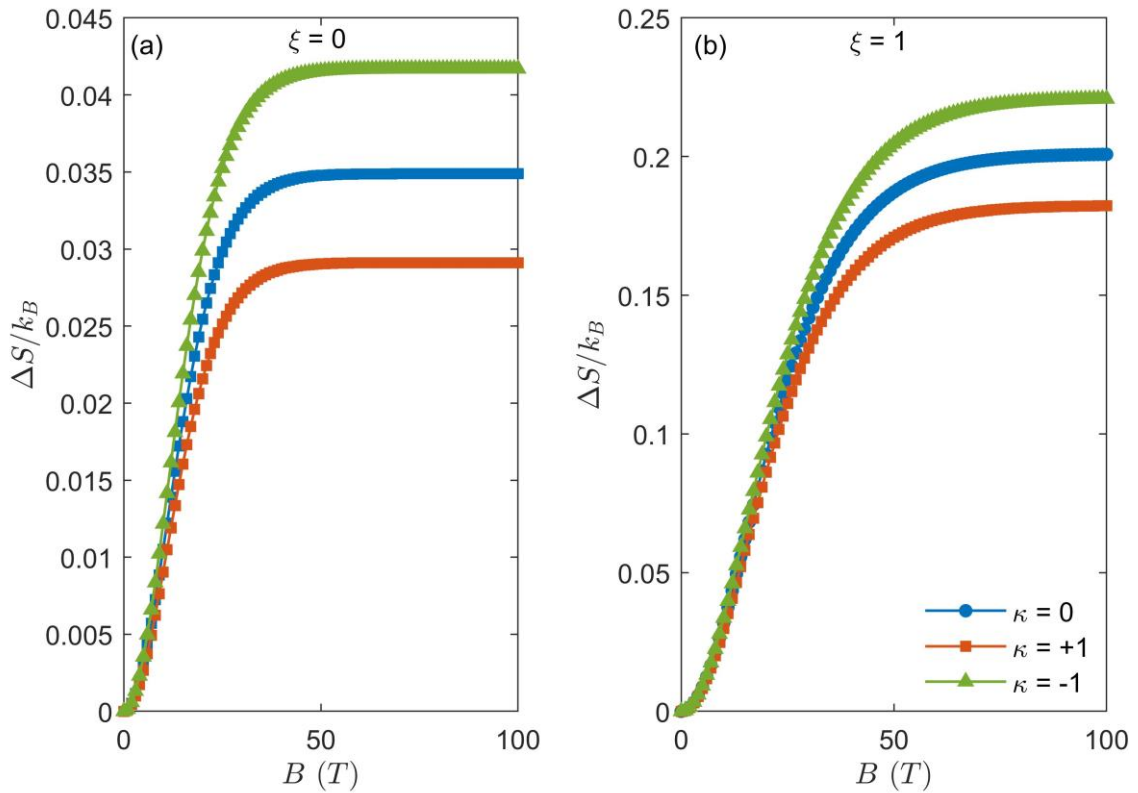


Figure 4.45: Variation of entropy versus magnetic field with and without the impurity effect for (a) $\zeta = 0$ and (b) $\zeta = 1$.

The variations of the entropy change versus magnetic field for different temperatures values are investigated in Figure 4.46 with $\omega_0 = 10$ THz, $V_0 = 30$ meV, $R_0 = 15$ nm, $\kappa = +1$ and $\zeta = 1$. It can be seen that At $T = 100$ K, the entropy change increases with magnetic fields up to 40 T and then it becomes constant with B . With raising T values to 200 K and 300 K, ΔS is increasing overall the B -range. Moreover, it is noted that the behavior of the change of entropy with rising the temperature in the B -range is not systematic.

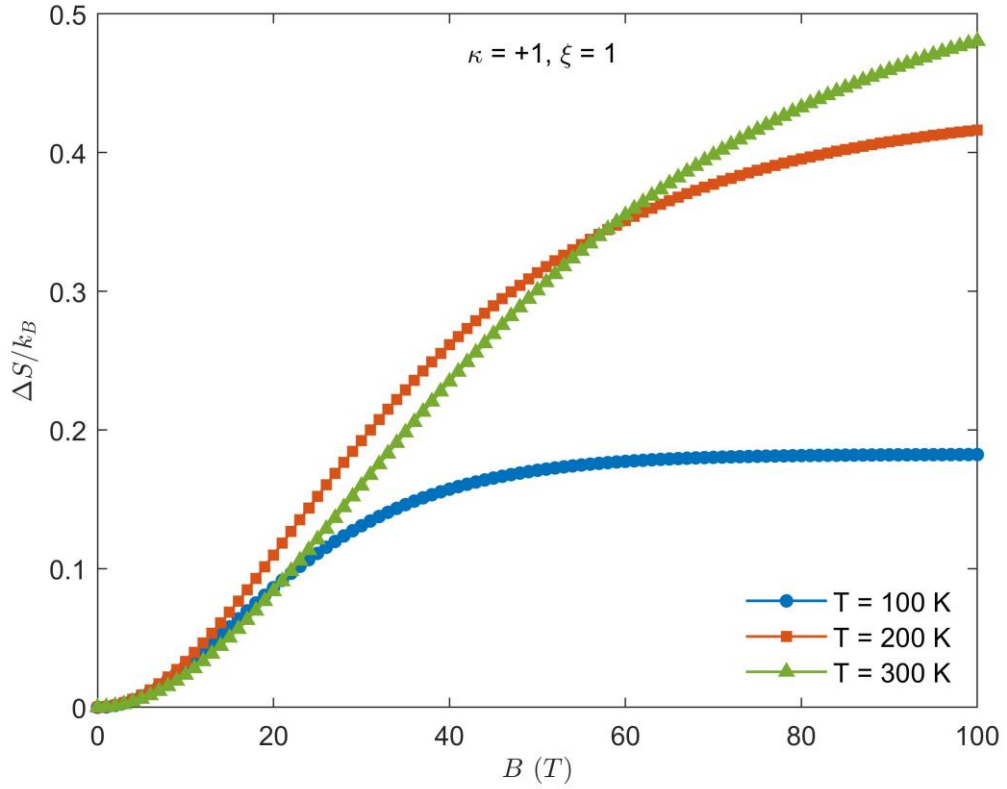


Figure 4.46: Variation of entropy versus magnetic field for donor impurity case at different temperature values.

The effect of confinement potential variation on the magneto-caloric effect in a QD/QR system is illustrated in Figure 4.47 in the presence of donor impurity with $B= 5$ T, $\omega_0= 10$ THz, $R_0= 15$ nm, $\kappa= +1$ and $\zeta= 1$, the magneto-caloric effect is more significant at low and intermediate temperatures for systems with low confinement potential values. Larger change of entropy is resulted because the closely spaced energy levels, resulting in a more pronounced magneto-caloric effect when a magnetic field is applied or removed. Higher V_0 leads to smaller changes in entropy, resulting in a less pronounced magneto-caloric effect.

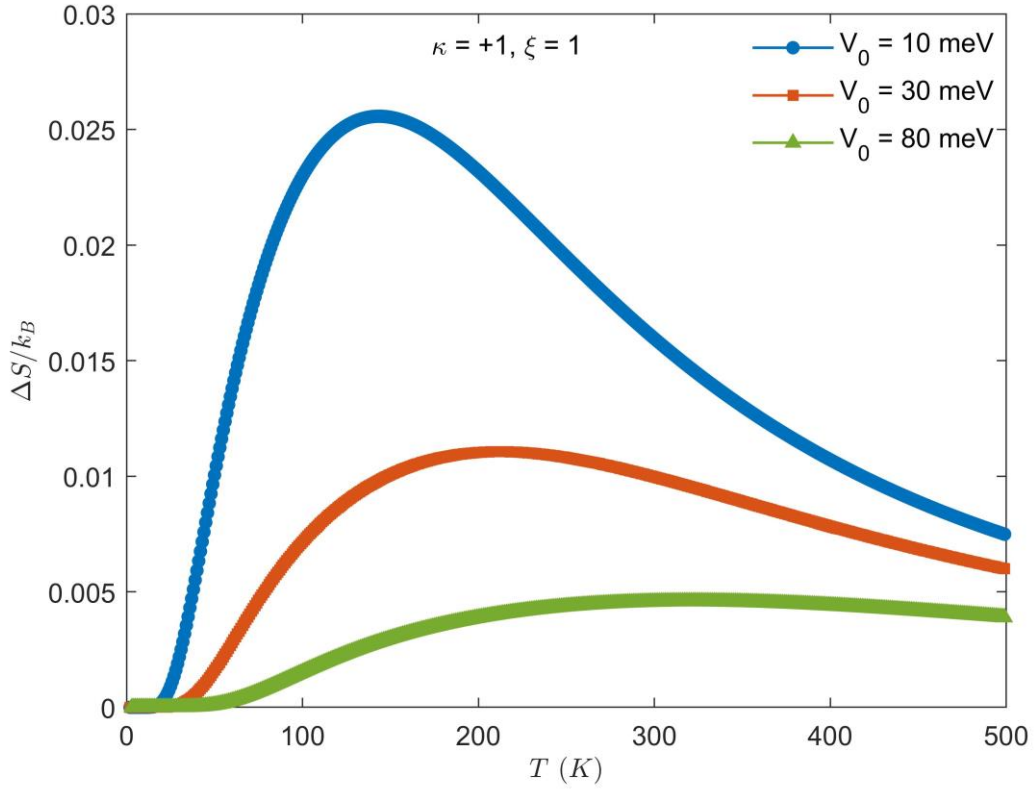


Figure 4.47: Variation of entropy versus temperature for donor impurity case at different confinement potential values.

The impurity affects the energy levels of the QD and the electronic and thermodynamic properties of the system is varied. It is worth mentioning that all thermodynamic properties decrease with temperature if the impurity is donor. This is physically explained by the following: there is a negative Coulomb contribution due to attractive potential between the impurity. In contrast, all thermodynamic characteristics are increasing if the impurity is acceptor due to that the electron transfers from valence band to an acceptor state, it leaves behind a hole. The top of the valence band and the energy levels of acceptor impurities are very near each other. In the presence of acceptor impurity, there is a repulsive coulomb potential of the impurity, which make the electron feels the effect of impurity and hence the energy level is pulled up [34].

4.3 Magnetic Properties

In order to obtain our desired results for the magnetic properties of the system, the computed results for the magnetic quantities, the magnetization and the magnetic susceptibility are presented in this section. Making use of the corresponding statistical energy shown previously.

4.3.1 The Magnetization (M)

In this section, the computed results for the magnetization (M) of the system is presented as a function of different physical parameters. The magnetization had been calculated in unit of effective Bohr magneton (μ_B). The variation of M as a function of temperature is presented in Figure 4.48 for $B= 5$ T, $\omega_0= 10$ THz, $V_0= 30$ meV and $R_0= 15$ nm, considering the QD case ($\zeta= 0$) and QD/QR ($\zeta= 1$) for several values of the κ - parameter: 0, +1 and -1.

In the absence of impurity, the magnetization is constant with temperature until 50 K is reached, with increasing temperature, M rises until reaches critical value (maximum), and then it starts decreasing. This behavior is common for two cases of impurity and the peak occurs at same position with the difference that it is higher for donor impurity and lower in the acceptor impurity case. Additionally, by changing ζ parameter from 0 to 1, the magnetization against temperature with impurity effect did not change.

The discrete energy levels in QDs and QRs systems influence the temperature dependence of magnetization. The spacing between the these levels is small, Therefore, higher energy states are more strongly populated by thermal excitation. The peak of magnetization may be associated with the access of electron to the energy levels that more efficiently contribute to magnetic alignment at specific temperatures. Above this point, the overall magnetization decreases due to the thermal population of higher, less magnetically favorable states.

Additionally, the presence of impurities can modify the temperature dependence of magnetization. The impurity states can contribute to the magnetic moment of the system at low temperature. As the temperature increases, the interaction between the impurities

and the thermal excitation of carriers can lead to increased disorder, further contributing to the decrease in magnetization after the peak.

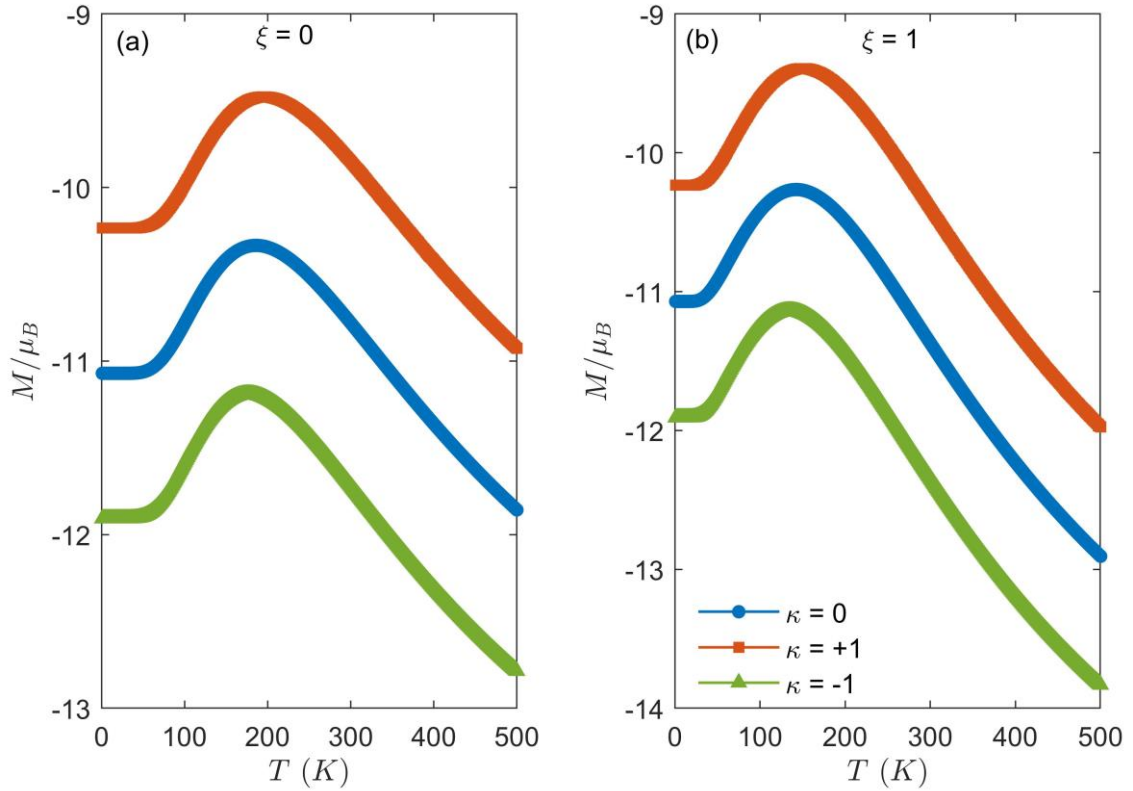


Figure 4.48: Magnetization versus temperature with and without the impurity effect for (a) $\xi=0$ and (b) $\xi=1$.

The Magnetization is plotted against temperature with different values of magnetic field for QD/QR system with $\omega_0=10$ THz, $V_0=30$ meV, $R_0=15$ nm, $\kappa=+1$ and $\xi=1$. As it is clear from Figure 4.49, M is little affected by temperature at low magnetic field (1 T). For fields larger than 1 T which is reported as stronger magnetic field values, it tends to remain constant then increases slightly with rising temperature and after that it decreases. Also, the magnetization reduces as the magnetic field rises.

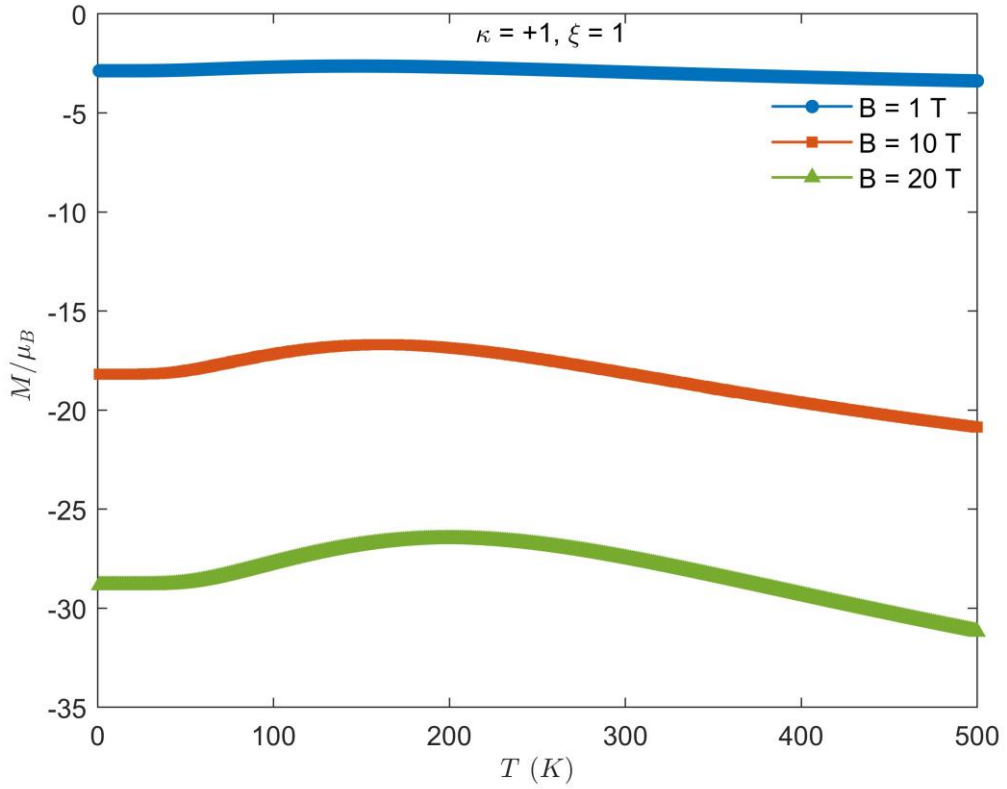


Figure 4.49: Magnetization versus temperature for donor impurity case at different magnetic field values.

The effect of impurity on the magnetization as a function of magnetic field is examined in Figure 4.50 for QD and QD/QR system with $T= 100$ K, $\omega_0= 10$ THz, $V_0= 30$ meV and $R_0= 15$ nm. The figure shows that in low magnetic field region, the magnetization decreases rapidly to negative values as the magnetic field strength increases and the impurity has no effect. M is decreasing faster than that in the higher magnetic field. For $B= 50-100$ T, the magnetization is constant and the impurity effect plays a role in the values of magnetization. The explanation to this behavior of $M-B$ is that; as the magnetic field increases, the occupancy of a higher angular momentum state gets energetically suitable, lead to the decreasing of magnetization.

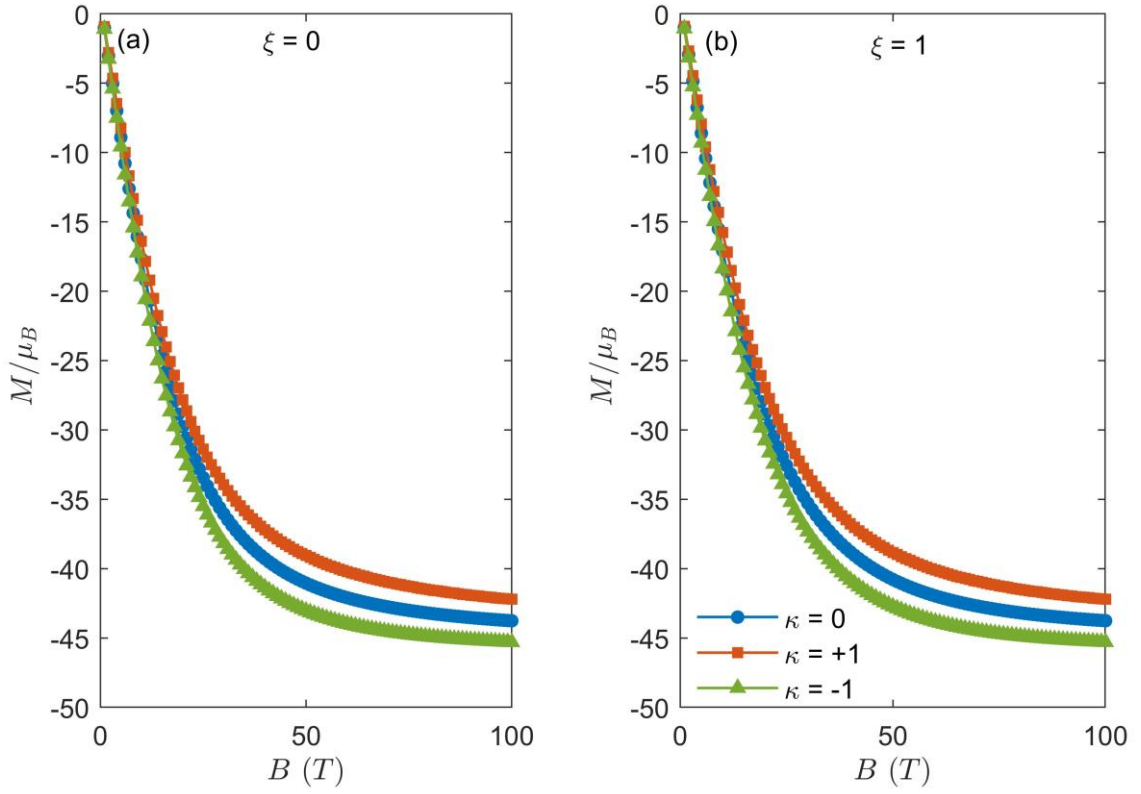


Figure 4.50: Magnetization versus magnetic field with and without the impurity effect for (a) $\xi = 0$ and (b) $\xi = 1$.

For fixed values of temperature, the magnetization decreases as the magnetic field strength increases (as shown in Figure 4.51) with parameters $\omega_0 = 10$ THz, $V_0 = 30$ meV, $R_0 = 15$ nm, $\kappa = +1$ and $\zeta = 1$. The decline will be more sharp in the low magnetic field area and not affected with changing the temperature. Above 30 T, the decreasing of magnetization is slower and it is higher for higher temperature at constant B.

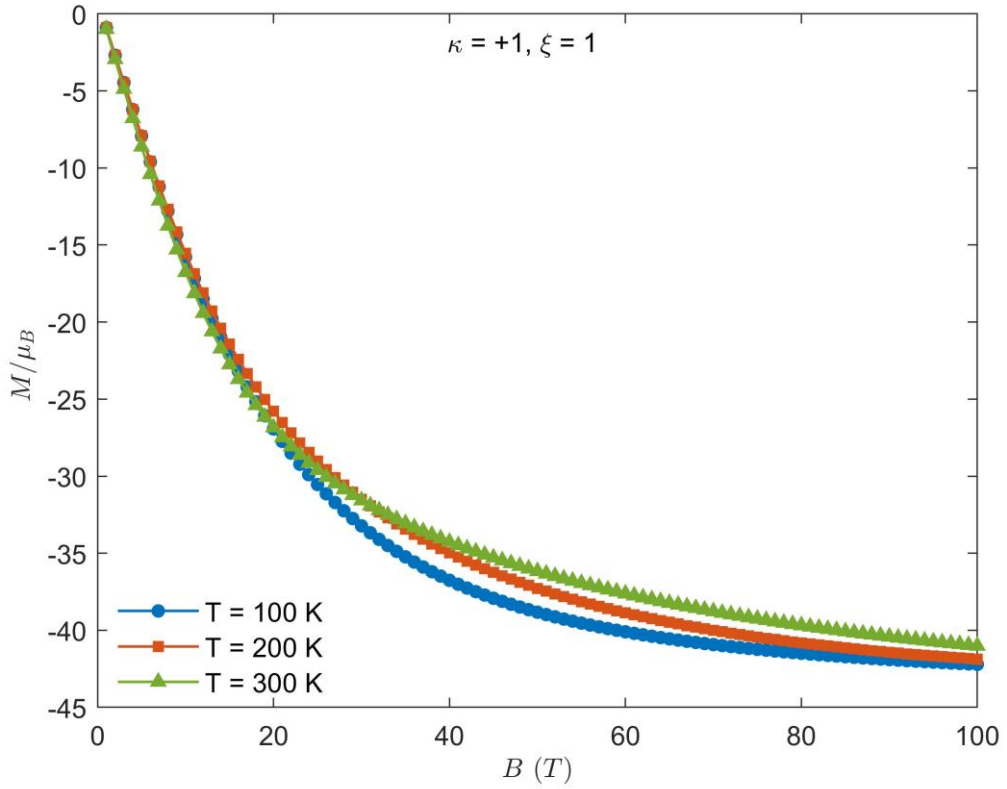


Figure 4.51: Magnetization versus magnetic field for donor impurity case at different temperature values.

The effect of confinement potential on the magnetization was studied by plotting the magnetization with temperature at three different values of confinement potential in Figure 4.52 for donor impurity with $B= 5$ T, $\omega_0= 10$ THz, $R_0= 15$ nm, $\kappa= +1$ and $\zeta= 1$. When the V_0 is 10 meV, it appears that the magnetization is constant with temperature at 50 K then it increases with increasing temperature and reaches a peak at about 150 K, after the peak it decreases. For stronger V_0 , the peak becomes broaden and change in M is very small.

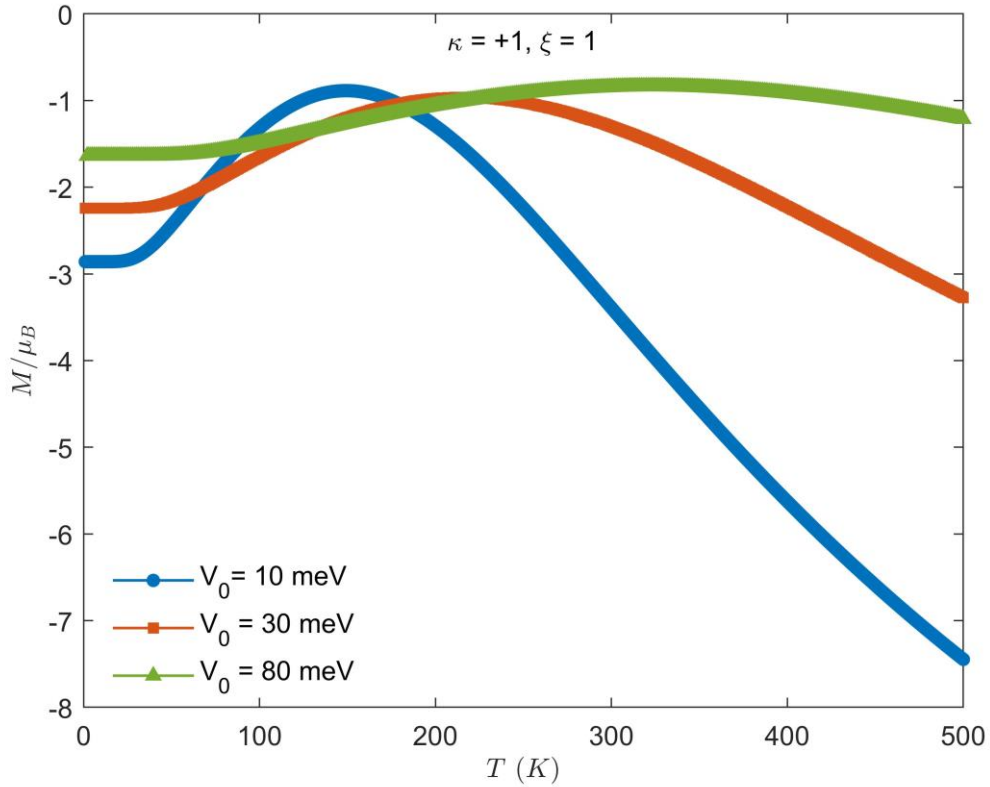


Figure 4.52: Magnetization versus temperature for donor impurity case at different confinement potential values.

4.3.2 The Magnetic Susceptibility (χ)

Figure 4.53 displays the magnetic susceptibility against temperature for two different ζ parameters (0 and 1) with $B= 5$ T, $\omega_0= 10$ THz, $V_0= 30$ meV and $R_0= 15$ nm with and without impurity. Regarding the temperature effect, all curves behave the same behavior. The magnetic susceptibility increases from zero with enhancing the temperature until it reaches the maximum at 100 K. Then, it decreases to reach negative values, leads to the flipping in the sign of χ from paramagnetic ($+\chi$) to diamagnetic material ($-\chi$) [68]. Focusing on Figure 4.53 (b), in the case of $\zeta= 1$, χ shows the same behavior with slight increase in values and shift of the peak toward higher temperature.

The paramagnetic to diamagnetic transition of QD/QR system as the temperature increasing is explained as follows; at low temperature, magnetic susceptibility (χ) is positive because the material is weakly attracted by the magnetic field. This occurs when thermal energy is not strong enough to disrupt the magnetic moments alignment. As

temperature increases, thermal energy becomes stronger and sufficient to cause a transition from paramagnetism to diamagnetism. This happens because thermal fluctuations randomize the magnetic moments, weakening their alignment with the external magnetic field.

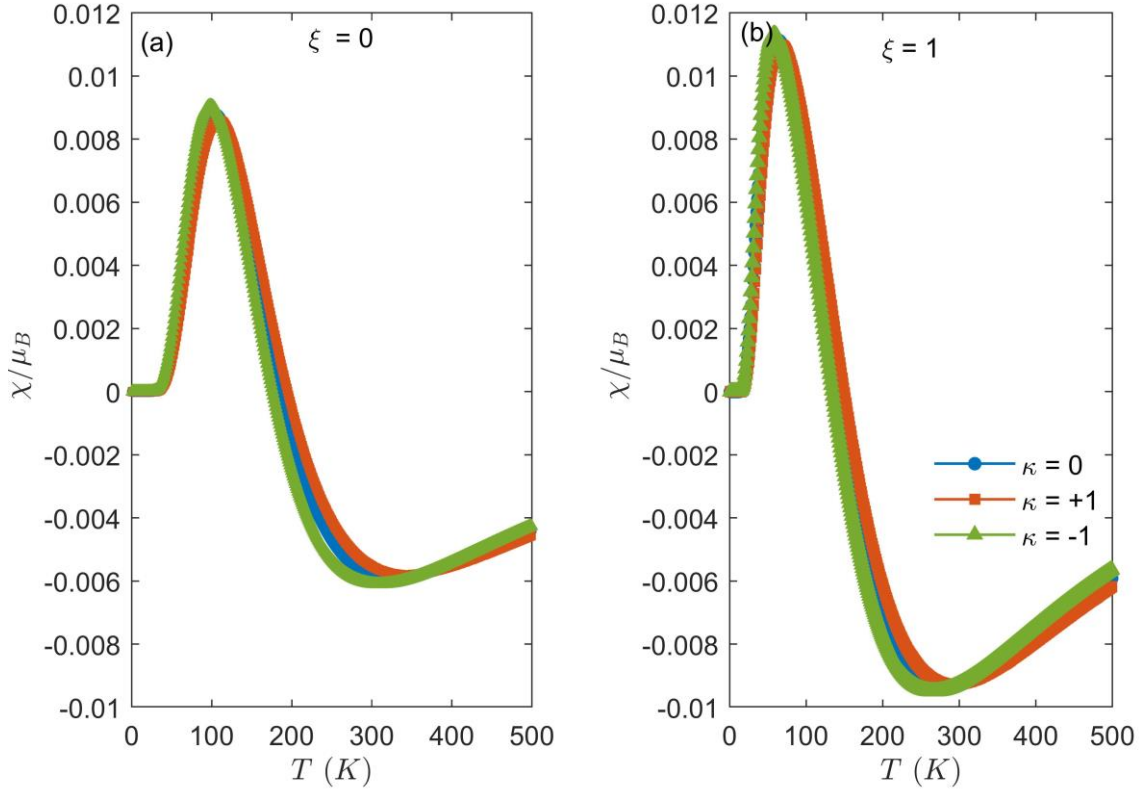


Figure 4.53: Magnetic susceptibility versus temperature with and without the impurity effect for (a) $\zeta=0$ and (b) $\zeta=1$.

The variations of magnetic susceptibility as a function of temperature for different magnetic fields is plotted in Figure 4.54 by considering the presence of donor impurity case with $\omega_0=10$ THz, $V_0=30$ meV, $R_0=15$ nm, $\kappa=+1$ and $\zeta=1$. An oscillating behavior had been seen in the magnetic susceptibility with different magnetic field values. It is observed that when $B=1$ T, the magnetic susceptibility increases with increasing temperature until it reaches a maximum at 60 K then decreases and gets constant in negative region to the end of the temperature range. Rising B to 10 T, χ displays higher peak at 80 K. After this peak, it decreases to a minimum at 300 K with negative values and return to slowly increase to the end of T -range. This peak is increased and shifted toward the higher temperature with wider shape when the magnetic field reaches 20 T.

Finally, It is noted that the magnetic susceptibility exhibits a transition from positive values to negative values.

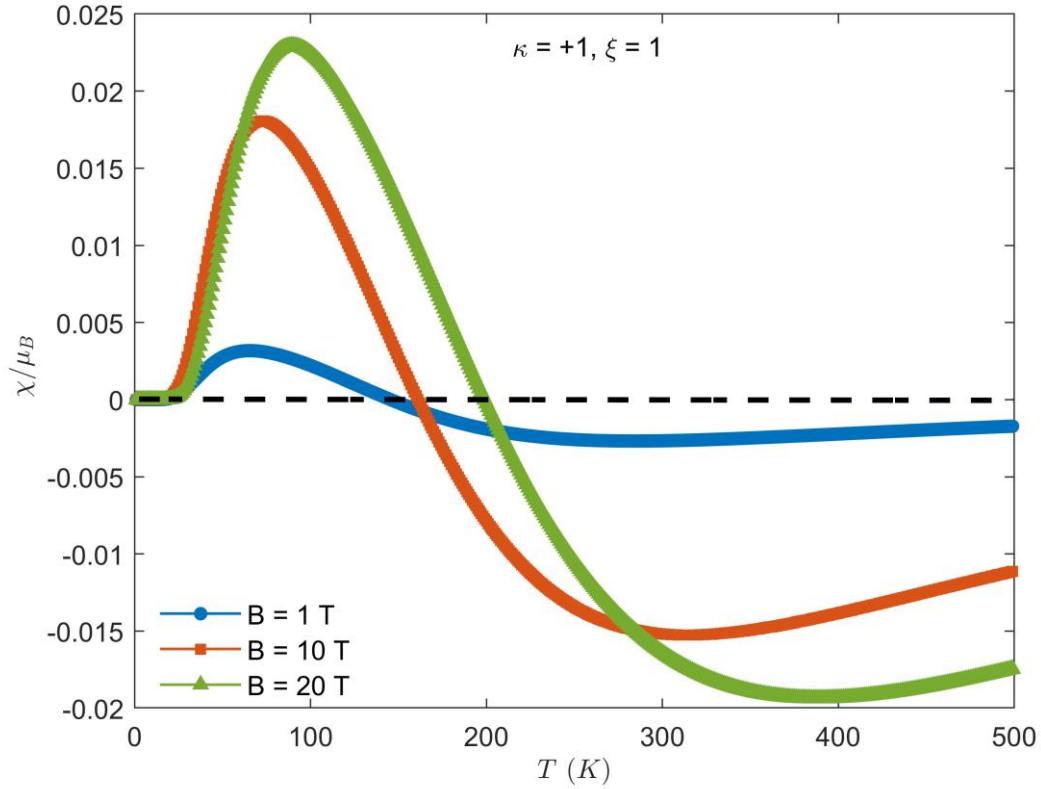


Figure 4.54: Magnetic susceptibility versus temperature for donor impurity case at different magnetic field values.

The dependence of magnetic susceptibility on magnetic field is illustrated in Figure 4.55 with parameters ($T= 100$ K, $\omega_0= 10$ THz, $V_0= 30$ meV, $R_0= 15$ nm)., an interesting behaviour is shown. Regardless of the impurity, the magnetic susceptibility increases to a maximum and then it decreases with increasing the magnetic field. The intensity of maximum is changing by altering the impurity in the case of quantum disk in Figure 4.55 (a). Above 50 T, the magnetic susceptibility is constant. Considering QD/QR in 4.55 (b), χ does not affect by impurities. It has larger values and the peak has a shift toward stronger magnetic field.

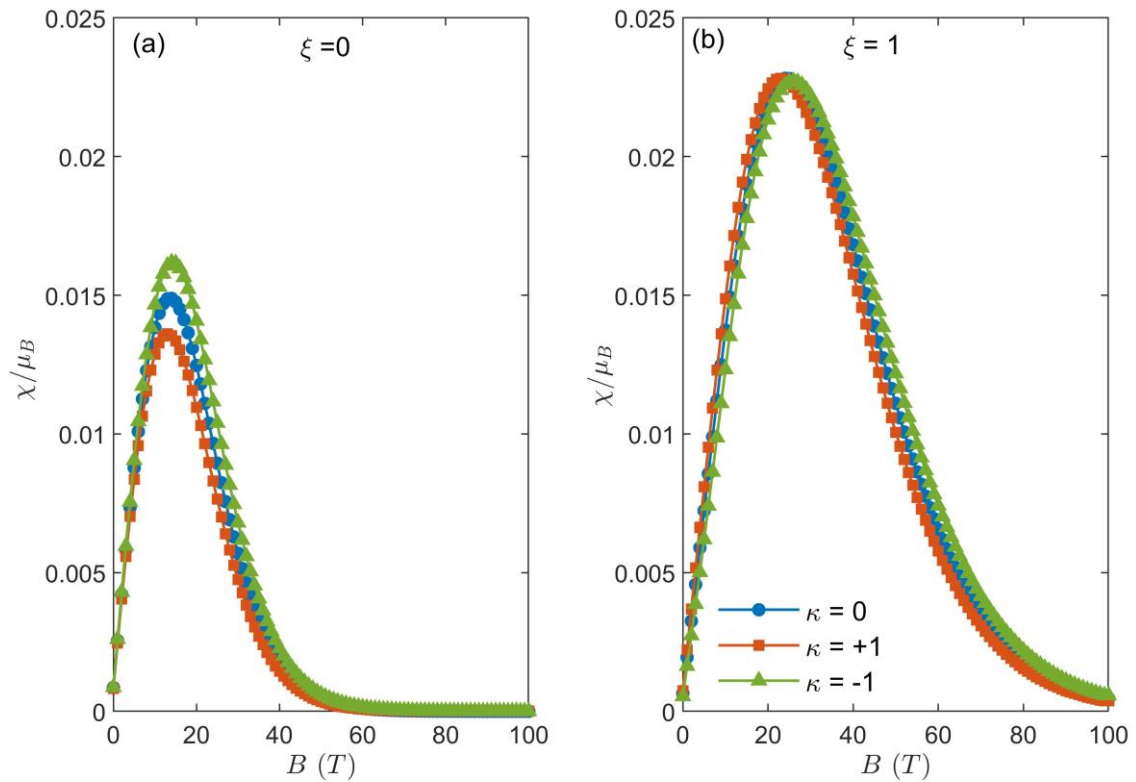


Figure 4.55: Magnetic susceptibility versus magnetic field with and without the impurity effect for (a) $\zeta=0$ and (b) $\zeta=1$.

Figure 4.56 shows the behavior of magnetic susceptibility versus the magnetic field for different values of temperature with $\omega_0=10$ THz, $V_0=30$ meV, $R_0=15$ nm, $\kappa=+1$ and $\zeta=1$. It is seen from the figure that the system has diamagnetic behavior at $T=200$ K and 300 K below 40 T and has a transition from negative value (diamagnetic) to positive value (paramagnetic) in the range of 40 - 100 T. However, with decreasing the temperature to 100 K, the magnetic susceptibility shows an oscillating behavior with increasing magnetic field with positive value (paramagnetic). Another differing point is that χ at 100 K exhibits a maximum with positive value and χ at 200 K and 300 K plays a minimum with negative values.

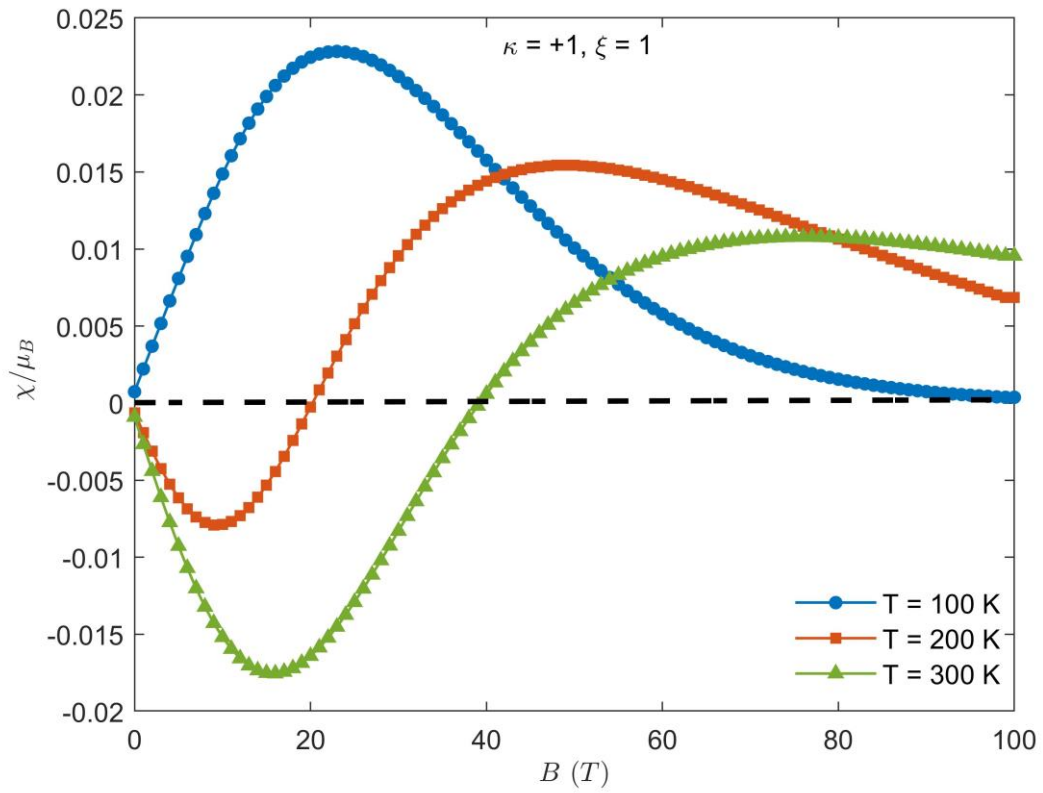


Figure 4.56: Magnetic susceptibility versus magnetic field for donor impurity case at different temperature values.

The trends of magnetic susceptibility were observed more clearly in Figure 4.57, which is (a) a 3D plot and (b) contour plot between temperature, magnetic field and the magnetic susceptibility.

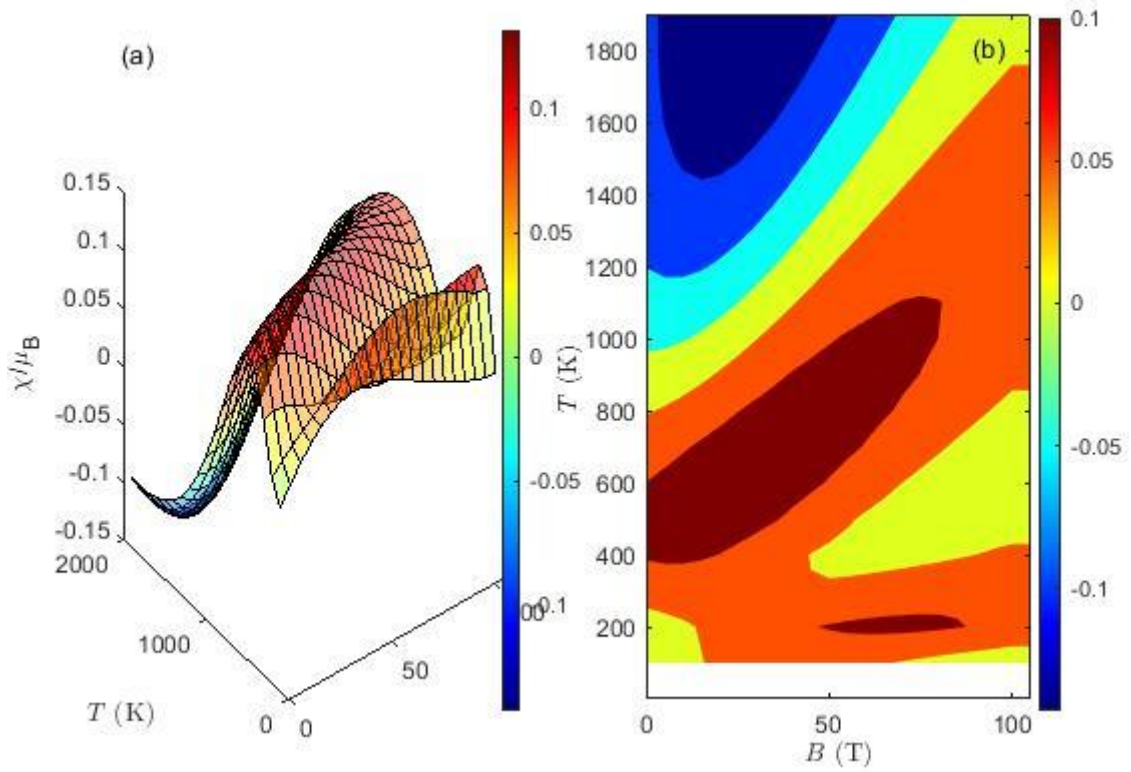


Figure 4.57: (a) 3D plot and (b) contour plot of magnetic susceptibility with temperature and magnetic field.

Now, let's see the effect of confinement potential on the magnetic susceptibility by plotting the magnetic susceptibility with temperature at three different potential values 10 meV, 30 meV and 80 meV with $B=5$ T, $\omega_0=10$ THz, $V_0=30$ meV, $R_0=15$ nm, $\kappa=+1$ and $\xi=1$. At 10 meV, the magnetic susceptibility begins to increase from zero with increasing temperature up to 60 K and exhibits a peak and then begins to decrease from positive to negative values as seen in Figure 4.58.

When the confinement potential is increased further, the same behavior of the magnetic susceptibility with temperature increasing, and here the peak became wider in width and less in height very clearly.

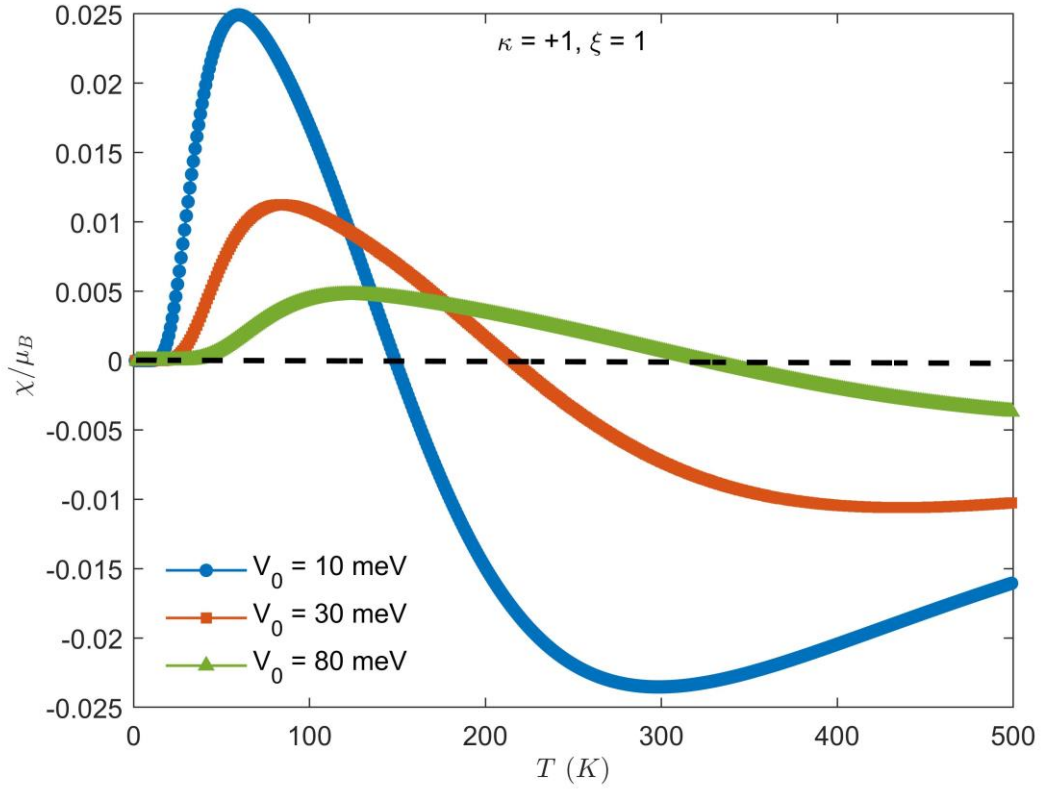


Figure 4.58: magnetic susceptibility versus temperature for donor impurity case at different confinement potential values.

4.4 The Effects of Hydrostatic Pressure and Temperature on the Electronic Properties of the QR/QD System

The effects of the pressure and the temperature on electronic properties with and without impurity in GaAs QD/QR is studied in this section.

First of all, the spectra of ground energy ($n=1$) of confined electron in the QD and QD/QR at constant temperature ($T=300$ K) with and without impurity are described in Figure 4.59 (a) and (b) as a function of pressure with parameters $B=5$ T, $\omega_0=10$ THz, $V_0=30$ meV and $R_0=15$ nm. The figure shows that in the case of quantum disk and absence of impurity, the energy does not vary with pressure. Whereas for the acceptor impurity, E_{mn} versus pressure displays exponential function shape (increases with pressure). The potential landscape of the QD/QR system will be altered in the presence of acceptor impurity. Under pressure, the interaction between charge carriers and the impurity's localized charge becomes stronger, further influencing the energy states. The

donor impurity makes the inversion of exponential function behavior (decreases with pressure). Considering the QD/QR system in (b), the same behavior of plots is obtained.

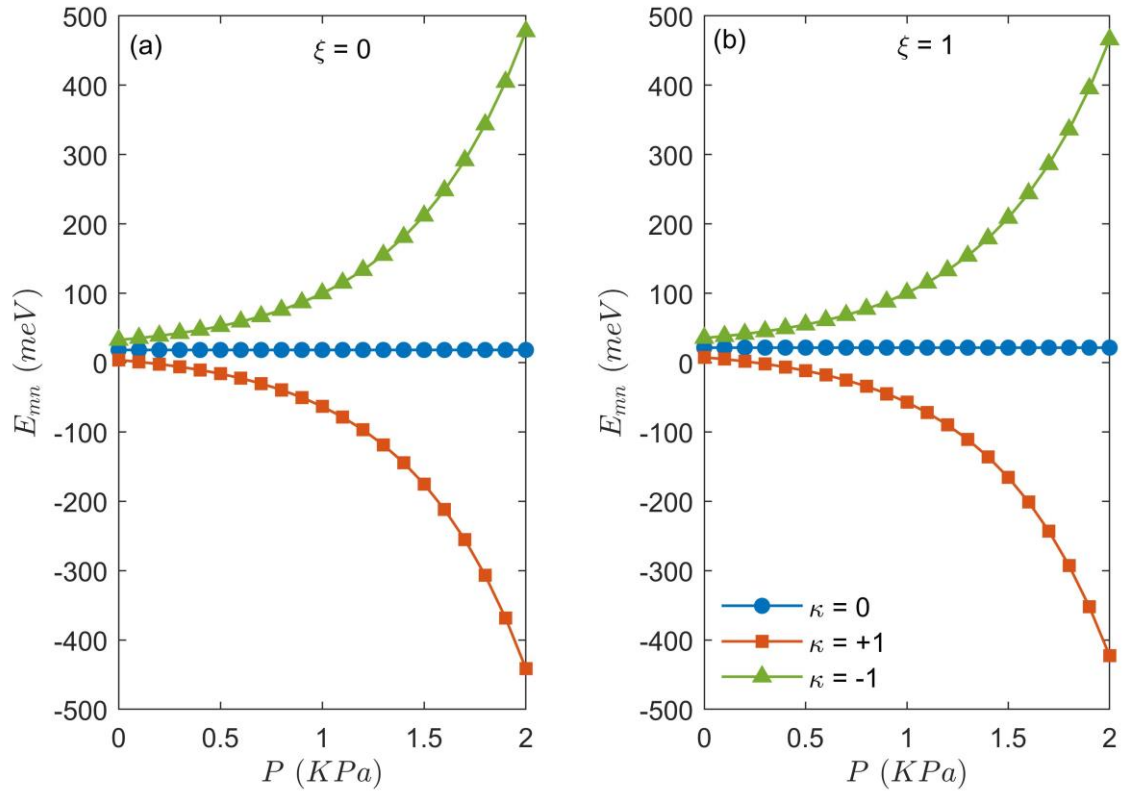


Figure 4.59: Energy of $n=1$ state for a confined electron versus the applied pressure with and without impurity for (a) QD ($\xi=0$) and (b) QD/QR ($\xi=1$).

The results of confined electron energy of ($n=1$) for a given temperature and pressure in the presence of donor impurity for GaAs QD/QR are presented in Figure 4.60 (a)-(d) by varying one parameter, leaving the others fixed. In Figure 4.60 (a), the energy with the variation of applied magnetic field is plotted for $T=300$ K with and without pressure $P=0, 500$ Pa, 1000 Pa with parameters $\omega_0=10$ THz, $V_0=30$ meV and $R_0=15$ nm. It is shown that at these parameters, E_{mn} does not vary with magnetic field but its values decrease with increasing the pressure at fixed temperature.

It is clearly noticed that as the parabolic confinement frequency ω_0 increases, the curves of energy also increase (Figure 4.60 (b)). This is because that as ω_0 increases, the parabolic effective frequency (Ω^2) increases also, which leads to the enhancement of the electron energy due to the parabolic confinement term of the donor impurity Hamiltonian.

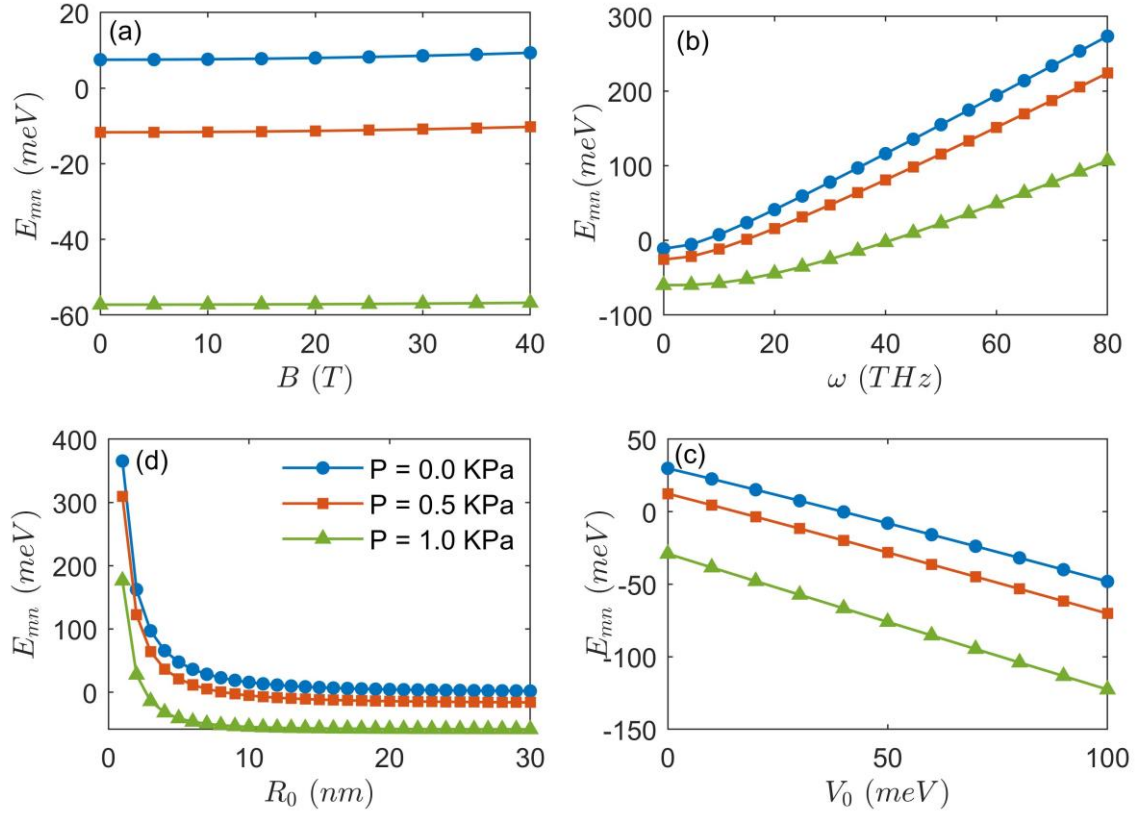


Figure 4.60: Energy of $n=1$ state for a confined electron with three different values of pressure versus (a) the applied magnetic field, (b) confining frequency, (c) confinement potential and (d) the dot radius for QD/QR ($\xi=1$) with donor impurity.

The effect of confining potential on the energy of the system at three different values of pressure is illustrated in Figure 4.60 (c). The energy is linearly decreasing with enhancing the potential at fixed pressure and declining with increasing the potential at fixed pressure.

In addition, the energy of the system is decreasing with a small dot radius values and continue in saturation way. The energy decreases when the pressure increases at fixed R_0 due to the variation of mass and the dielectric constant with the pressure change.

Figure 4.61 (a)-(d) shows the variation of hydrogenic donor impurity binding energy of $n=1$ state with different magnetic field, confining frequency, confining potential and dot radius, respectively. The plots taken at fixed temperature (300 K) with and without the hydrostatic pressure. The binding energy in all graphs rises as the hydrostatic pressure gets higher. This is due to the additional confinement due to the pressure.

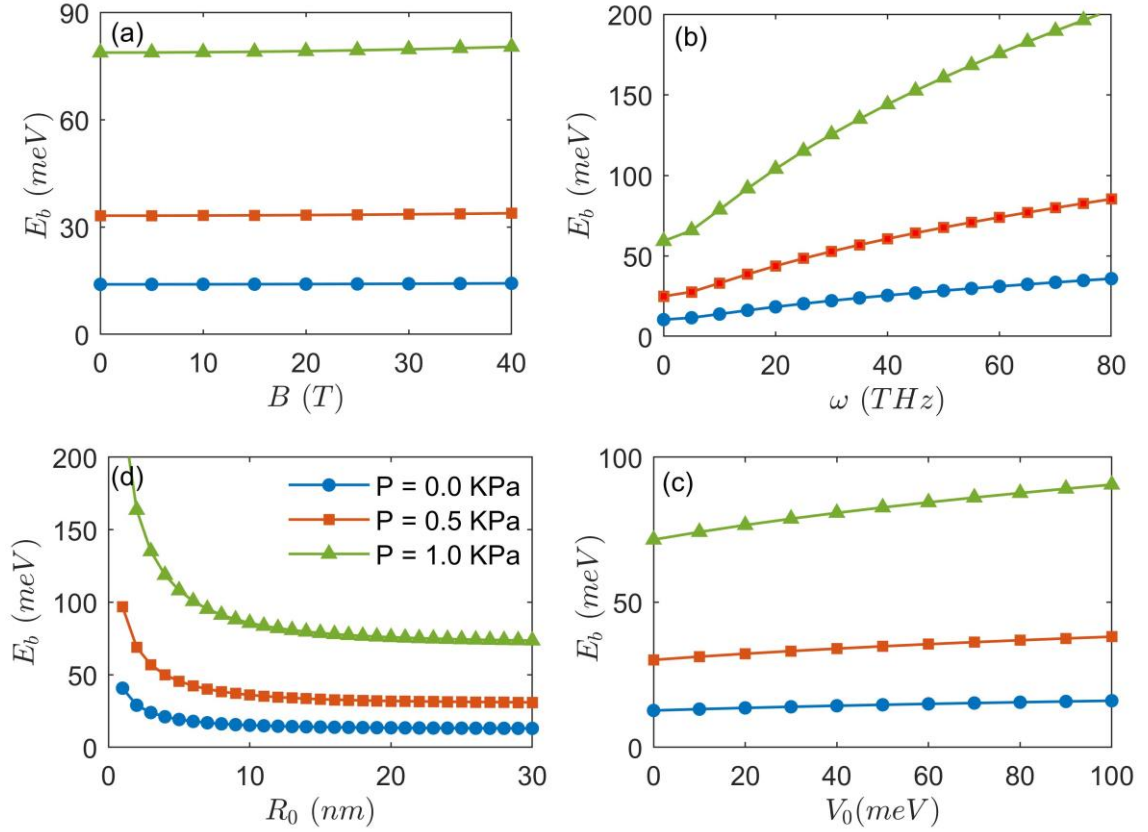


Figure 4.54: The binding energy of $n=1$ state for a confined electron with three different values of pressure versus (a) the applied magnetic field, (b) confining frequency, (c) confinement potential and (d) the dot radius for QD/QR ($\zeta=1$).

Typically, applying the hydrostatic pressure compresses the QD or QR, so the effective confinement potential enhances, this means that the electron is more tightly bound to donor site, rising the binding energy [77].

Moreover, the dependence of effective mass and dielectric constant on the hydrostatic pressure will impact the energy that binds the electron with donor impurity within the system.

Under the pressure, the effective mass is increasing, this implies that the electron has smaller kinetic energy and higher tighting to attractive potential of donor. Also, the dielectric constant is decreasing with increasing the pressure, this enhances the coulomb interaction between electron and donor nucleus, resulting an increase in the binding energy.

The investigation into the density of states (DoS) under the influence of varying pressure, at a given temperature, magnetic field, confinement parameters and impurity type has yielded significant insights into the electronic properties of the material.

Figure 4.62 shows the density of state of QD/QR system at $T= 300$ K, with parameters $B= 5$ T, $\omega_0= 10$ THz, $V_0= 30$ meV, $R_0= 15$ nm and n ranging from 1 to 5 with three impurity cases ($\kappa= 0, +1, -1$). Three different values of pressure were taken in calculating the DoS with energy.

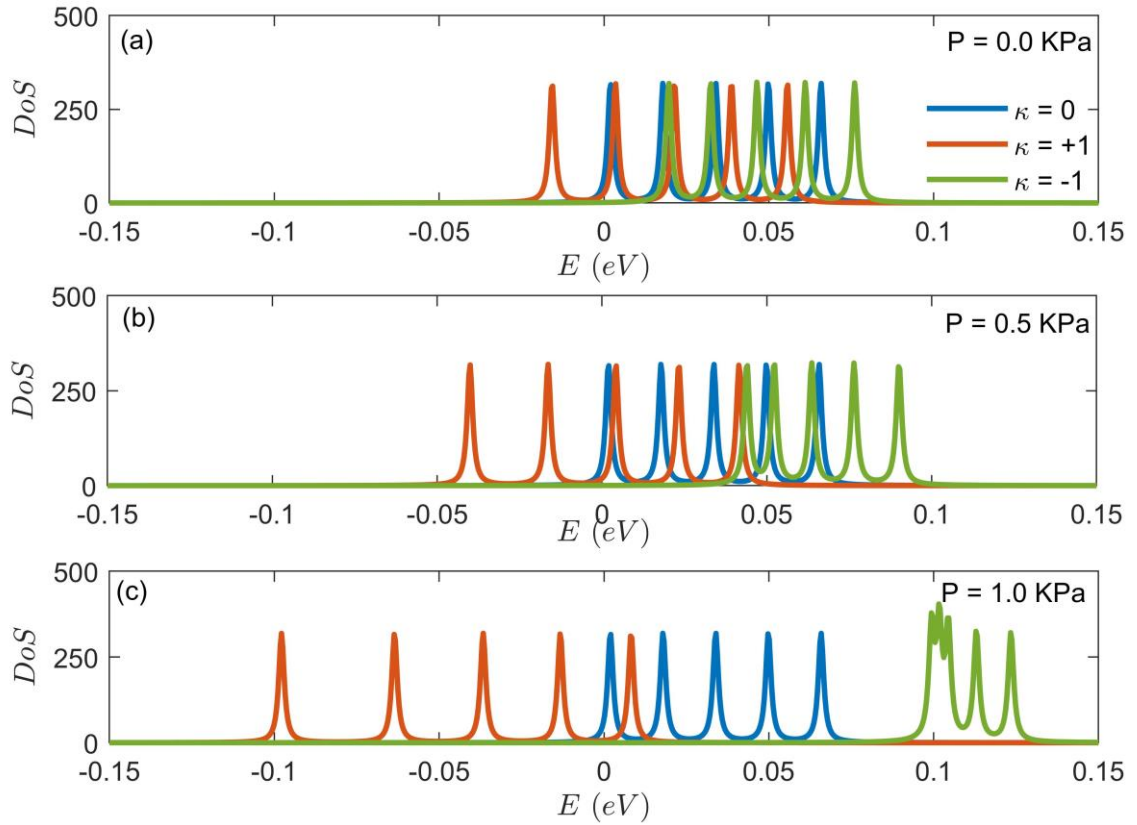


Figure 4.62: The density of state of the QD/QR system with and without impurity effect as a function of energy for n ($1 \rightarrow 5$) and three different values of pressure: (a) 0.0 KPa, (b) 0.5 KPa, and (c) 1.0 KPa.

Without pressure, the density of the state is presented in Figure 4.62 (a) in the presence and absence of impurities, while under increasing pressure at Figure 4.62 (b), a clear change appeared in the levels, the DoS is shifting to left for donor impurity and is shifting toward higher energy for acceptor impurity, this means that the material is converted to p or n -type. In Figure 4.62 (c), the bandwidth and intensity of DoS profile is affected by rising the pressure to 1.0 KPa in addition to their position shift.

The clear shifting of donor states toward negative energies is consequently matches with results of donor binding energy (negative energy) by increasing the pressure.

Additionally, the donor states are extended to wider energy range by increasing hydrostatic pressure, leading to an increase in band gap, this shifts the conduction band minimum to higher energy, the impurity levels are measured relative to conduction band appear at lower energy.

Moreover, the distinct energy states are merged in the presence of acceptor impurity. The effect of pressure on the merging of acceptor states influences the electronic properties of a material.

Increasing pressure can change the interatomic distances (change the lattice parameters) and thus modify the electronic band structure. Under high pressure, the increased overlap of atomic orbitals can cause the energy bands to broaden. This can result in the merging of previously distinct energy states, particularly around impurity levels.

Impurities introduce localized states within the band structure, which can trap charge carriers and modify the band structure. Whether the impurity is a donor or acceptor, its concentration, and its energy level relative to the conduction or valence band determines how these localized states interact with the host material's electronic structure. The interaction between impurity states and the host material's electronic states can be enhanced or diminished depending on how pressure affects the electronic band structure and impurity energy levels. For example, in a semiconductor with acceptor impurities, increasing pressure might cause the acceptor levels to shift closer to the valence band, resulting in the merging of these states and affecting hole concentration.

Overall, the combined effects of impurity type and pressure on the merging of states in the DoS are crucial for tuning the electronic properties of materials for various applications, such as in pressure sensors, transistors, and other semiconductor devices. Understanding these effects allows for precise control over material properties, enabling the design of materials with specific desired electronic characteristics.

The three dimensional plot of the previous density of state case is plotted in Figure 4.63.

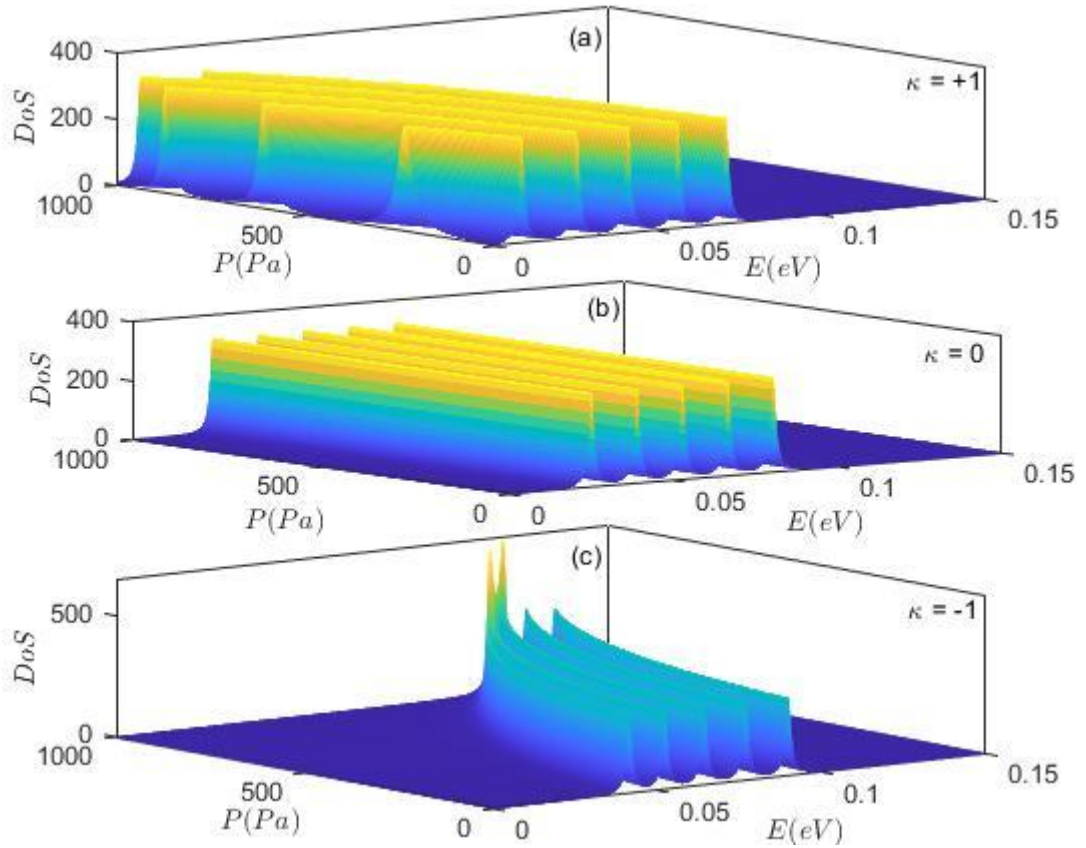


Figure 4.63: The 3D plot of the density of state, energy and pressure of the QD/QR system with and without impurity effect for n (1→5).

Now the range of n was changed (1-10) and the density of the state was studied at the same three pressure values. It was found that with increasing n , the oscillations increase and become closer together without pressure (Figure 4.64). Increasing the quantum number n provides a higher occupation of available states, altering the overall electronic structure.

As for the effect of impurities, the presence of donor impurities has shifted the DoS slightly towards the lower energy values compared to the case of absence of impurities, and it was shifted to the right in the case of the presence of acceptor impurities.

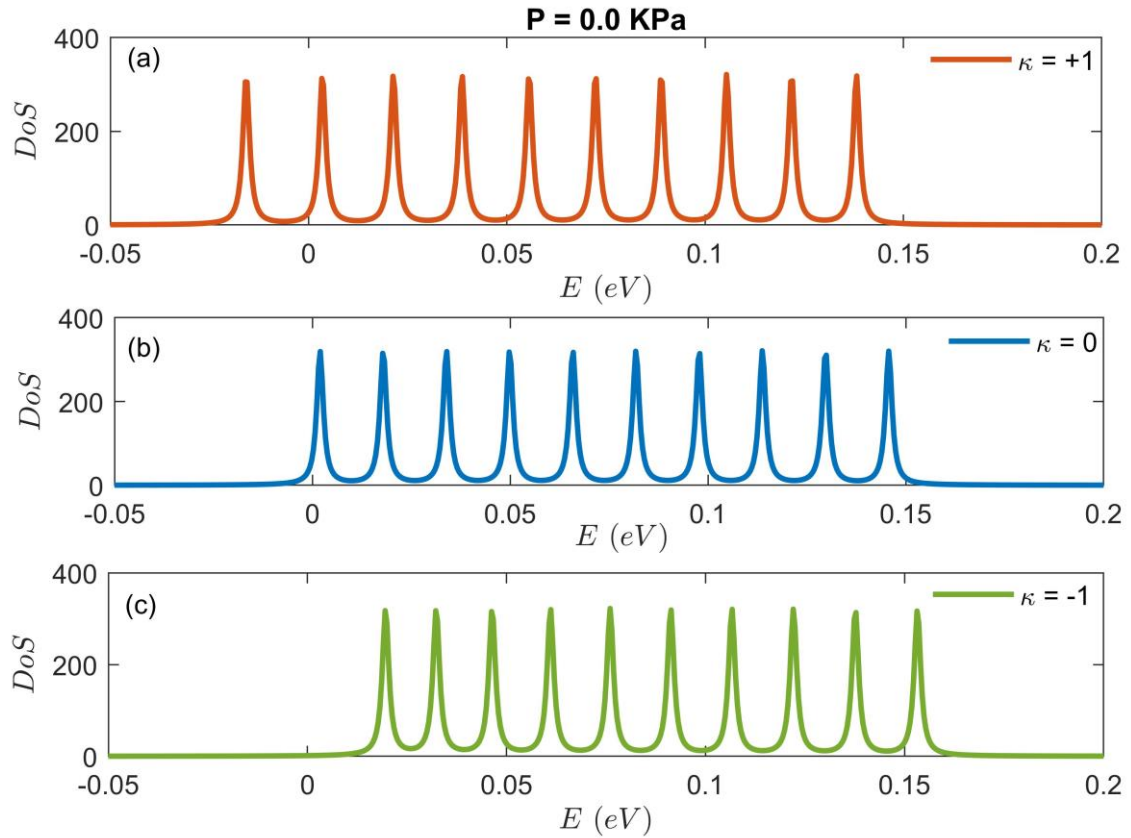


Figure 4.64: The density of state of the QD/QR system as a function of energy for n ($1 \rightarrow 10$) and specific pressure values (0.0 KPa) for (a) $\kappa = 0$, (b) $\kappa = +1$ and (c) $\kappa = -1$.

When the pressure raised to a value of 0.5 KPa as shown in Figure 4.65, the displacements of DoS profile, whether in the presence of donor impurities or acceptor impurities, become larger, and it seems that there is an event that begins to appear in a not very clear image in the case of acceptor impurities.

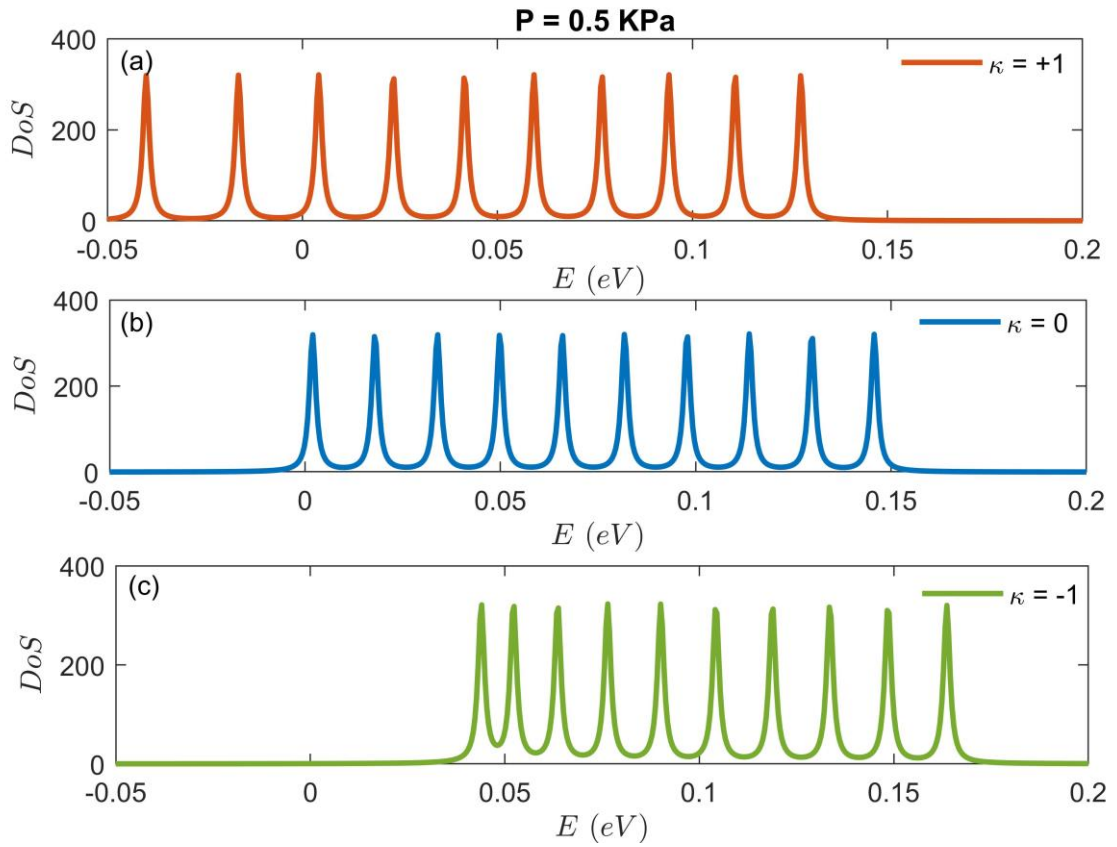


Figure 4.65: The density of state of the QD/QR system as a function of energy for n ($1 \rightarrow 10$) and specific pressure values (0.5 KPa) for (a) $\kappa = 0$, (b) $\kappa = +1$ and (c) $\kappa = -1$.

Moving to Figure 4.66, which represents a double increase in pressure (1.0 KPa). The states are shifted more to right and left, in addition to the occurrence of merging in the case of acceptor impurities, which we predicted would appear in the previous drawing.

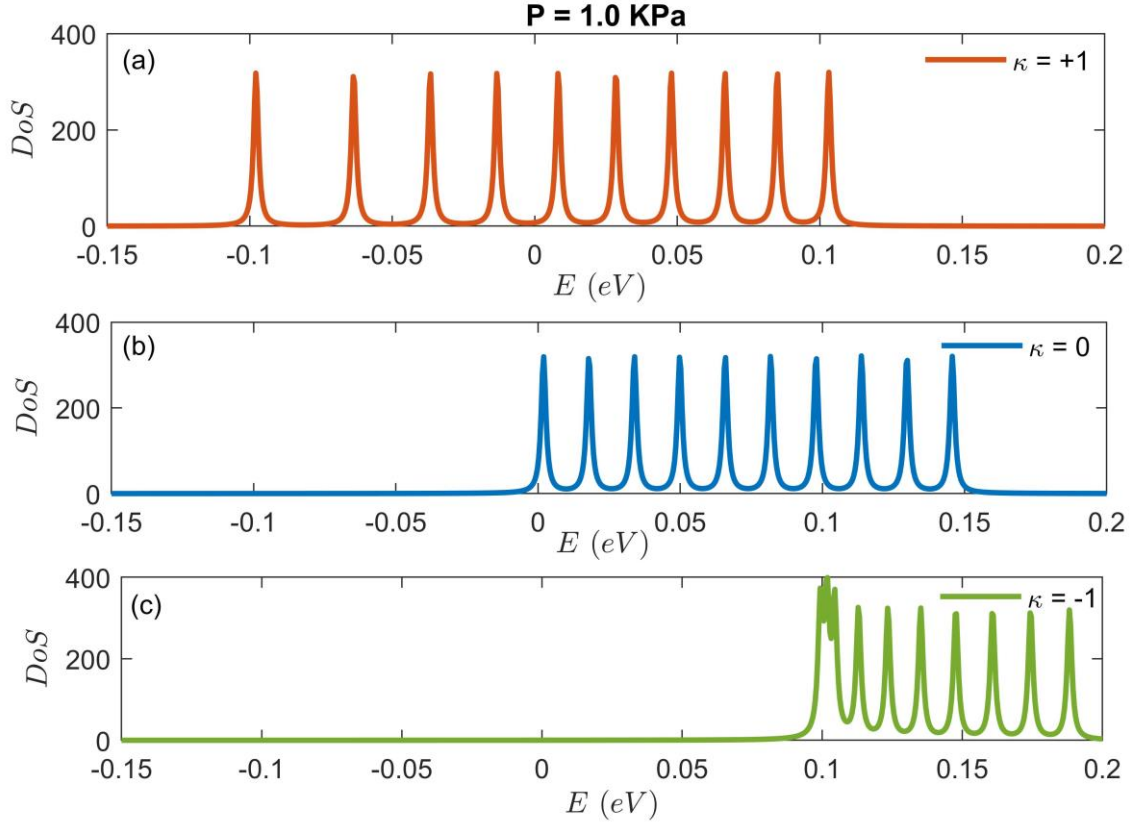


Figure 4.66: The density of state of the QD/QR system as a function of energy for n ($1 \rightarrow 10$) and specific pressure values (1.0 KPa) for (a) $\kappa = 0$, (b) $\kappa = +1$ and (c) $\kappa = -1$.

In confirmation of the effect of the values of n on the density of the state, the density of the state was studied when $n = 1-20$, and a clear increase in the number of levels was shown in a larger range of energy. Higher quantum number n leads to a higher occupation of available states, which in turn modifies the electronic structure and distribution. This increased occupation can lead to enhanced conductivity and changes in the material's electronic properties.

As for the impurities, their presence has become certain, as it causes a shift in the density of the levels in the donor and acceptor states, and by increasing the pressure from 0 to 1, the shift increases.

Figure 4.67-69, under increased pressure, a notable shift in the DoS is observed, which can be attributed to the compression of electronic states. This compression results in higher energy states becoming more populated, leading to a denser packing of the energy levels [78].

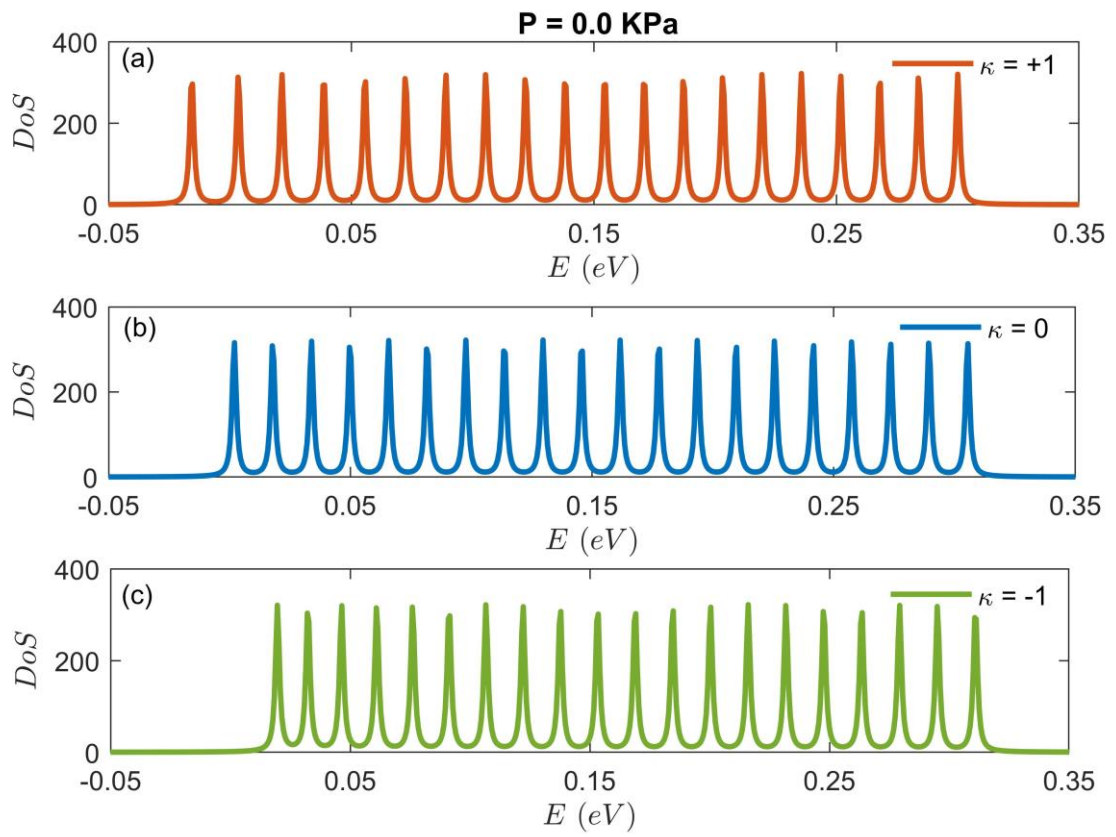


Figure 4.67: The density of state of the QD/QR system for n ($1 \rightarrow 20$) and specific pressure values (0.0 KPa) for (a) $\kappa = 0$, (b) $\kappa = +1$ and (c) $\kappa = -1$.

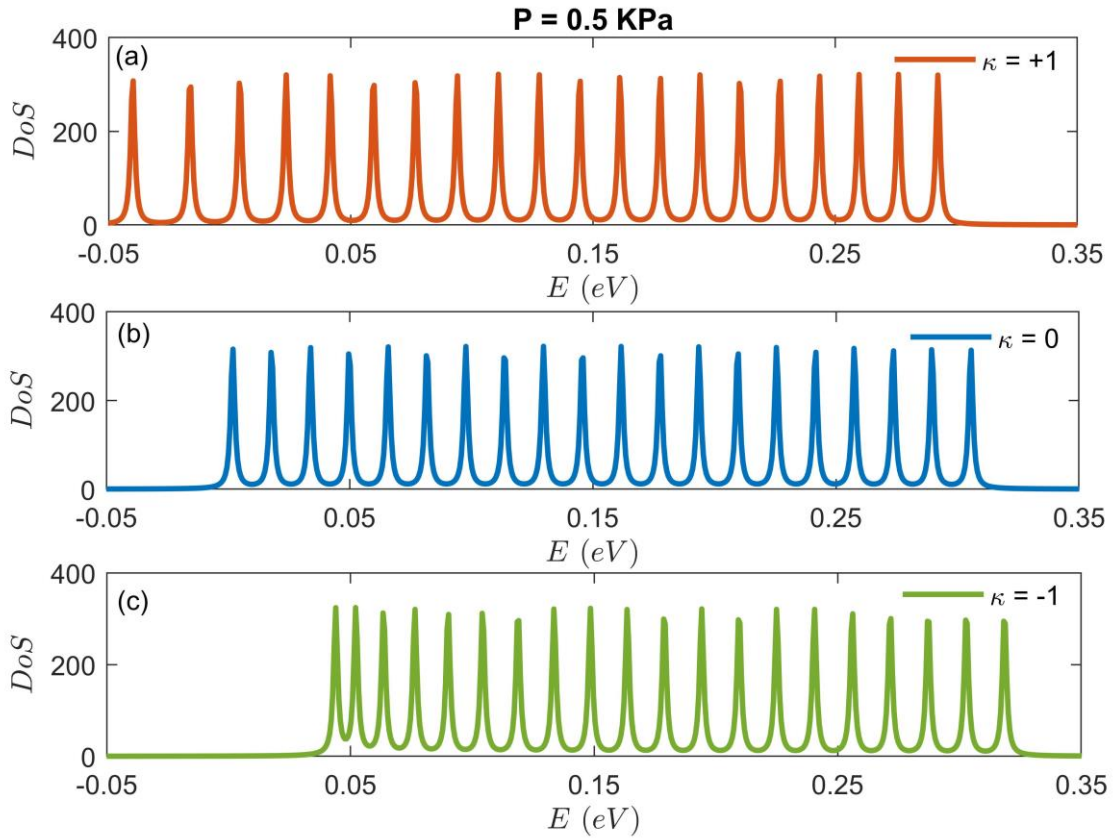


Figure 4.61: The density of state of the QD/QR system for n ($1 \rightarrow 20$) and specific pressure values (0.5 KPa) for (a) $\kappa = 0$, (b) $\kappa = +1$ and (c) $\kappa = -1$.

The type of impurity (donor for n-type and acceptor for p-type materials) significantly affects the DoS by introducing localized states within the band gap. Adding acceptor impurities creates states near the valence band. Pressure can cause these states to merge with the valence band, increasing hole concentration and improving conductivity [79].

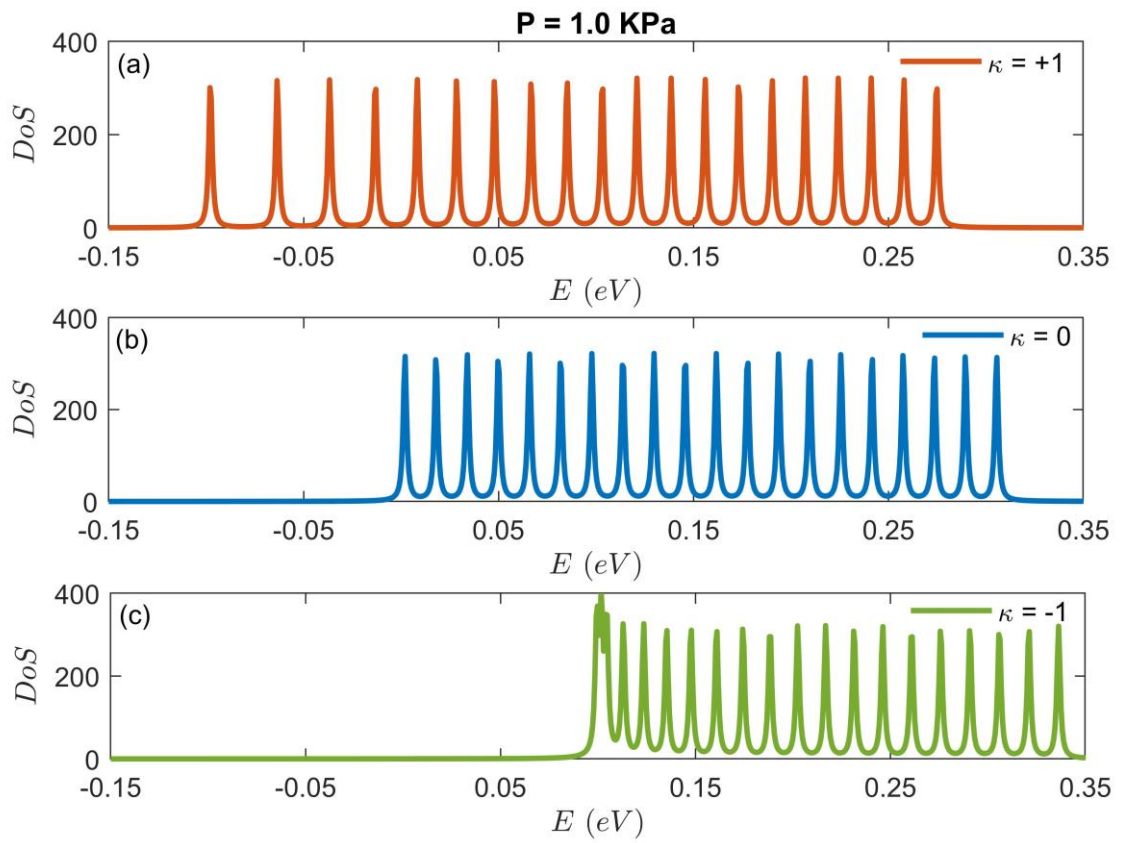


Figure 4.69: The density of state of the QD/QR system for n ($1 \rightarrow 20$) and specific pressure values (1.0 KPa) for (a) $\kappa = 0$, (b) $\kappa = +1$ and (c) $\kappa = -1$.

Chapter Four: Discussion

In this work, the electronic , thermodynamic and magnetic properties of GaAs quantum dot/ quantum ring confined by Gaussian potential and parabolic-inverse square potential in perpendicular magnetic field are discussed. The effect of temperature, magnetic field, confinement potential, pressure and impurity on these properties is presented. It is shown that the specific heat formed a peak and shifted to the right by increasing the magnetic field.

Moreover, the magneto-caloric effect is theoretically discussed in this research. The temperature dependence of the magnetic entropy changes show a pronounced maximum. The theoretical studies of the magneto-caloric effect are important, not only for technological applications, but also to understand the physical mechanisms behind the thermodynamic and magnetic properties of the materials. The process of MCE are interesting because it can eliminate the necessity for large values of the magnetic field and contribute to enhancing the performance of magnetic refrigerators.

Regarding the magnetic properties, it is observed that there are both positive (paramagnetic) and negative (diamagnetic) values for the magnetic susceptibility with and without impurity for the GaAs QD/QR.

In the near future, the calculations related to study these characteristics with other different parameters like confinement parameters and pressure are taken into consideration, we can say that the thermodynamic and magnetic properties are strongly dependent on these parameters and we hope the results will be promise in wide area in quantum physics and nanotechnology.

References

- Smith, H. I., Hawryluk, A. M., Melngailis, J. J., Schatterbug, M. L., Ceglio Jr, N. M., Price, R. H., ... & Kastner, M. A. (1982). *Submicron Structures Fabrication and Research*. Research Laboratory of Electronics (RLE) at the Massachusetts Institute of Technology (MIT).
- Ashoori, R. C. (1996). Electrons in artificial atoms. *Nature*, 379(6564), 413-419.
- Kouwenhoven, L. P., Johnson, A. T., Van der Vaart, N. C., Harmans, C. J. P. M., & Foxon, C. T. (1991). Quantized current in a quantum-dot turnstile using oscillating tunnel barriers. *Physical Review Letters*, 67(12), 1626.
- Averin, D. V., & Likharev, K. K. (1992). Possible applications of the single charge tunneling. In *Single charge tunneling: Coulomb blockade phenomena in nanostructures* (pp. 311-332). Boston, MA: Springer US.
- Madkour, L. H., & Madkour, L. H. (2019). Introduction to nanotechnology (NT) and nanomaterials (NMs). *Nanoelectronic materials: fundamentals and applications*, 1-47.
- Hossain, N., Mobarak, M. H., Mimona, M. A., Islam, M. A., Hossain, A., Zohura, F. T., & Chowdhury, M. A. (2023). Advances and significances of nanoparticles in semiconductor applications—A review. *Results in Engineering*, 19, 101347.
- Sattler, K. D. (2010). *Handbook of nanophysics: principles and methods*. CRC press.
- Monthieux, M., Serp, P., Flahaut, E., Laurent, C., Peigney, A., Razafinimanana, M., ... & Bhushan, B. (2004). *Handbook of Nanotechnology*.
- Dey, S., Swargiary, D., Dasgupta, D., Bordoloi, D., Saikia, R., Neog, D., ... & Choudhury, S. (2012). The confinement energy of quantum dots. *arXiv preprint arXiv:1212.2318*.
- Bambo, M., May, B., & Shumbula, P. (2022). Fabrication Methods of Quantum Dots—Polymer Composites. In *Quantum Dots and Polymer Nanocomposites* (pp. 125-150). CRC Press.
- Hunagund, S. (2023). Quantum Engineering: Quantum dots. In *Principles and Applications of Quantum Computing Using Essential Math* (pp. 77-106). IGI Global.
- Ramalingam, G., Kathirgamanathan, P., Ravi, G., Elangovan, T., Manivannan, N., & Kasinathan, K. (2020). Quantum confinement effect of 2D nanomaterials. In *Quantum dots-fundamental and applications*. IntechOpen.
- Parak, W. J., Manna, L., & Nann, T. (2010). Fundamental principles of quantum dots. *Nanotechnology: Online*, 73-96.

Paras, Yadav, K., Kumar, P., Teja, D. R., Chakraborty, S., Chakraborty, M., ... & Hang, D. R. (2022). A review on low-dimensional nanomaterials: nanofabrication, characterization and applications. *Nanomaterials*, 13(1), 160.

Moody, G. (2013). *Confinement Effects on the Electronic and Optical Properties of Semiconductor Quantum Dots Revealed with Two-Dimensional Coherent Spectroscopy* (Doctoral dissertation, University of Colorado at Boulder).

Chakraborty, T. (1999). Quantum Dots: A survey of the properties of artificial atoms.

Rourk, C., Huang, Y., Chen, M., & Shen, C. (2021). Indication of strongly correlated electron transport and Mott insulator in disordered multilayer ferritin structures (DMFS). *Materials*, 14(16), 4527.

F. M. Bzour. (2016). Effects of the hydrostatic pressure and temperature on the properties of the (GaAs) single quantum dot in a magnetic field, M. Sc Thesis, An-Najah National University.

Torimoto, T., Kameyama, T., Uematsu, T., & Kuwabata, S. (2023). Controlling optical properties and electronic energy structure of I–III–VI semiconductor quantum dots for improving their photofunctions. *Journal of Photochemistry and Photobiology C: Photochemistry Reviews*, 54, 100569.

Petryayeva, E., Algar, W. R., & Medintz, I. L. (2013). Quantum dots in bioanalysis: a review of applications across various platforms for fluorescence spectroscopy and imaging. *Applied spectroscopy*, 67(3), 215-252.

Koole, R., Groeneveld, E., Vanmaekelbergh, D., Meijerink, A., & de Mello Donegá, C. (2014). Size effects on semiconductor nanoparticles. *Nanoparticles: Workhorses of Nanoscience*, 13-51.

Martins, C. S., LaGrow, A. P., & Prior, J. A. (2022). Quantum dots for cancer-related miRNA monitoring. *Acs Sensors*, 7(5), 1269-1299.

Mamiyev, Z., & Balayeva, N. O. (2023). PbS nanostructures: A review of recent advances. *Materials Today Sustainability*, 21, 100305.

Çakır, B., Yakar, Y., & Özmen, A. (2012). Refractive index changes and absorption coefficients in a spherical quantum dot with parabolic potential. *Journal of Luminescence*, 132(10), 2659-2664.

Masumoto, Y., & Takagahara, T. (Eds.). (2013). *Semiconductor quantum dots: physics, spectroscopy and applications*. Springer Science & Business Media.

Arakawa, Y., & Holmes, M. J. (2020). Progress in quantum-dot single photon sources for quantum information technologies: A broad spectrum overview. *Applied Physics Reviews*, 7(2).

Pal, S., Ghosh, M., & Duque, C. A. (2019). Impurity related optical properties in tuned quantum dot/ring systems. *Philosophical Magazine*.

Vladimir, M. Fomin. *Physics of Quantum Rings*. Springer.

Kim, H. D., Kyhm, K., Taylor, R. A., Nogues, G., Je, K. C., Lee, E. H., & Song, J. D. (2013). Asymmetry of localised states in a single quantum ring: Polarization dependence of excitons and biexcitons. *Applied Physics Letters*, *102*(3).

Lin, T. C., Lin, C. H., Ling, H. S., Fu, Y. J., Chang, W. H., Lin, S. D., & Lee, C. P. (2009). Impacts of structural asymmetry on the magnetic response of excitons and biexcitons in single self-assembled In (Ga) As quantum rings. *Physical Review B—Condensed Matter and Materials Physics*, *80*(8), 081304.

Mukherjee, T. (2011). *Thermodynamics of magnetic multilayers*. The University of Nebraska-Lincoln.

Tishin, A. M. (2008). Magnetic therapy of malignant neoplasms by injecting material particles with high magnetocaloric effect and suitable magnetic phase transition temperature. *Patent number: EP1897590-A1*.

De Oliveira, N. A., & von RANKE, P. J. (2010). Theoretical aspects of the magnetocaloric effect. *Physics Reports*, *489*(4-5), 89-159.

Kirak, M. U. H. A. R. R. E. M. (2021). Magnetic and thermodynamic properties of GaAs quantum dot confined by parabolic-inverse square plus gaussian potential. *Journal of Magnetism and Magnetic Materials*, *536*, 167481.

Manaselyan, A. K., Barseghyan, M. G., Kirakosyan, A. A., Laroze, D., & Duque, C. A. (2014). Effects of applied lateral electric field and hydrostatic pressure on the intraband optical transitions in a GaAs/Ga_{1-x}Al_xAs quantum ring. *Physica E: Low-dimensional Systems and Nanostructures*, *60*, 95-99.

Radu, A., Kirakosyan, A. A., Laroze, D., & Barseghyan, M. G. (2015). The effects of the intense laser and homogeneous electric fields on the electronic and intraband optical properties of a GaAs/Ga_{0.7}Al_{0.3}As quantum ring. *Semiconductor Science and Technology*, *30*(4), 045006.

Bejan, D. (2017). Donor impurity-related nonlinear optical rectification in a two-dimensional quantum ring under magnetic field. *Physics Letters A*, *381*(38), 3307-3313.

Niculescu, E. C., & Bejan, D. (2017). Off-centre impurity-related nonlinear optical absorption, second and third harmonic generation in a two-dimensional quantum ring under magnetic field. *Philosophical Magazine*, *97*(24), 2089-2107.

Duque, C. M., Morales, A. L., Mora-Ramos, M. E., & Duque, C. A. (2013). Optical nonlinearities associated to applied electric fields in parabolic two-dimensional quantum rings. *Journal of luminescence*, *143*, 81-88.

Zhang, Z., Liu, L., Huang, H., Li, L., Wang, Y., Xu, J., & Xu, J. (2020). Encapsulation of CsPbBr₃ perovskite quantum dots into PPy conducting polymer: Exceptional water stability and enhanced charge transport property. *Applied Surface Science*, *526*, 146735.

- Wang, L. L., Chen, N., Bin, S., Mo, Y. H., Ma, L. L., He, G. L., ... & Yuan, J. H. (2018). Effect of conduction band parabolicity on the spectrum and binding energy of a hydrogenic impurity in GaAs spherical quantum dots. *Philosophical Magazine*, 98(10), 899-910.
- Hayrapetyan, D. B., Amirkhanyan, S. M., Kazaryan, E. M., & Sarkisyan, H. A. (2016). Effect of hydrostatic pressure on diamagnetic susceptibility of hydrogenic donor impurity in core/shell/shell spherical quantum dot with Kratzer confining potential. *Physica E: Low-dimensional Systems and Nanostructures*, 84, 367-371.
- Hayrapetyan, D. B., Kazaryan, E. M., & Tevosyan, H. K. (2014). Impurity states in a cylindrical quantum dot with the modified Pöschl-Teller potential. *Journal of Contemporary Physics (Armenian Academy of Sciences)*, 49, 119-122.
- Peter, A. J. (2005). The effect of hydrostatic pressure on binding energy of impurity states in spherical quantum dots. *Physica E: Low-dimensional Systems and Nanostructures*, 28(3), 225-229.
- Movilla, J. L., & Planelles, J. (2005). Image charges in spherical quantum dots with an off-centered impurity: algorithm and numerical results. *Computer physics communications*, 170(2), 144-152.
- Zhu, J. L., Xiong, J. J., & Gu, B. L. (1990). Confined electron and hydrogenic donor states in a spherical quantum dot of GaAs-Ga_{1-x}Al_xAs. *Physical Review B*, 41(9), 6001.
- Porrás-Montenegro, N., & Pe, S. T. (1992). Hydrogenic impurities in GaAs-(Ga, Al) as quantum dots. *Physical Review B*, 46(15), 9780.
- Pérez-Merchancano, S. T., Bolívar-Marinez, L. E., & Silva-Valencia, J. (2007). The binding energy of donor impurities in GaAs quantum dots under the pressure effect. *Revista mexicana de física*, 53(6), 470-474.
- Bose, C., & Sarkar, C. K. (2000). Binding Energy of Impurity States in Spherical GaAs-Ga_{1-x}Al_xAs Quantum Dots. *physica status solidi (b)*, 218(2), 461-469.
- Bayrak, O. R. H. A. N., Boztosun, I., & Ciftci, H. A. K. A. N. (2007). Exact analytical solutions to the Kratzer potential by the asymptotic iteration method. *International Journal of Quantum Chemistry*, 107(3), 540-544.
- Rezaei, G., Taghizadeh, S. F., & Enshaeian, A. A. (2012). External electric field, hydrostatic pressure and temperature effects on the binding energy of an off-center hydrogenic impurity confined in a spherical Gaussian quantum dot. *Physica E: Low-dimensional Systems and Nanostructures*, 44(7-8), 1562-1566.
- Yakar, Y., Çakır, B., & Özmen, A. (2018). Magnetic field effects on oscillator strength, dipole polarizability and refractive index changes in spherical quantum dot. *Chemical Physics Letters*, 708, 138-145.

- Jahromi, A. S., & Rezaei, G. (2015). Electromagnetically induced transparency in a two-dimensional quantum pseudo-dot system: Effects of geometrical size and external magnetic field. *Physica B: Condensed Matter*, 456, 103-107.
- Ikhdaïr, S. M., & Hamzavi, M. (2012). A quantum pseudodot system with two-dimensional pseudoharmonic oscillator in external magnetic and Aharonov-Bohm fields. *Physica B: Condensed Matter*, 407(21), 4198-4207.
- Elsaid, M., Hjaz, E., & Shaer, A. (2017). Energy states and exchange energy of coupled double quantum dot in a magnetic field. *International Journal of Nano Dimension*, 8(1), 1-8.
- Shaer, A., Elsaid, M. K., & Elhasan, M. (2016). Magnetization of GaAs parabolic quantum dot by variation method. *J. Phys. Sci. Appl*, 6(2), 39-46.
- Khordad, R. (2013). Use of modified Gaussian potential to study an exciton in a spherical quantum dot. *Superlattices and Microstructures*, 54, 7-15.
- Mikhail, I. F. I., & Shafee, A. M. (2017). Optical absorption in a disk-shaped quantum dot in the presence of an impurity. *Physica B: Condensed Matter*, 507, 142-146.
- Bejan, D., Stan, C., & Niculescu, E. C. (2018). Optical properties of an elliptic quantum ring: Eccentricity and electric field effects. *Optical Materials*, 78, 207-219.
- Gharaati, A., & Khordad, R. (2010). A new confinement potential in spherical quantum dots: modified Gaussian potential. *Superlattices and Microstructures*, 48(3), 276-287.
- Yakar, Y., Çakır, B., & Özmen, A. (2010). Calculation of linear and nonlinear optical absorption coefficients of a spherical quantum dot with parabolic potential. *Optics Communications*, 283(9), 1795-1800.
- Rezaei, G., Vaseghi, B., & Sadri, M. (2011). External electric field effect on the optical rectification coefficient of an exciton in a spherical parabolic quantum dot. *Physica B: Condensed Matter*, 406(24), 4596-4599.
- Xie, W. (2010). Optical properties of an off-center hydrogenic impurity in a spherical quantum dot with Gaussian potential. *Superlattices and Microstructures*, 48(2), 239-247.
- Kerdi, B., Pierre, M., Cours, R., Warot-Fonrose, B., Goiran, M., & Escoffier, W. (2020). High magnetic field spin-valley-split Shubnikov-de Haas oscillations in a W Se 2 monolayer. *Physical Review B*, 102(15), 155106.
- Beale, P. D. (1996). *Statistical Mechanics*. Butterworth-Heinemann.
- Ghanbari, A., Khordad, R., Taghizadeh, F., Nasirizadeh, I., Edet, C. O., & Ali, N. (2022). Impurity effect on thermal properties of tuned quantum dot/ring systems. *Chemical Physics Letters*, 806, 140000.

Arora, S., Gupta, Y., Khosla, P., Priyanka, & Sharma, R. (2023). Impact of Impurity on the Mean Energy, Heat Capacity, Free Energy, Entropy and Magnetocaloric Effect of Ga $1-\chi$ Al χ As Quantum Wire. *Journal of Low Temperature Physics*, 212(1), 54-68.

Alia, A. A., Elsaied, M. K., & Shaer, A. (2019). Magnetic properties of GaAs parabolic quantum dot in the presence of donor impurity under the influence of external tilted electric and magnetic fields. *Journal of Taibah University for Science*, 13(1), 687-695.

Sivakami, A., & Gayathri, V. (2013). Hydrostatic pressure and temperature dependence of dielectric mismatch effect on the impurity binding energy in a spherical quantum dot. *Superlattices and Microstructures*, 58, 218-227.

Peter, A. J. (2009). The effect of position dependent effective mass of hydrogenic impurities in parabolic GaAs/GaAlAs quantum dots in a strong magnetic field. *International Journal of Modern Physics B*, 23(26), 5109-5118.

Servatkah, M., Hashemi, P., & Pourmand, R. (2022). Binding energy in tuned quantum dots under an external magnetic field. *Journal of Optoelectronic Nanostructures*, 7(4), 49-65.

Luo, J. W., Franceschetti, A., & Zunger, A. (2008). Quantum-size-induced electronic transitions in quantum dots: Indirect band-gap GaAs. *Physical Review B—Condensed Matter and Materials Physics*, 78(3), 035306.

Ghaltaghchyan, H. T., Kazaryan, E. M., & Sarkisyan, H. A. (2016). Diamagnetism in the cylindrical quantum dot with parabolic confinement potential. *Ученые записки Ереванского государственного университета, серия Физические и Математические науки*, (3), 20-24.

Haddad, H., Nammas, F. S., Al Shorman, M. M., & Shukri, A. A. (2017). Electronic structure of one electron confined in three-dimensional quantum dots. *Physica B: Condensed Matter*, 526, 132-135.

Vicente, A. G. J., Castro, L. B., Obispo, A. E., & Meza, L. E. A. (2021). Remarks on thermodynamic properties of a double ring-shaped quantum dot at low and high temperatures. *Journal of Low Temperature Physics*, 202(3), 372-381.

Kuyanov, P., McNamee, S. A., & LaPierre, R. R. (2018). GaAs quantum dots in a GaP nanowire photodetector. *Nanotechnology*, 29(12), 124003.

Fakkahi, A., Sali, A., Jaouane, M., & Arraoui, R. (2021). Hydrostatic pressure, temperature, and electric field effects on the hydrogenic impurity binding energy in a multilayered spherical quantum dot. *Applied Physics A*, 127, 1-9.

Bai, F., Bian, K., Huang, X., Wang, Z., & Fan, H. (2019). Pressure induced nanoparticle phase behavior, property, and applications. *Chemical reviews*, 119(12), 7673-7717.

Lau, W. H. (2000). *Quantum Theory of the Electronic and Optical Properties of Low-dimensional Semiconductor Systems*. National Library of Canada= Bibliothèque nationale du Canada, Ottawa.

تأثيرات الشوائب على الخواص الالكترونية والحرارية و المغناطيسية للنقاط/الحلقات الكمية في الهياكل الدقيقة لمادة زرنيخيد الغاليوم

ألفت عبد الفتاح إبراهيم عمرية

د. مؤيد أبو صاع

د. عدلي صالح

أ.د. محمد السعيد

أ.د. عاطف قسراوي

أ.د. حسين شنك

د. إياد سعد الدين

ملخص

في هذه الرسالة، يتم دراسة أطياف الطاقة لنقطة/حلقة كمومية من زرنيخيد الغاليوم مضبوطة مع جهد مكافئ معكوس مربع واحتجاز غاوسي معدل تحت تأثير حقل مغناطيسي خارجي. لتحقيق هذا الهدف، يتم حل معادلة شرودنجر تحليليًا بدون ومع النظر في الشوائب المانحة والمتقبلة ويتم اشتقاق القيم الذاتية للطاقة تحليليًا ضمن إطار الكتلة الفعالة والتقريب النطاقي المكافئ. كما تم التحقيق نظريًا في طاقة الربط للحالة الأرضية والحالة المثارة الأولى للنظام مع الأخذ في الاعتبار مختلف المعايير. تظهر النتائج أن الأطياف الطاقية وطاقة الربط تتأثر بوضوح بمعايير مختلفة. علاوة على ذلك، تم دراسة كثافة المستويات في نظام النقطة/الحلقة الكمومية الذي يتميز بتغيرات في الحقول المغناطيسية، والضغط، والشوائب. توفر كثافة المستويات رؤى مذهلة حول الخصائص الإلكترونية للمواد واستجابتها للمعايير الخارجية.

بناءً على الأطياف الطاقية المحسوبة، تم الحصول نظرياً على الدوال الحرارية للنظام. تم حساب دالة التقسيم مع الطيف الطاقى الصحيح، ثم تم حساب الطاقة المتوسطة، والطاقة الحرة، والحرارة النوعية، وعدم الانتظام لنظام النقطة/الحلقة الكمومية المضبوطة مع وبدون تأثير الشوائب كدالة لدرجة الحرارة والحقل المغناطيسي. يتبين أن وجود تأثير الشوائب يسبب بنية قمة في الحرارة النوعية للنظام. كما تم التحقيق في تغير الفوضى المغناطيسية للنظام كدالة لدرجة الحرارة والحقل المغناطيسي. لوحظ أن اعتماد درجة الحرارة لتأثير المغناطيس الحراري يظهر حد أقصى ملحوظ في درجات حرارة محددة.

بالإضافة إلى ذلك، تُظهر النتائج أن درجة الحرارة، والمجال المغناطيسي، والشوائب لها تأثير كبير على الخصائص المغناطيسية للهيك، وتم التحقيق في سلوك المغنطة، والحساسية المغناطيسية للنظام على مدى واسع. توفر هذه النتائج أساساً حاسماً للأبحاث التجريبية المستقبلية والتطبيقات العملية في علوم المواد وفيزياء المادة المكثفة.

كلمات مفتاحية: النقطة الكمومية، الحلقة الكمومية، الخصائص المغناطيسية، الخصائص الحرارية، الشوائب.